Impact of Mooring Systems on Wave Energy Converter Control and Useful Power Capture

by

Spencer Funk
B.Eng., University of Victoria, 2021

A Thesis Submitted in Partial Fulfillment of the
Requirements for the Degree of

MASTER OF APPLIED SCIENCE

in the Department of Mechanical Engineering

We acknowledge and respect the Lək̓ʷəŋən (Songhees and Esquimalt) Peoples on whose territory the university stands, and the Lək̓ʷəŋən and W̱SÁNEĆ Peoples whose historical relationships with the land continue to this day.

Impact of Mooring Systems on Wave Energy Converter Control and Useful Power Capture

by

Spencer Funk

B.Eng., University of Victoria, 2021

Supervisory Committee

Dr. Brad Buckham, Supervisor
Department of Mechanical Engineering

Dr. Flavio Firmani, Departmental Member
Department of Mechanical Engineering

Abstract

With the effects of climate change becoming more extreme each year there is a dire need to reduce carbon emissions – especially in the energy sector. An energy source currently not in use by any sector is the energy stored in ocean waves. Wave energy can be captured by wave energy converters (WECs) which transform said energy into electricity using a power take-off device. However, these devices are currently too expensive to build and operate for the power they produce.

The common approach to designing a WEC is to optimize its design with modelling and testing and then deploy it in the ocean with a mooring system. Notably, the mooring system is typically neglected at the modelling and testing stages. But the significance of the mooring dynamics to the system response is not fully understood. This work demonstrates that neglecting the mooring system can lead to up to a 50% power loss by modelling the power production of a controlled self-reacting point absorber (SRPA) with and without knowledge of the mooring system.

To address these outstanding questions, four mooring designs were characterized using a unique approach and incorporated into a mechanical circuit model of the SRPA. The characterization approach was used to fit high-fidelity mooring simulation data to linear transfer function models with a high degree of accuracy. Such models significantly reduce simulation time of the SRPA by reducing the mooring dynamics to just the force at its connection to the SRPA.

This new model was then used to determine impacts on dynamics and power production. The circuit model was also used to demonstrate the effect of the mooring on three control types.

The effects amounted to up to a 40% reduction of the control variable, suggesting that current controllers may be overdesigned and more expensive as a result.

Finally, the annual energy production of three control types were compared by modelling and simulating a moored SRPA in a realistic sea. The simulation results indicated that the performance gains previously seen for a new control type are not eroded by the mooring system or by the realistic sea, with the new control type resulting in four times more annual energy production than the others.

Table of Contents

List of Tables

List of Figures

List of Acronyms and Parameters

Acronym	Description
AM control	Amplitude control
C1	Case 1, no mooring
C2	Case 2, mooring in dynamics
C3	Case 3, mooring in dynamics and control
CC control	Complex-conjugate control
DOF	Degree of freedom
FFT	Fast Fourier transform
GA control	Geometry-amplitude control
GW	Gigawatt
GWh	Gigawatt-hour
kWh	Kilowatt-hour
LCOE	Levelized cost of energy
MWh	Megawatt-hour
NRMSE	Normalized root mean square error
PM	Pierson-Moskowitz
PTO	Power take-off
RAO	Response amplitude operator
SBPA	Single-body point absorber
SRPA	Self-reacting point absorber
SSB	Sea-state based control
TW	Terawatt
WEC	Wave energy converter

Parameter	Description	Units
α	Scaling parameter from full scale to model scale	-
ν	Kinematic viscosity of a fluid	m^2/s
ω	Angular frequency	rad/s
ω_d	Damped natural frequency	rad/s
ω_t	Frequency chosen to tune to	rad/s
ρ	Density of water	kg/m^3
A	Added mass	kg
a	Acceleration	m/s^2
A_b	Added mass of a mooring node	kg
A_w	Monochromatic ocean wave amplitude	m
b	Radiation damping	Ns/m
b_a	Mooring material internal damping	Ns/m
b_b	Linearized drag of mooring segment	Ns/m
b_{bs}	Damping of seabed	Ns/m
c	Damping	Ns/m
D	Denominator of transfer function	–

E_w	Energy in a monochromatic ocean wave	J
F	Force	N
f	frequency	Hz
F_A	Added mass force on WEC	N
$F_{B,mean}$	Buoyant force at mean position of WEC	N
F_{eq}	Force resultant from excitation of equivalent impedance	N
F_{ex}	Wave excitation force per unit wave amplitude	N/m
F_{FK}	Froude-Krylov force	N
F_{FS}	Force generated by reactive force source	N
F_i	Force generated by excitation of intrinsic mechanical impedance of an SRPA	N
F_k	Hydrostatic stiffness of WEC	N
F_m	Inertial force due to mass	N
F_{moor}	Force resultant from excitation of mooring	N
F_R	Radiation damping force	N

F_r	Froude number	$-$
F_s	Scattering force	N
F_{Th}	Thevenin equivalent excitation force per unit wave amplitude	N/m
g	Gravitational acceleration	m/s^2
H_{m0}	Significant wave height of wave spectrum	m
i	Imaginary unit	$-$
k	Stiffness	N/m
k_a	Mooring material stiffness	N/m
k_{bs}	Stiffness of seabed	N/m
m	Mass	kg
m_b	Mass of a mooring node	kg
m_{eff}	Effective mass	kg
N	Numerator of transfer function	$-$
P_{RAO}	Useful power RAO	W/m
P_u	Useful power	W
R	Resistive impedance	Ns/m
R_e	Reynolds number	$-$
R_{PTO}	Resistance of PTO	Ns/m
S	Variance density	m^2/Hz
s	Laplace variable	$-$

T_e	Energy period of wave spectrum	s
T_p	Peak period of wave spectrum	s
T_w	Temporal period of monochromatic ocean wave	s
u , v	Velocity	m/s
u_1	Heave velocity of float	m/s
u_2	heave velocity of spar	m/s
u_{Th}	Thevenin equivalent velocity	m/s
x	Position	m
X	Reactive impedance	Ns/m
X_{Fs}	Reactance of reactive force source	Ns/m
Z	Impedance	Ns/m
Z_a	Impedance between mooring segments	Ns/m
Z_b	Impedance between mooring node and ground	Ns/m
Z_{eq}	Equivalent impedance of combined elements	Ns/m
Z_{eq1}	Equivalent impedance of combined elements of float	Ns/m
Z_{eq2}	Equivalent impedance of combined elements of spar	Ns/m
$Z_{eq2}^{'}$	Equivalent impedance of combined elements of spar excluding mooring	Ns/m
Z_i	Intrinsic mechanical impedance of an SRPA	Ns/m
Z_k	Hydrostatic stiffness impedance	Ns/m
Z_m	Mass impedance	Ns/m
Z_{moor} , Z_1	Impedance of mooring system	Ns/m
Z_{PTO}	PTO impedance	Ns/m
Z_R	Radiation damping impedance	Ns/m

Acknowledgements

First, I would like to thank my supervisor Dr. Buckham for his continued guidance and support and for giving me the opportunity to do this work. I also want to thank Dr. Kush Bubbar and Dr. Ali Haider from the University of New Brunswick for helping me learn how to use new tools and for their excellent suggestions. I would also like to thank Dr. Firmani for fostering my passion for teaching and giving me opportunities to try new things, challenge myself, and guide others.

A massive shout out to Pauline, Heather, Nisa, Patrick, Luke, and Gerard for always being willing to talk ideas out with me; my thoughts would still be tangled around and circling back on themselves if it weren't for all of your generosity with your time and your feedback. Another huge shout out to all the buddies who helped me get out of my own head at the end of the day by hanging out and playing games together. I would have gone nuts without you guys.

Thank you, Mom, and thank you, Dad, for raising me to be inquisitive, supporting my passions, and always loving me; I love you both more than I could ever say. Thanks for being such a great brother Austin, we've been through a lot together and you've always been there for me. I admire you so much and I'm so proud to be your brother. Most of all, thank you to Sophie. You've given me endless encouragement and kept me going through all this. I am so happy to be walking along beside you. I love you more than everything

Chapter 1

Introduction to Wave Energy

With the effects of climate change becoming more extreme each year there is a dire need to reduce carbon emissions – especially in the energy sector. This need is currently being addressed largely by electrification of historically polluting industries such as transportation. The electrification process is increasing the demands of global energy systems while we also aim to transition those systems to cleaner sources of power.

A key realization made about the ongoing energy transition is that the temporal variability in solar and wind power requires grid-scale energy storage in order to smooth out the intermittencies of those technologies. Implementing such storage systems are challenging due in part to their economic infeasibility [1], and a lack of natural resources. An approach which would help to reduce the necessary size of grid-scale energy storage is introducing new renewable energy technologies. Renewables such as wind and solar have varying levels of predictability, but by diversifying the renewable mix with new energy sources with their own variability, the overall energy system becomes more consistent. A greater variety of renewable energy technologies means the variation of each becomes less prevalent and they tend to average out, resulting in a steadier supply of renewable power.

Even if the storage problem is solved there is not a single renewable energy technology that works in every region. For example, countries in the far North or South have much less solar power available during the Winter months making solar less suitable. Similarly, some regions have very

little wind. Even if a renewable resource is available at the scale required, there may not be space available to install the renewable generator. These issues point to a need for additional sources of renewable energy.

Wave energy is uniquely positioned to aid in solving each of these issues. Adding another renewable energy source helps to average out the overall power, but wave energy also exhibits some desirable traits. Waves are more consistent than wind, only varying significantly seasonally, so harnessing their energy could help provide a consistent baseload to the grid [2]. Because these variations are somewhat predictable they are easier to incorporate into the grid and support other renewables [3]. Short-term variations caused by the period of the waves are difficult to manage at first glance, but it has been shown that this issue may be resolved by installing many wave energy devices to achieve steady power during any single sea condition [4]. Additionally, wave energy adds another option for coastal communities where there may not be enough appropriate space for wind or solar farms. However, harnessing this energy is currently too expensive, requiring improvements to be made to the devices designed to capture it.

1.1 Global and Local Wave Resources

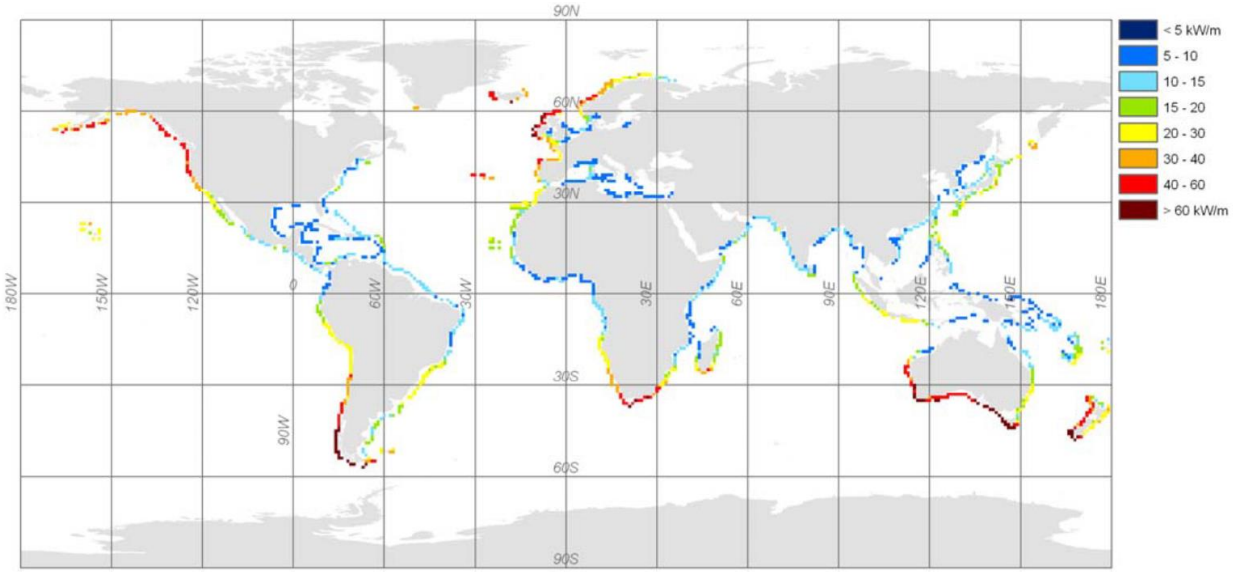

Figure 1-1 Average annual theoretical coastal power from [5].

Globally there is potential for 3 TW of available wave energy [5]. The available resource results from eliminating distant and low power resources as well as areas covered by sea ice [5]. Figure 1-1 shows that the most potential is along the West Coasts in the Northern and Southern hemispheres with energy dropping off near the equator. This puts Canada in a unique position with about half of North America's wave energy resource off the coast of British Columbia. This resource amounts to a net energy flux of about 100 GW for the region [5], which, even accounting for the efficiency of a device is comparable to British Columbia's 2019 installed power capacity of 18.25 GW [6]. Due to this potential, the resource in the region has been studied rigorously.

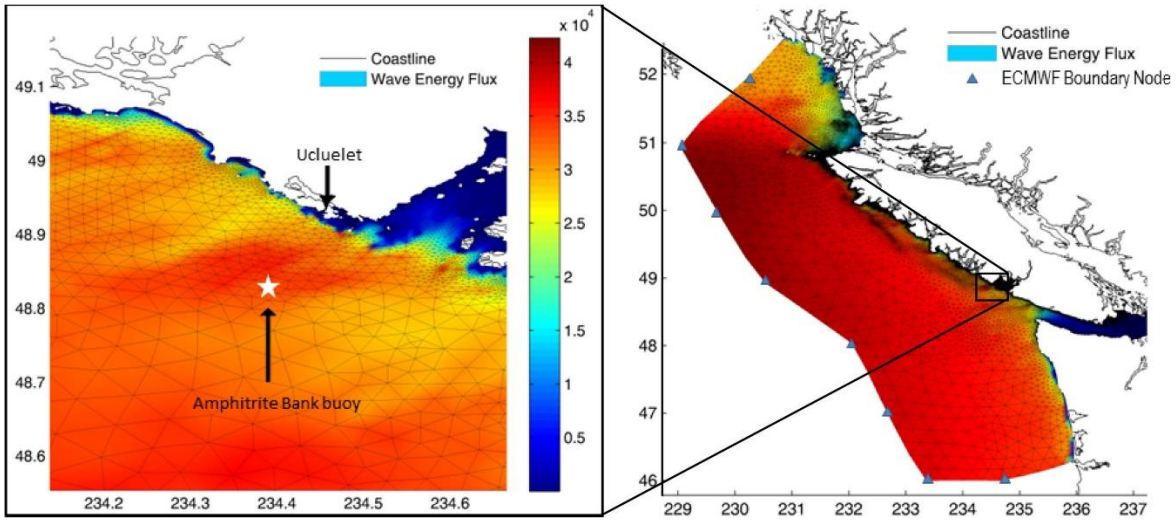

Figure 1-2Mean annual wave energy flux off Vancouver Island [W/m] from [7].

A model of the wave flux around Vancouver Island determined that the total wave energy in the region amounts to 140 GWh [7]. Further research into specific sites in this region estimated the available resource while allowing considerations for fishing, marine traffic and ecologically sensitive zones [8], and determined with those considerations that 67,000 GWh of annual energy is available in the region. Estimating that 10% of this energy could be captured and converted to electricity, 6,700 GWh of annual energy could be delivered from just the coastline of this Island, which, as an example is enough to power 625,000 homes for a year. In addition to electricity for use in the grid, this energy could also be used to drive water pumps and desalination systems.

Harnessing this power requires mechanisms which can convert wave motion into a more conventional form such as rotation to run a generator. Such is the purpose of wave energy converters (WECs). Serious WEC research started in the 1970s and since then there have been a wide range of WEC designs ranging from buoys rolling atop waves to run a generator, to structures using wave-driven air to run a turbine. While various classification systems for WEC devices have been proposed, the reader is referred to the classification framework of Pecher and Kofoed [9, Ch.

1], who classify WECs based on their shape, location, and working principle. Two aspects all WECs have in common are that they employ a system to capture wave power and another to convert that power to electricity commonly referred to as the Power Take-Off (PTO) device. In this research it was necessary to focus on a single class of WEC called point absorbers due to the operational variations across all WEC devices. Point absorber designs also vary significantly, with various PTOs, hull geometry, moorings, etc. However, they share the same operating principles and assumptions, so they all fit within the same mathematical model.

1.2 Point Absorbers

The simplest type of point absorber is the Single Body Point Absorber (SBPA), which consists of a floating body (hereafter referred to as the "float") that captures wave energy as it is driven by the waves. Energy capture is realized by the transformation of wave motion to useful motion of the WEC, which drives the PTO and produces useful power in the form of electricity. In the case of an SBPA one end of the PTO is fixed to the ground and the other to the float. Some examples of point absorbers are shown in Figure 1-3, they are the CETO 6 designed by Carnegie [10], and CorPower's WEC [11]. Carnegie's device has a disk-shaped reacting body which sits just below the sea surface. The PTO is mounted to the reacting body and connects to the mooring lines which roll up and pay out as the body moves. CorPower's device sits at the surface. The PTO is housed internally, and the device is rigidly connected to the seabed with a shaft assembly and tensioned single point mooring system. In this architecture, the float generates a force across the PTO and the seabed provides a reaction. Differences in the action and reaction forces result in extension or compression of the PTO.

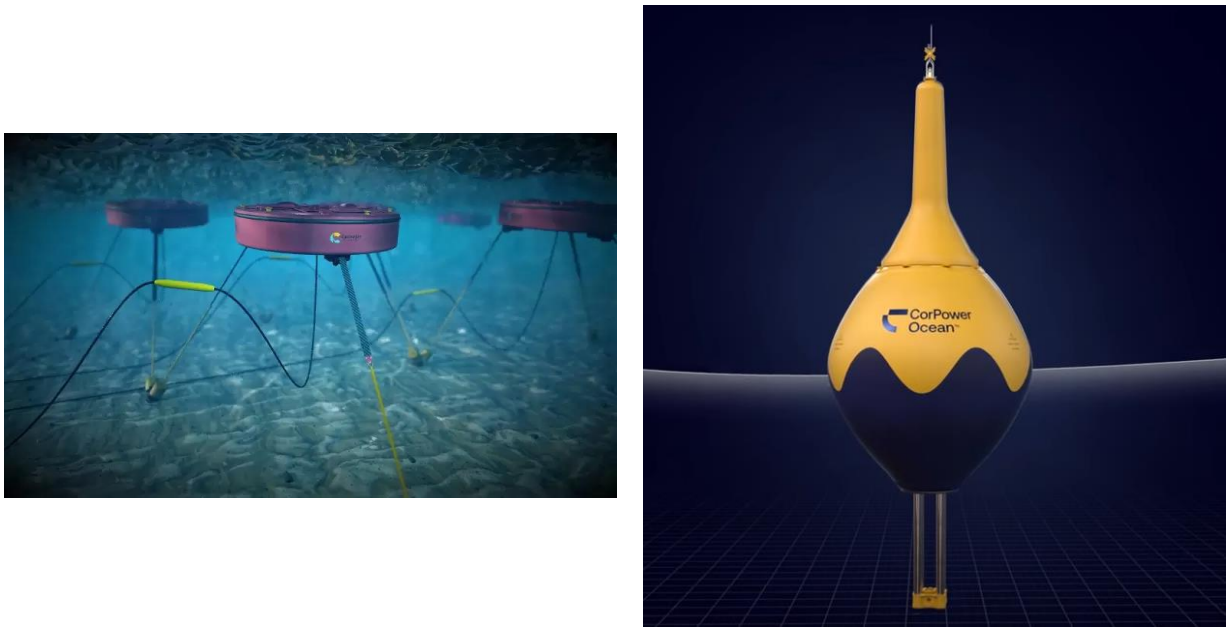

Figure 1-3 SBPAs produced by Carnegie [10] (left) and CorPower [11] (right).

A subset of point absorbers that do not require a rigid connection to the seabed are referred to as "self-reacting." As the name implies, the PTO of a Self-Reacting Point Absorber (SRPA) is connected between two floating bodies and so the action and reaction forces are provided by floating hulls and are internal to the WEC architecture. There is no reaction force that need be provided by the seabed for power generation to occur at the PTO. The first body is equivalent to the float of an SBPA, while the second floating body is usually referred to as the "spar" as it is a ballast stabilized spar type buoy with a deep draft and relatively small cross-sectional area.

Figure 1-4 SRPA produced by Ocean Power Technologies [12]

In the case of an SBPA, any motion of the float drives the PTO since it reacts against the seabed, but this is not the case for an SRPA. Relative motion must occur between the ends of the PSO for it to produce electricity, and so it is evident that the spar and float must react differently to the incident waves. Such variations in motion are achieved through greatly varied size, shape, and mass of each body. A feature of this type of WEC is that the components are self contained and require only a simple moored connection to the seafloor since the reaction force across the PTO is self-contained. Simple moored connections are rarely viable for SBPA designs since their moorings and anchors must be designed to withstand the reaction forces that develop between the buoy and the seabed where the PTO is typically mounted. One such example is the PB3 PowerBuoy designed by Ocean Power Technologies consisting of a small buoy and a tall spar which houses batteries [12]. A key advantage of SRPAs comes from the potential to achieve resonance of both bodies which was shown to lead to orders of magnitude of improvement in power output with a new type of control [13]. Some examples of SRPAs are given in Figure 1-5;

they include a device which was modelled and tested by WaveBob [14], and Reference Model 3 (RM3) which is an SRPA concept proposed by Sandia National Laboratories [15]. The RM3 design is also similar in size and shape to the Ocean Power Technologies SRPA in Figure 1-4. The WaveBob and Ocean Power Technologies SRPAs were studied by Beatty et al. using a combination of mathematical and physical scale models. It was found that the Ocean Power Technologies SRPA had better annual performance with 41% greater average power due to operating effectively within a wide capture width, while the WaveBob device had a higher peak production but a smaller capture width [16].

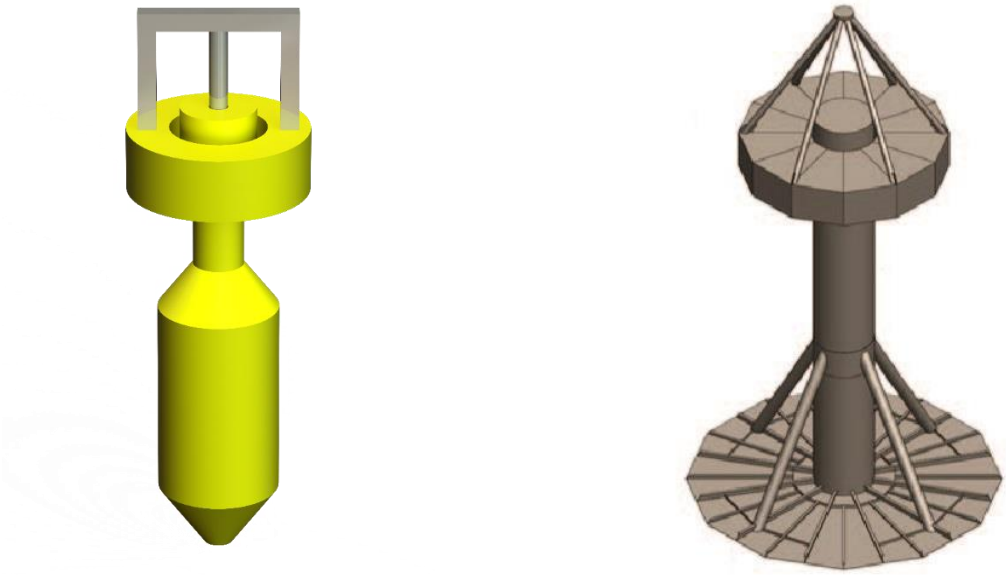

Figure 1-5 Recreated model of WaveBob SRPA [14] (left) and RM3 SRPA designed by Sandia National Labs [15] (right).

Bubbar et al. previously studied the WaveBob style SRPA and demonstrated the power capture with various control types [13]. The same SRPA is used in this work to build upon and make comparisons with that work. The WaveBob model is also advantageous as it has a much greater internal volume which can contain the PTO and any other necessary mechanisms.

1.3 Problem Statement

The potential improvement offered by SRPAs is necessary in the current state of wave energy due to the high cost of WEC systems. However, for an SRPA to be successful it must be cost-competitive with other energy sources. Wave energy converters are currently prohibitively expensive due to the high cost of deploying buoys at sea and the need for frequent maintenance in the extreme ocean environments that hold so much power. Wave energy converters and other electricity generators can be evaluated based on their levelized cost of energy (LCOE), which is the ratio of the net present value of the device to the total energy produced. The net present value of the device is calculated based on construction, operation and maintenance, and decommissioning costs. BC's energy system is 87% hydroelectric, and the LCOE of hydroelectric power in 2021 was $0.05/kWh[1] but could be as high as $0.27/kWh [17], while estimated LCOE for WEC devices in 2020 was roughly $0.57/kWh [18]. These LCOEs align with the suggestion that the LCOE of WEC devices needs to be halved to begin to be competitive in the renewable energy sector [19]. This halving could be achieved by reducing the cost of a device, increasing its design life, increasing the power it produces, or some combination of the three. Cost reductions could be achieved through the economies of scale as wave energy gains a foothold or artificially through government subsidies. Similar mechanisms can help improve the design life as the supply chain matures and operational experience develops. However, it has been suggested that a WEC designer should begin by improving WEC performance.

[1] All LCOE values are in USD.

Weber introduced two metrics: the technology performance level and the technology readiness level [20]. The performance level is a measure of the power produced by a WEC, while the readiness level reflects on how well established the market, manufacturing, and supply chains are. Weber argued that WEC designs should be improved in the early stages of design when readiness is low and the system fundamentals are still flexible before developing readiness by proceeding to physical testing and demonstration where components are difficult to change. Increasing the performance level of a WEC at low readiness suggests the need for faster simulation of WEC dynamics, more effective control, and more accurate models of WECs and peripheral systems such as moorings.

Despite the current high cost of wave energy, it may soon be viable to deploy wave energy systems in remote coastal communities which are dependent on expensive diesel. A study from 2020 found that if the LCOE of wave energy could be reduced to $0.41/kWh it could be a viable alternative energy source to coastal communities currently strictly reliant on diesel generation [21].

1.3.1 Improving SRPA Performance Through Control

Control is currently the most prevalent topic in SRPA research due to the substantial energy gains which can be achieved through control optimizations. As discussed previously, to compete with commercial renewables like wind, these performance gains are necessary for WECs to compete in the renewable electricity market. The principle of control for an SRPA is to bring the relative motion between the spar and the float into phase with the force across the PTO. If the WEC is in phase with the waves it can draw more power from each wave akin to pushing someone on a swing. If the push from a wave opposes the motion of the WEC it loses power to the wave rather than capturing it. In the case of an SRPA, the key parameters are the relative velocity u_r of

the PTO terminals and the force acting through the PTO. The relative velocity and through force result from the individual motions and wave forcing on each body.

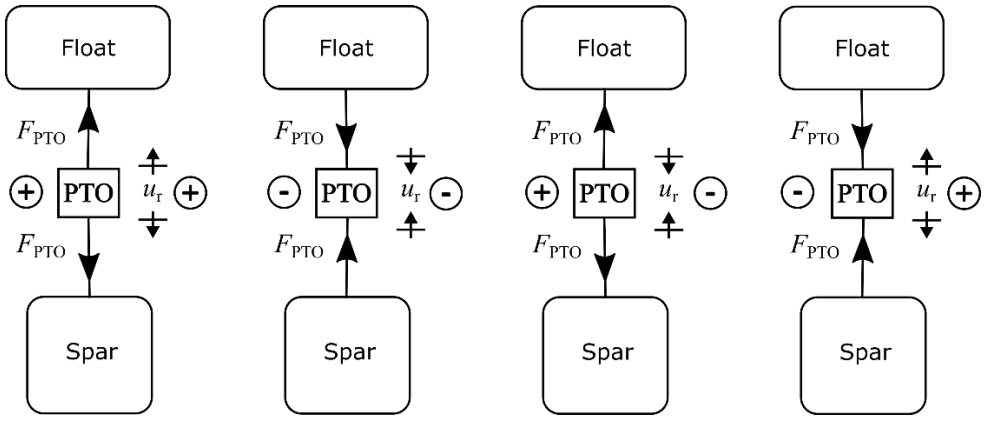

Figure 1-6 Possible combinations of forces and velocities across PTO.

If the force and velocity oppose each other, the PTO does work on the wave and power would be drawn from the PTO rather than producing it. When the force and velocity are in the same direction, and in phase, this maximizes the work done on the PTO by the wave and consequently also the power captured. In the context of wave energy, when the force and velocity are in phase, the WEC is said to be in *resonance*. Optimizations may be achieved through physical adjustments to the PTO, the spar, the float, or some combination of those three. Such adjustments are herein considered to change the *type* of control. However, these optimizations can also be pursued at various levels of fidelity, being active or passive control *approaches*.

Passive control consists of changing the control parameter to a single value for the current sea state so that the WEC resonates with one frequency of the wave spectrum. Setting the control variable to one value effectively "tunes" the WEC to a frequency which it resonates at. Under this control approach energy is extracted from the wave frequencies near where the system is tuned to, and less power is extracted from frequencies beyond this range.

Another approach is active control. Active control is achieved by optimizing strokes of the PTO on a wave-to-wave basis. Active control requires constant adjustment of the control variable for each wave, generally achieved with a feedback loop and prediction of oncoming waves. Although there is much research in this facet of control, optimal active control is yet to be fully realized. Passive control is used in this work since it is easily interpreted and to provide a reasonable expectation of power output with current control methods.

After the control approach, there is also a choice to made about the type of control, which are based on the capabilities of the PTO. However, the types of control are most clearly understood for an SBPA; as such they are introduced in that context. The bridge from SBPA control to SRPA control is introduced in Chapter 2 and the types of control are expanded upon in Chapter 4. The simplest type of control is known in the wave energy community as latching [9]. Latching control improves the power captured by a PTO by locking and releasing the PTO. This action serves to align the WEC motion with the force of the waves when it otherwise would not. In idealized studies of WEC control, the PTO is considered a controllable device built from basic mechanical components such as masses, springs, and dashpots. Amplitude control is used when the PTO can be controlled but is functionally only a dashpot and maximizes the useful power given that the WEC is not at resonance [22]. A WEC operating under amplitude control is only ever in phase with the waves and resonates at its natural frequencies ω_d since varying the damping of a dashpot c has a limited ability to change those natural frequencies.

$$\omega_d = \sqrt{\frac{k}{m}}\sqrt{1-\frac{c}{2\sqrt{km}}} \tag{1.1}$$

The stiffness, k, of a WEC is a culmination hydrostatic balance, and any elasticity of the PTO and moorings; while the mass, m, represents the actual mass of the WEC and the mass of any water that it displaces as it oscillates. By introducing controllable springs or masses to the PTO to enable making adjustments to k and m in equation (1.1), one has much more control over the frequencies the WEC will resonate at. One control type which utilizes the idea of controllable masses and springs is called complex-conjugate control for the mathematical relationship which defines the control type [23]. Of particular interest is a step adjacent to complex-conjugate control where the PTO consist only of a controllable dashpot and operates under amplitude control, while a separate device consists of the controllable mass and spring elements. This control method is of interest as it was shown to result in orders of magnitude more power production at some frequencies by changing the resonant mode shape for a particular SRPA design [13]. This type is commonly known as master-follower control, and was first discussed in detail for use in WEC design by Price et al. [24].

At this stage, WEC researchers have mainly focused on amplitude and complex-conjugate control of the PTO, but others have suggested that master-follower control may be achieved by controlling the mass and stiffness of the WEC through the geometry of the float or spar. Thus, this control type is also referred to as geometry control. Wang and Ringwood suggested pumping ballast in and out of a WEC to optimize the geometry via the mass of the WEC for power capture [25]. By changing the geometry, the impedance of the WEC is changed, and the force response due to motion changes in turn. Bubbar et al. proposed starting from the force response which would cause resonance, determining its impedance, and observing the effective change this force-source has on the geometry [26]. Both methods suggest the geometry may be controlled to maximize

power with the PTO control set to optimize given the resulting dynamics. This additional controller was shown to drastically increase the power captured by an SRPA [26], and is studied further in this work.

1.3.2 Effects of Moorings on Performance

Mooring systems have been heavily researched for seakeeping applications such as in the oil and gas industry. However, the design criteria of a mooring for a WEC are significantly different from that field. A mooring which holds the WEC in place would lead to minimal power production for example. Moorings have also been studied in the context of wave energy, but little research has been done on their effect on power capture and control of WECs.

A standard approach in the wave energy community is to treat the mooring as a simple spring under the assumptions that the body motions are small and the mooring has much higher natural frequencies than a wave spectrum [27]. Although, moorings have also been characterized in more detail for frequency domain analysis of SBPAs [28], [29]. Further work by Davidson and Ringwood describes various approaches to modelling a mooring including methods in the frequency domain and using system identification [30], which was employed by Cerveira et al. to show that a representative mooring as part of an SBPA had little effect on power capture [31]. The result that a mooring has a small effect on WEC power was also found by Muliawan et al. with time domain modelling [32]. These results provide the basis for using simplified mooring models or neglecting them altogether in the study of WEC design and controllers.

The sensitivity of WEC performance to moorings has been studied to a degree, but some gaps in that knowledge have not been pursued. Most studies are specific to certain mooring line arrangements and provide little insight into a process for considering other moorings when they

do. Another gap is what benefits may be realized when the WEC controller operates with knowledge of the mooring dynamics. Since control is vital to the optimal operation of a WEC, it seems logical that the controller should have an accurate model of the dynamic footprint of a mooring. For example, even aside from the motion of the mooring, adding one increases the mass of the system, which obviously changes the natural frequency of the WEC. These potential impacts warrant some investigation into how the PTO and mooring might be related, but more complexity arises with the introduction of a second controller for geometry control. It will be shown in Chapter 2 that the second controller and mooring share a connection between the spar and the seabed, suggesting that any effect the mooring has on the overall WEC should also have a direct impact on the control system's objectives and thus affect its design. Any dependencies between the mooring and controller can be highlighted through the optimal control design.

In order to make a fair comparison between WEC systems with and without moorings to determine the impact of mooring dynamics on WEC power, those systems must be equivalent. To isolate the impact of mooring dynamics on performance, the mass of the overall system should be preserved so that any gains or losses due to straight accumulation of mass are not included. To this end, any mass added by the moorings is removed from the body it is attached to in order to maintain consistent mass in the system.

1.4 Contributions & Technical Objectives

The contributions of this thesis are threefold. First, this work provides a method to characterize a mooring system's dynamic influence on SRPA motion and power conversion. Moorings are treated as having unavoidable or unimportant impacts, but their negative impacts may be reduced by including them earlier in SPRA design. Using this characterization process, a

linearized mooring model may be formed for various designs while remaining consistent with the mathematical framework used to assess SRPA performance in the early stages of the SRPA design process.

The second contribution is an approach for designing the SRPA control system which incorporates the mooring. This approach is applied to four different mooring designs and is independent from the shape of the mooring. Using this approach resulted in significant SRPA power performance improvements – demonstrating that the current approach of neglecting the mooring system until late in the design process unnecessarily detracts from the potential power capture of an SRPA which has a negative impact on its LCOE.

The final contribution is to provide confidence that master-follower or geometry control is advantageous in a realistic sea. Sea-state data from off the West Coast of Canada is used as an input to frequency domain simulations. The sea-state data is also combined with the mathematical model of the SRPA and mooring to determine the optimal setpoint for passive control. The SRPA model, sea-state, and optimal setpoint for passive control are then used to generate annual energy production estimates for the three control types. The annual energy production from each type indicated that the competitive advantage of master-follower control seen in previous studies is not eroded in a realistic sea.

To realize these contributions, the following technical objectives must be achieved:

1. To present a process for characterizing mooring dynamics; specifically, quantifying the mechanical impedance of a mooring through a system identification approach with high-fidelity mooring simulation data as an input.
2. To determine if including a mooring model in early design of SRPAs may lead to performance gains or changes to the design of the amplitude, complex-conjugate, or master-follower controllers.
3. To assess if the competitive advantage geometry control has over other types is eroded in a realistic sea by computing the annual energy production of a moored SRPA with common control types in a polychromatic sea.

1.5 Thesis Structure

Chapter 2 introduces the mathematical framework used in this work to relate incident wave frequency and height to a heave response of the WEC. This framework makes use of mechanical circuits and is also the basis for the theory used to determine how to tune the response of a WEC. SBPA and SRPA dynamics are introduced and related to circuit components. The SRPA model and data used throughout this thesis is introduced. The concept of an SBPA equivalent to an SRPA is also introduced in this chapter and is largely literature review of previous research.

Chapter 3 covers the theory and process used to find the mechanical impedance of a mooring system for use in the mechanical circuit of the SRPA. Four mooring configurations are presented and the merits of various characterization approaches to determine the relationship of impedance to wave frequency are discussed. Two approaches are compared in this work. One applies the linear circuit expression for an impedance to find an impedance block which is equivalent to the

mooring. The other takes advantage of the finite element mooring model used to find the impedance of sections of the mooring. A general circuit model of a multi-block mooring is introduced for this purpose. These approaches are compared and the merits of each are discussed.

Chapter 4 introduces the control types studied for the SRPA and reiterates how the mooring may impact each of them. The expressions for the three types of control are sourced from previous literature and presented. The process used to make linear, frequency domain power calculations is described. Finally, the impacts of the mooring on useful power and the controllers are presented and discussed.

Chapter 5 analyzes the performance of an SRPA with a mooring in a realistic sea while operating under each of the three control types presented in Chapter 4. The assumptions necessary to perform this analysis within a frequency domain study are discussed and a heuristic for implementing a passive control approach in a polychromatic sea is introduced. A procedure for computing the annual energy production of an SRPA is described, and the annual energy productions of SRPAs operating under the three control types are compared to guide insight into the potential for geometry control and to check if the performance is significantly eroded by the mooring.

Finally, Chapter 6 summarizes the content of this thesis and suggests avenues for future work stemming from questions raised in this work.

Chapter 2

Heave-only Mathematical Modelling of SRPAs

Mathematical models are used to describe systems in a definite way so that they can be optimized deterministically. Such models are formed with an understanding of the system dynamics and the application of simplifying assumptions to fit the dynamics to a mathematical framework. The mathematical modeling framework used throughout this work is that of mechanical circuits. An assumption which applies to mechanical circuits is that the system dynamics are linear. Linearity restricts the resultant force of each circuit element to be proportional to only one of: position, velocity, or acceleration. The result of that restriction is that each circuit element will oscillate at the frequency of excitation, but may differ in the amplitude or phase of their response. In the frequency domain it is logical to study each frequency individually, so the inputs used in mechanical circuits typically consist of a single-frequency or are *monochromatic*. Despite this limitation, the mechanical circuit representation of the SRPA dynamics provides a method to compress the dynamics into a form that is consistent with the simpler SBPA. This simpler or *canonical* form allows well known strategies for tuning the response of an SBPA for application to the control of an SRPA – which is critical to applying master-follower control with an inerter. In this work, the technique is extended to include additional circuit elements which represent the mooring. Thus, through the circuit representation the influence of mooring, inerter, spar, and float on the power conversion can be well defined. The mechanical circuit representation is applied to the parameters of a real SRPA system, which are also presented in this chapter.

2.1 Introduction to Mechanical Circuits

Mechanical circuits are an extension of Newton's Second law and are established on the principle that the force applied to a body and the subsequent motion of the body are proportional due to the mechanical impedance of the body. In the case of Newton's second law the motion is defined by acceleration, and the impedance is mass. Similar expressions relating force and one of displacement, velocity or acceleration can be easily expressed for all mechanical elements such as springs and dampers. These masses, springs, and dampers form the fundamental building blocks of the mechanical circuit framework. The familiar dynamics of these mechanical elements are given below.

$$F_{spring} = \left[k_{spring} \right] x \tag{2.1}$$

$$F_{damper} = \left[b_{damper} \right] v \tag{2.2}$$

$$F_{mass} = \left[m_{mass} \right] a \tag{2.3}$$

The stiffness, damping, and mass are considered in general to be impedances which create a force due to the motion at the terminals of the element. Comparing equations (2.1), (2.2), and (2.3) with (2.4), one may observe the parallel with Ohm's Law, showing the similarities between mechanical and electric circuits:

$$V = \left[R \right] i \tag{2.4}$$

Comparing these expressions, the force appears to be analogous to voltage, but in mechanical circuits the motion is selected as the voltage or *across* variable. The true comparison is achieved simply by rearranging equation (2.4) into equation (2.5). Following this idea, the force is analogous to current, and is called the *through* variable.

$$i = \left[\frac{1}{R}\right] V \tag{2.5}$$

Declaring force to be the through variable is straightforward if one considers forces to be the reaction to motion. If a body with a spring is displaced the stiffness of the spring generates a reaction force, the same holds for the damping of a damper and velocity, and the mass of an accelerating body. From this perspective, force is the response of a circuit element to motion. Since these forces act to resist or impede motion, the stiffness, damping, and mass coefficients are referred to as the *impedance* of each element.

With force defined as the through variable, motion must be the across variable. However, motion is not a single quantity, but is typically defined in terms of position, velocity, and acceleration. However, these terms are all algebraically related as sequential derivatives in time, so a choice of which to standardize on is necessary. In this work, velocity is selected as the across variable, but note that any choice is valid and just requires slightly altered mathematical accounting. Expressions for position and acceleration are easily written in terms of velocity using calculus:

$$x(t) = \int_{-\infty}^{t} v(t)dt \tag{2.6}$$

$$a(t) = \frac{dv(t)}{dt} \tag{2.7}$$

Mechanical circuits are a linear, frequency domain approach, so the Laplace or Fourier transforms are commonly applied to find the frequency domain relationship between these quantities, which are much simpler to work with and compute.

$$\mathcal{F}\{x(t)\} = \frac{1}{i\omega} v(\omega) \tag{2.8}$$

$$\mathcal{F}\{v(t)\} = v(\omega) \tag{2.9}$$

$$\mathcal{F}\{a(t)\} = i\omega v(\omega) \tag{2.10}$$

The $i\omega$ terms are grouped with the physical coefficient of the corresponding elements to form one quantity which relates force and velocity. In other words, the impedance is the transfer function between input velocity and force response. With this last insight a direct comparison between electric and mechanical circuits is given in Table 1.

Table 1 List of electric and equivalent mechanical circuit elements.

Electric	Mechanical
Current 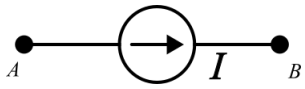	Force 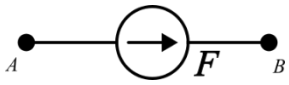
Resistance $I=\left[\frac{1}{R}\right](V_B-V_A)$ 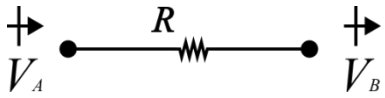	Damping $F=[b](v_B-v_A)$ 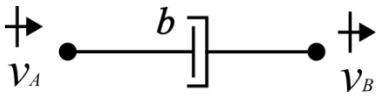
Inductance $I=\left[\frac{1}{i\omega}\frac{1}{L}\right](V_B-V_A)$ 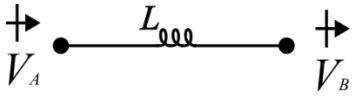	Stiffness $F=\left[\frac{1}{i\omega}k\right](v_B-v_A)$ 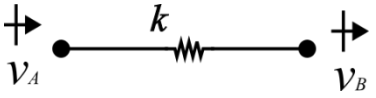
Capacitance $I=[i\omega C](V_B-V_A)$ 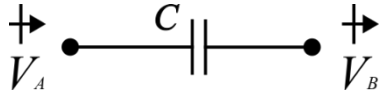	Mass $F=[i\omega m]v$ 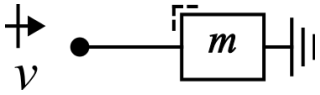
Impedance $I=\left[\frac{1}{Z}\right](V_B-V_A)$ 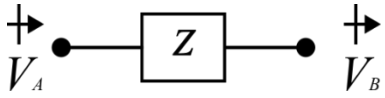	Impedance $F=[Z](v_B-v_A)$ 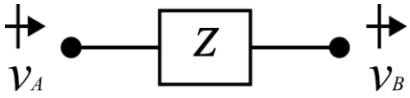

From this point, the term "impedance" is used to refer to the mechanical impedance only rather than electrical impedance. The mathematical form of the final impedance for each element is shown in square brackets in Table 1, and can be grouped in two ways. The first is to differentiate between impedances based on whether they are imaginary or real numbers. The expressions for masses and springs contain the imaginary unit i, so they are *imaginary* elements. The expression for a damper is purely real, so it is referred to as a *real* element. The second grouping is based on

whether the circuit element stores energy or not. Dampers dissipate energy and are referred to as *resistive* elements, while masses and springs can store and return energy and are called *reactive*. The choice of through and across variables leads to these two definitions forming the same groups; the terms real and resistive, and imaginary and reactive are used interchangeably in this work, but this may not always the case in other studies. When referring to a real or resistive impedance R is used to represent resistance, while X is used to represent the reactance of imaginary or reactive impedances. The impedance of a generalized circuit element is denoted as Z, and can consist of a real and imaginary part. This distinction between real and reactive components will become important when control is discussed in Chapter 4. The expression for a general impedance element Z_n is given below.

$$Z_n = R_n + iX_n \tag{2.11}$$

One other difference between electric and mechanical circuits jumps out in Table 1. Mass elements are unique in that they can only ever have one velocity associated with them and so only have one node to connect. The other node of a mass is always attached to ground. That ground connection exists because the acceleration of a mass is tied to an inertial reference frame and only has one motion, or across variable associated with it; while the compression of a spring or damper depends on the position or velocity of both ends which may be connected to ground or another circuit element. This property is useful and is employed by Bubbar et al. in the design of the SRPA control system to provide an artificial connection to ground [13], which is discussed further in section 2.5.2. However, if mass is not a true analog to a capacitor, there should be another element which is. This element should generate a force proportional to the acceleration difference of two end nodes rather than one. Smith describes the mechanical circuit element which replaces mass in

Table 1 as an inertia-based element which rotates in place as each node moves [33]. A simple realization of this element is a flywheel mounted in a casing and driven by a rack and pinion as shown in Figure 2-1.

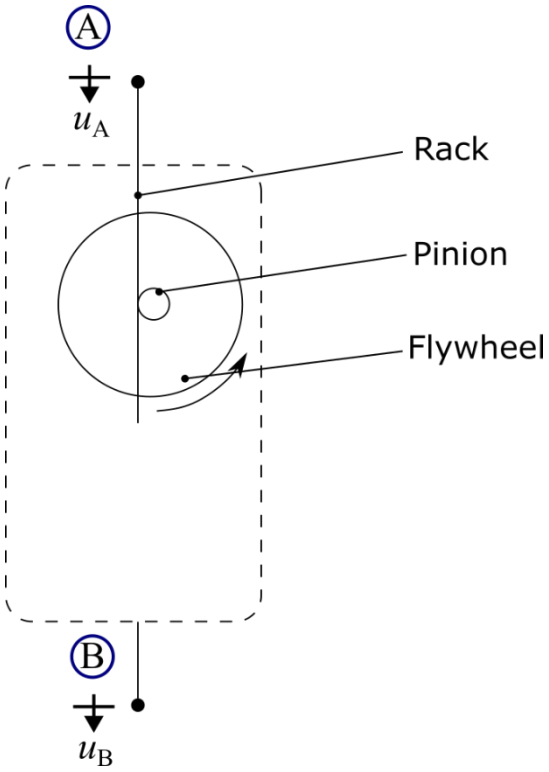

Figure 2-1 Example of inerter system comprised of rack and pinion-driven flywheel.

One node of the element in Figure 2-1 is connected to the rack, and the other to a casing fixed to the shaft of the pinion and when either end is accelerated the speed of the flywheel changes resulting in an inertial force. This device is an example of an *inerter*. The impedance of the inerter is its effective mass m_{eff} . The effective mass of an inerter is a function of the ratio of linear motion across the inerter to the rotation of the flywheel β and the inertia I of the flywheel:

$$m_{eff} = \beta^2 I \tag{2.12}$$

Importantly, since the inertia of the flywheel cannot be negative, neither can the effective mass of the inerter, although it can reach zero through control or decoupling of the transmission represented by β.

The constitutive expression for the inerter based on its effective mass is given below.

$$F = \left[i\omega m_{eff} \right] \left(v_B - v_A \right) \tag{2.13}$$

The inerter is a key component in the design of the reactive force source. It serves to generate an inertial resistance between two moving bodies which can be controlled. The effective mass of the inerter can be adjusted by introducing a transmission between the pinion and the flywheel to vary β or by shifting masses on the flywheel to change its moment of inertia. This concept was demonstrated and tested at scale by Beatty et al. [34].

2.2 Manipulating Mechanical Circuits

A useful tool stemming from the mechanical circuit approach is the application of established circuit theorems. Thevenin's equivalent circuit theorem was used by Falnes as well as Bubbar et al., and the application to SRPAs from their work is discussed in section 2.6 [35], [36]. Norton's node law may also be used to determine the sum of forces at a node. The node law is used to assemble the circuits of an SBPA and an SRPA in sections 2.4.2 and 2.5.2. It is also used in the analysis of a multi-block mooring model in Chapter 3. The superposition theorem is also applied to calculate power with multiple force sources in Chapter 5.

Another note on mechanical circuits is that circuit elements in parallel are equivalent to an impedance with the sum of the individual impedances, and elements in series sum reciprocally.

These rules are opposite to electric circuits but can be understood intuitively with a simple example using springs and position as the across variable. If a force is applied to a spring it moves some distance x proportional to its stiffness k. If a second spring is introduced in parallel to the first the displacement is halved given the same force. Thus, the equivalent stiffness of the springs is $2k$ as shown in Figure 2-2.

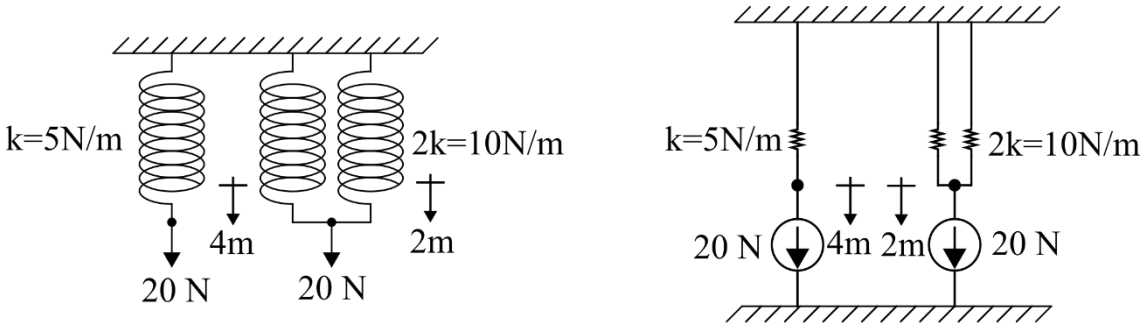

Figure 2-2 Example of springs in parallel.

If the same spring is added end-to-end in series with the first, the spring would only have doubled in length and has the same stiffness as shown in Figure 2-3, but with double the end displacement. If a spring with much greater stiffness is added in series, it would stretch significantly less than the first as shown in Figure 2-3, and the net stiffness is greater, comparatively reducing the net displacement.

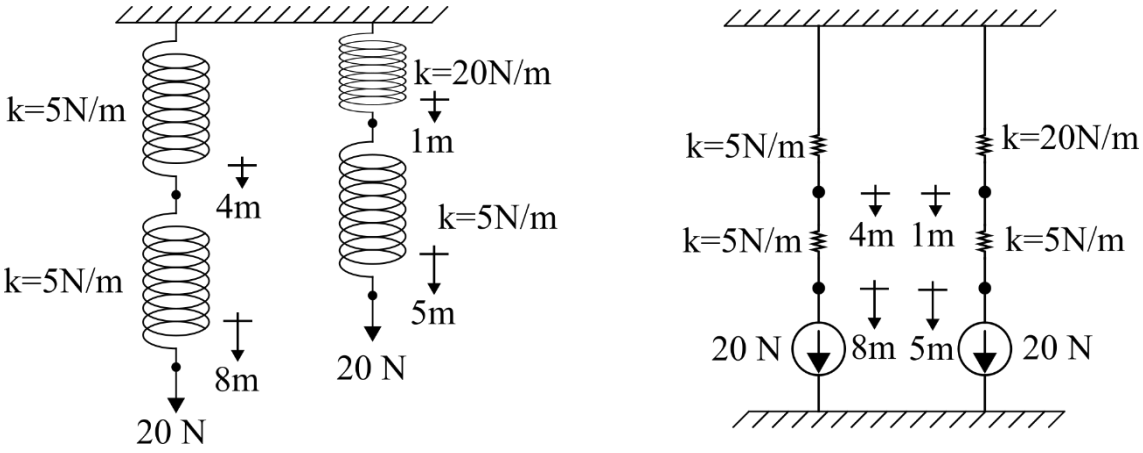

Figure 2-3 Example of springs in series.

These cases demonstrate the similarity of summing impedances in a mechanical circuit to that of an electric circuit with the caveat that the addition of parallel and series elements is swapped. The effects of combining springs in parallel and series depicted in Figure 2-2 and Figure 2-3 are also easily extended to dashpots and inerters simply by replacing the physical parameter and across variable. In fact, any circuit element can be added to another using similar intuition. For example, if one of the springs in series in Figure 2-3 were replaced with a dashpot, the steady state solution would consist of some displacement of the spring and a constant velocity of the dashpot. In fact, the impedances of the spring and dashpot could still be added together to describe the motion of the end node. These cases demonstrate the similarity of summing impedances in a mechanical circuit to that of an electric circuit with the caveat that the addition of parallel and series elements is swapped.

$$Z_{par} = Z_i + Z_j \tag{2.14}$$

$$\frac{1}{Z_{ser}} = \frac{1}{Z_i} + \frac{1}{Z_j}$$
$$Z_{ser} = \frac{Z_i Z_j}{Z_i + Z_j} \tag{2.15}$$

2.3 Heave-Only Assumption

Bodies deployed on the ocean generally experience motion in 6 Degrees of Freedom (DOF) due to the limited ability of a mooring to constrain their motion. However, in this work the dynamics have been simplified to just the heave or vertical DOF. This simplification is made for two reasons. The first is that this DOF is where the power is generated. Since the SRPA studied is designed to operate in heave it follows that if it performs poorly in 1DOF it will also perform poorly in 6DOF motion. The second reason is to home in on the basic interaction between the WEC, the inerter, and the mooring without needing to unravel added complexity from additional DOFs. Another perspective is that taking incremental steps and starting by forming an understanding of a 1DOF WEC and mooring, one may have additional insights in higher DOF analyses. Ortiz et al. performed an optimization of power on an SRPA moving in 6DOF using aspects of the mooring design as the optimization variable and showed that the mooring can serve to restrict motion in other DOFs, which makes this assumption more realistic [37].

2.4 SBPAs

Although SRPAs are the focus of this work, an understanding of previous work on SBPAs is fundamental for the optimal control of the SRPA model. The optimal control laws for the PTO of an SBPA are provided by Falnes and Kurniawan [38]. These laws improve useful power by enforcing conditions which optimize the amplitude and/or phase of the SBPA response to excitation. Falnes et al. also showed that an equivalent SBPA can be found analytically for any

SRPA [35]. This principle was later reproduced by Bubbar et al. and repackaged in the context of a mechanical circuit [36]. Being able to find the equivalent SBPA of an SRPA is key as it allows using the optimal control laws defined for SBPAs in the study and control of SRPAs.

2.4.1 SBPA Dynamics

SBPA dynamics are driven by the interaction of the body with the sea. The key hydrodynamic forces are due to waves moving the SBPA and the SBPA generating waves in turn. The force driving SBPA motion is the excitation force F_{ex} which is the force the passing waves exert on the body. The excitation force is split into the Froude-Krylov force F_{FK} the body would feel if the wave passed through it and the body did not move, and the scattering force F_s accounting for how the presence of the floating body changes the wave.

$$F_{ex} = F_{FK} + F_s \tag{2.16}$$

The motion of a floating body also generates waves in kind, which can be visualized by considering a rubber duck in a bath. If the duck is made to bob up and down, then it generates waves which propagate out in all directions. The same is true for all floating bodies, and the force felt by the body as it radiates waves is known as the radiation force F_R. The radiation force is generally divided into a component due to added mass and another due to radiation damping. Added mass describes the force felt by the body from the fluid it pushes out of its path as the body oscillates. The radiation damping term accounts for the energy leaving the SBPA through radiated waves.

Another set of forces acting on the SBPA are gravity and buoyancy. Their effects are expressed in terms of constant gravitational force mg, the buoyancy at the mean position $F_{B,mean}$,

and a hydrostatic force F_k which is felt when the body moves from the mean position. The hydrostatic force is zero when the weight of the body is balanced by the water it displaces at its resting draught. It behaves like a spring, providing a restoring force which brings the body back to the mean position.

The final force relevant to the SBPA is the reaction force of the PTO F_{PTO}. This force is generally the focus of studies on control as the impedance and resulting force can be controlled with a transmission or a similar device.

The equation of motion for a floating body with the listed forces is given below.

$$ma(t) = F_{ex}(t) - F_R(t) + F_{B,mean} - mg - F_k(t) + F_{PTO}(t) \tag{2.17}$$

Herein the WEC dynamics are approached in the frequency domain. The reason for working in the frequency domain is to take advantage of linear mechanical circuits. The limitations of a frequency domain study are that any solutions are only valid at steady state and provide no insight into transient effects; in addition, non-linear terms such as drag are linearized or neglected. A steady-state frequency domain solution also implies that oscillations are about equilibrium and constant forces are not included. For example, hydrostatic balance about equilibrium is present, but the actual forces of gravity and buoyancy which would bring a floating body to equilibrium cannot be included, and instead the body simply oscillates about its initial position. Applying these assumptions to the time domain expression and writing the acceleration term as an inertial force F_m provides a starting point for the frequency domain study:

$$F_m(t) = F_{ex}(t) - F_R(t) - F_k(t) + F_{PTO}(t) \tag{2.18}$$

The equation of motion is readily converted to the frequency domain with the Fourier transform.

$$F_m(\omega) = F_{ex}(\omega) - F_R(\omega) - F_k(\omega) + F_{PTO}(\omega) \tag{2.19}$$

Since velocity is the across variable, the forces on the SBPA must all be expressed as the product of velocity and the representative impedance from Table 1.

The impedance of a mass element Z_m applies to acceleration, so the appropriate term is taken from Table 1:

$$F_m(\omega) = Z_m(\omega)u(\omega) = \left[i\omega m\right]u(\omega) \tag{2.20}$$

The excitation force is treated as inputs to the system and is left as a force source, which is analogous to a current source, as shown in Figure 2-4.

The radiation impedance Z_R is decomposed into added mass A and radiation damping b by finding the mass and damping impedances in Table 1. The total radiation force F_R is realized by a combination of the added mass force F_A, and the radiation damping force F_b.

$$F_R(\omega) = F_A(\omega) + F_b(\omega) = Z_R(\omega)u(\omega) = \left[i\omega A(\omega) + b(\omega)\right]u(\omega) \tag{2.21}$$

The hydrostatic impedance Z_k acts on position, so takes the form of a stiffness.

$$F_k(\omega) = Z_k(\omega)u(\omega) = \left[\frac{1}{i\omega}k\right]u(\omega) \tag{2.22}$$

The PTO force is left as a general impedance to be solved for. The form it takes depends on its design and how it is controlled.

$$F_{PTO}(\omega) = Z_{PTO}(\omega)u(\omega) \tag{2.23}$$

2.4.2 Expressing SBPA Dynamics as a Mechanical Circuit

Substituting equations (2.20) through (2.23) into (2.19), rearranging, and gathering the velocity-dependent terms yields the equation of motion in terms of velocity and characteristic impedances.

$$F_{ex}(\omega) = \left(i\omega m + i\omega A(\omega) + b(\omega) + \frac{1}{i\omega} k \right) u(\omega) + Z_{PTO}(\omega)u(\omega) \tag{2.24}$$

Equation (2.24) may be rewritten as a circuit model by arranging the mechanical circuit elements given in Table 1 as shown in Figure 2-4.

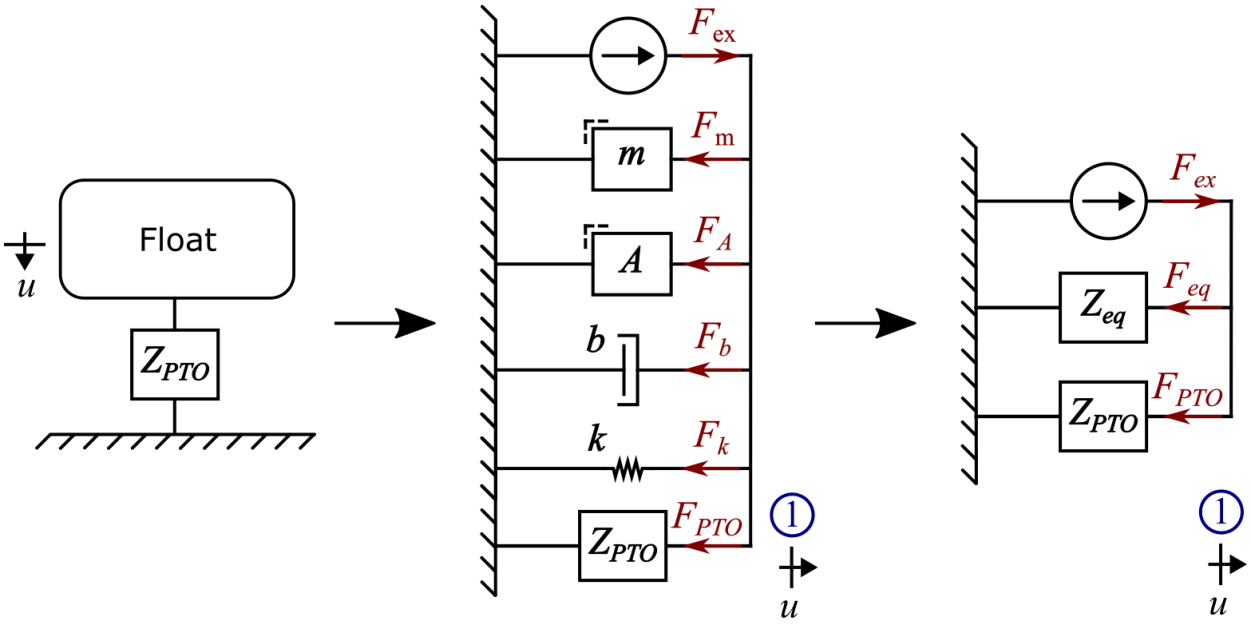

Figure 2-4 Diagram of SBPA (left), mechanical circuit of an SBPA (centre), and simplification of an SBPA (right).

A further simplification of the model can be made by grouping the impedances, except the PTO, to form a single equivalent impedance Z_{eq}. This impedance can also be considered the

intrinsic impedance of the SBPA hull – it is the impedance resulting from the physical design of the floating body.

$$Z_{eq}(\omega) = i\omega m + i\omega A(\omega) + b(\omega) + \frac{1}{i\omega}k \tag{2.25}$$

The simplest form of an SBPA consists of an excitation force, the equivalent impedance of the floating body, and the variable impedance of the PTO. It is from this form that the optimal control conditions for the PTO are defined.

2.5 Moored SRPAs

SRPAs are driven by the same nature of wave and fluid interactions, but consist of two bodies which are driven independently by ocean waves. The SBPA equation of motion and the corresponding mechanical circuit provide an important building block for the mechanical circuit of an SRPA. But there are several additional components in an SRPA device that must be represented in the circuit model. These include:

1. The excitation force and the hydrodynamic reactions associated with the additional floating body.
2. An additional reaction force caused by the mooring system of the SRPA.
3. A separate, controlled force source that represents the action which achieves the geometry change necessary for master-follower control, which is discussed further in section 2.5.2.

2.5.1 SRPA Dynamics

The equations for each body are given below with the float denoted with a subscript 1 and the spar with a subscript 2. Since the bodies are coupled by the PTO, the PTO force is positive for one body and negative for the other.

$$m_1 a_1(t) = F_{ex1}(t) - F_{R1}(t) - F_{k1}(t) + F_{PTO}(t) \tag{2.26}$$

$$m_2 a_2(t) = F_{ex2}(t) - F_{R2}(t) - F_{k2}(t) - F_{PTO}(t) - F_{FS}(t) - F_{moor}(t) \tag{2.27}$$

Equations (2.26) and (2.27) can be readily converted to their linear, frequency domain equivalents as was done for the SBPA equation of motion.

$$i\omega m_1 u_1(\omega) = F_{ex1}(\omega) - F_{R1}(\omega) - F_{k1}(\omega) + F_{PTO}(\omega) \tag{2.28}$$

$$i\omega m_2 u_2(\omega) = F_{ex2}(\omega) - F_{R2}(\omega) - F_{k2}(\omega) - F_{PTO}(\omega) - F_{FS}(\omega) - F_{moor}(\omega) \tag{2.29}$$

It is worth noting that the motion of spar and float in proximity are not independent as is suggested by the lack of any velocity coupling terms in equations (2.28) and (2.29) – none of the hydrodynamic quantities in equation (2.28) depend on the motion of body 2 and none of the hydrodynamic quantities in equation (2.29) depend on the motion of body 1. An additional force should be felt by each body when the other body moves due to radiated waves. For example, a wave radiating from the spar would necessarily interact with the float. These interactions are generally referred to as cross-coupling. The effects of cross-coupling are not included in the model used in this work as a study of this WEC suggested that cross-coupling has a negligible impact on the dynamics of this SRPA [16].

A summary of the forces presented for SBPAs is included here along with the additional forces to clearly show the additions. Note that in the following equations the index $i = 1, 2$ for the float and spar respectively. The inertial, radiation, and hydrostatic forces are restated:

$$F_{mi}(\omega) = Z_{mi}(\omega)u_i(\omega) = \left[i\omega m_i\right]u_i(\omega) \tag{2.30}$$

$$F_{Ri}(\omega) = Z_{Ri}(\omega)u_i(\omega) = \left[i\omega A_i(\omega) + b_i(\omega)\right]u_i(\omega) \tag{2.31}$$

$$F_{ki}(\omega) = Z_{ki}(\omega)u_i(\omega) = \left[\frac{1}{i\omega}k_i\right]u_i(\omega) \tag{2.32}$$

The PTO force now connects the float to the spar, so the velocity across this element is simply the difference in the velocities of each body.

$$F_{PTO}(\omega) = Z_{PTO}(\omega)\left(u_1(\omega) - u_2(\omega)\right) \tag{2.33}$$

Bubbar et al. describes a new impedance block comprised of only reactive components which can bring about the geometry changes necessary for master-follower control. This block is positioned as a connection between the spar and ground. Bubbar offers several options on how to generate this force, one of which is a system with an inerter [13]. For now, this force is expressed as a combination of strictly reactive components, such as springs, masses, or inerters.

$$F_{FS}(\omega) = iX_{FS}(\omega)u_2(\omega) \tag{2.34}$$

The mooring force is also expressed as a generic impedance Z_{moor} for now. The task of characterizing moorings and finding this impedance is covered in Chapter 3, so it is assumed to meet the requirements of a linear, frequency domain impedance.

$$F_{moor}(\omega) = u_2(\omega)Z_{moor}(\omega) \tag{2.35}$$

Substituting equations (2.30) through (2.35) into (2.28) and (2.29), and rearranging yields the equations of motion in terms of the velocity of each body and characteristic impedances.

$$F_{ex1}(\omega)=\left(i\omega m_1+i\omega A_1(\omega)+b_1(\omega)+\frac{1}{i\omega}k_1\right)u_1(\omega)-Z_{PTO}(\omega)\left(u_1(\omega)-u_2(\omega)\right) \tag{2.36}$$

$$\begin{aligned}F_{ex2}(\omega)=&\left(i\omega m_2+i\omega A_2(\omega)+b_2(\omega)+\frac{1}{i\omega}k_2+X_{FS}(\omega)+Z_{moor}(\omega)\right)u_2(\omega)\\&+Z_{PTO}(\omega)\left(u_1(\omega)-u_2(\omega)\right)\end{aligned} \tag{2.37}$$

2.5.2 Expressing SRPA Dynamics as a Mechanical Circuit

Circuit modelling is employed to visualize equations (2.36) and (2.37) as well as to determine the equivalent single-body system. As previously mentioned, finding the equivalent single body system enables the use of the optimal control expressions derived for such systems [38]. The simplification of a multi-body SRPA to a single body equivalent was originally proposed by Falnes, but was later expanded with mechanical circuits by Bubbar et al. [35], [36].

Similar to the SBPA, the expressions within parentheses in equations (2.36) and (2.37) are the equivalent impedances of each individual body.

$$Z_{eq1}(\omega)=i\omega m_1+i\omega A_1(\omega)+b_1(\omega)+\frac{1}{i\omega}k_1 \tag{2.38}$$

$$Z_{eq2}(\omega)=i\omega m_2+i\omega A_2(\omega)+b_2(\omega)+\frac{1}{i\omega}k_2+X_{FS}(\omega)+Z_{moor}(\omega) \tag{2.39}$$

With the equations of motion laid out in the frequency domain, one may form a mechanical circuit representation of the SRPA as shown in Figure 2-5. However, where it was straightforward for one body, it is not obvious how to find the total equivalent intrinsic impedance of two bodies, and the reactive force source and mooring impedances are not yet fully defined. The mooring

impedance is discussed in Chapter 3 and the reactive force source is detailed in the following section.

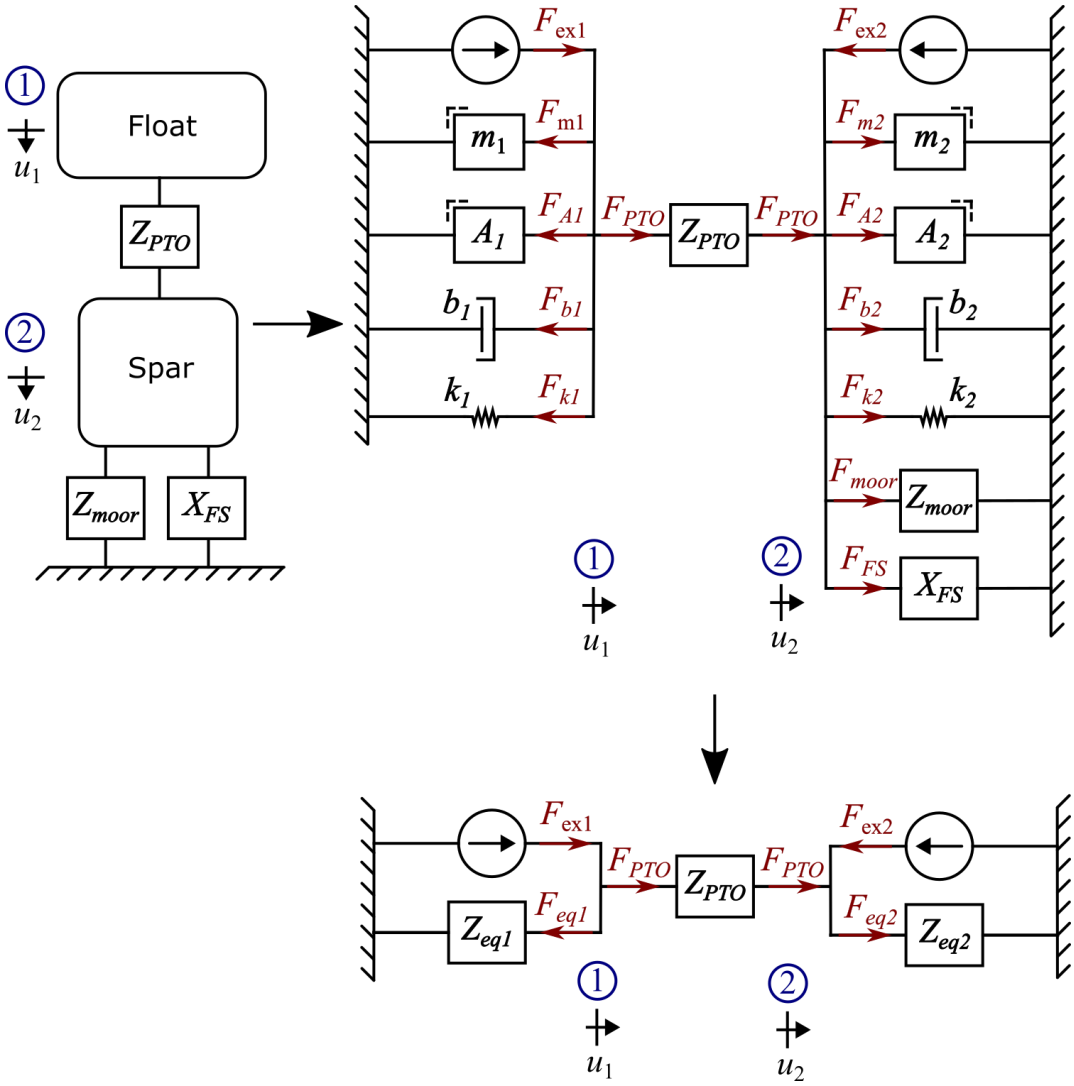

Figure 2-5 SRPA diagram (left), mechanical circuit of an SRPA with a mooring (top-right), and simplified mechanical circuit of an SRPA (bottom-right). Modified from [13].

2.5.3 Reactive Force Source

Bubbar proposed alternative designs of the reactive force source X_{FS} using reactive elements such as mass, springs, and inerters all connected to ground [13]. But an issue arises in designing that physical connection for an SRPA which is not typically connected to ground aside

from the moorings. Instead Bubbar proposes taking advantage of the inertial resistance to motion of mass. Because the inertial force associated with mass always depends on the absolute acceleration of the mass itself, it has a virtual connection to ground. This virtual connection creates a connection to ground without a physical connection to the seabed and the entire reactive force source can be placed inside the reacting body of the SRPA. Note that changing the mass of the SRPA may be prohibitively complicated, so for the reactive force source to be controllable it must also contain a controlled spring or inerter. The design proposed by Bubbar et al. consists of a constant mass suspended by a constant spring and a controllable inerter as shown in Figure 2-6 [13].

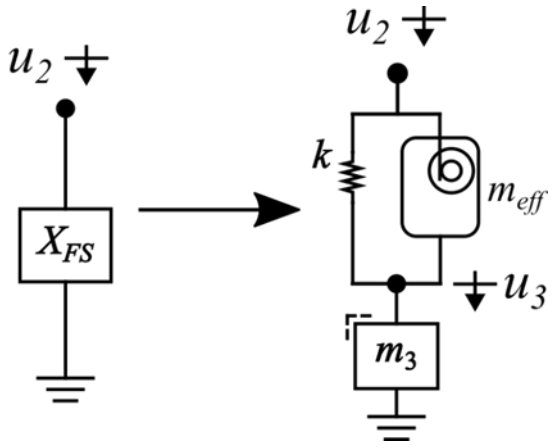

Figure 2-6 Realization of a reactive force source utilizing an inerter.

Simplifying the circuit shown in Figure 2-6, an expression for X_{FS} may be found:

$$X_{FS}(\omega) = \frac{\omega^3 m_{eff}(\omega) m_3 - \omega m_3 k}{\omega^2 \left(m_{eff}(\omega) + m_3 \right) - k} \tag{2.40}$$

Importantly the effective mass of the inerter m_{eff} is bounded by physical limitations, so could never have a negative value. This limitation is discussed in the work of Bubbar et al. [13]. However, the mooring may also influence this limit and is discussed further in Chapter 4.

While the mooring physically connects the spar to ground, the reactive force source has a virtual ground connection. Since they each connect the spar to ground, these impedance blocks are in parallel and the mooring will necessarily have some effect on this reactive force source. The topic of Chapter 3 is to characterize the mooring impedance using mechanical circuit elements so the mooring's impact on the requirements of the reactive force source may be quantified in Chapter 4.

At this point the SRPA system cannot be solved to find the optimal control as presented by Falnes and Kurniawan [38], because the optimal control is defined only for a single body with one excitation force, one intrinsic impedance, and a PTO connected to ground. If the SRPA circuit in Figure 2-5 can be reduced to a canonical form akin to the SBPA circuit in Figure 2-4, then the optimal control may be applied. The canonical form should consist of an equivalent excitation and intrinsic impedance which are equivalent to the excitation and impedance of each of the SRPA bodies. This equivalency is enforced by making use of Thevenin's theorem.

2.6 Thevenin Equivalent SBPA for an SRPA

The task of finding the canonical form of an SRPA has been studied as early as 1999 by Falnes, who demonstrated the use of Thevenin's theorem to find a single-body system equivalent to a two-body system [35]. Bubbar et al. repeated this work within the mechanical circuit framework [36]. The following presents the expressions to find the Thevenin equivalent circuit of an SRPA. The reader is directed to the work of Bubbar et al. for a full derivation [36], but an explanation of the approach and the key expressions are presented here for clarity.

Thevenin's theorem states that any circuit may be simplified to an equivalent source and impedance with the same characteristics from the perspective of a load. In terms of mechanical

circuits, this equivalency means that the single-body equivalent system preserves the force, motion, and power dissipated across the PTO of the two-body system. There are two tasks necessary to finding the Thevenin equivalent circuit: solving for the Thevenin excitation, and the intrinsic impedance. Starting from the circuit in the bottom-right of Figure 2-5, the Thevenin equivalent circuit is found by considering two special cases of the circuit and treating the PTO as the load [39]. The first is to disconnect the PTO and find the relative velocity u_{Th} between nodes 1 and 2 in Figure 2-5. Disconnecting the PTO means these nodes representing the spar and float, move independently. The second case is to lock the nodes together, which prevents any relative motion, and find the force F_{Th} which acts through the PTO.

Bubbar shows the free relative velocity $u_{r,\,free}$ and Thevenin equivalent PTO force F_{Th} found from these cases are [36]:

$$u_{r,\,free}(\omega) = \frac{F_{ex1}(\omega) Z_{eq2}(\omega) - F_{ex2}(\omega) Z_{eq1}(\omega)}{Z_{eq1}(\omega) Z_{eq2}(\omega)} \tag{2.41}$$

$$F_{Th}(\omega) = \frac{F_{ex1}(\omega) Z_{eq2}(\omega) - F_{ex2}(\omega) Z_{eq1}(\omega)}{Z_{eq1}(\omega) + Z_{eq2}(\omega)} \tag{2.42}$$

The free relative velocity and Thevenin equivalent force are both functions of the excitation and intrinsic impedance of each body and represent the motion and excitation force of the equivalent single-body system respectively. Equation (2.42) also reveals the potential to increase the force through the PTO for an SRPA over an SBPA as the two force sources become one. This increased force could lead to a much lower velocity amplitude and device travel to achieve the

same power response. Equations (2.41) and (2.42) can then be used to find the single-body equivalent intrinsic impedance Z_i:

$$Z_i(\omega) = \frac{F_{Th}(\omega)}{u_{r,free}(\omega)} = \frac{Z_{eq1}(\omega) Z_{eq2}(\omega)}{Z_{eq1}(\omega) + Z_{eq2}(\omega)} \tag{2.43}$$

By defining a new spar impedance Z'_{eq2} which does not to include the mooring impedance the influence the mooring has on equation (2.43) is made clear.

$$Z_{eq_2}(\omega) = Z'_{eq_2}(\omega) + Z_{moor}(\omega) \tag{2.44}$$

$$Z_i(\omega) = \frac{F_{Th}(\omega)}{u_{Th}(\omega)} = \frac{Z_{eq1}(\omega)\left(Z'_{eq_2}(\omega) + Z_{moor}(\omega)\right)}{Z_{eq1}(\omega) + Z'_{eq_2}(\omega) + Z_{moor}(\omega)} \tag{2.45}$$

Inspecting equation (2.45), if the mooring has an impedance comparable to the equivalent intrinsic impedance of either body it will have a significant impact on the single-body intrinsic impedance.

Note that the free velocity has been calculated and used to determine the intrinsic impedance and is not the Thevenin equivalent velocity u_{Th}. Since the circuit has a new excitation force source in F_{Th}, the input force is fully defined, but the velocity across the circuit is a variable and depends on all of the remaining circuit elements. Free relative velocity and Thevenin velocity differ due to the presence of the PTO which was assumed to have zero impedance in the calculation of equation (2.41). So, the Thevenin equivalent velocity is calculated as follows:

$$u_{Th} = \frac{F_{Th}}{Z_i + Z_{PTO}} \tag{2.46}$$

With this expression the single-body equivalent WEC and dynamics have been determined. The excitation and velocity of this new WEC are given by the Thevenin equivalents found in (2.41) and (2.42), and the intrinsic impedance is in parallel with the PTO impedance, which remains unaltered from the original circuit, resulting in Figure 2-7.

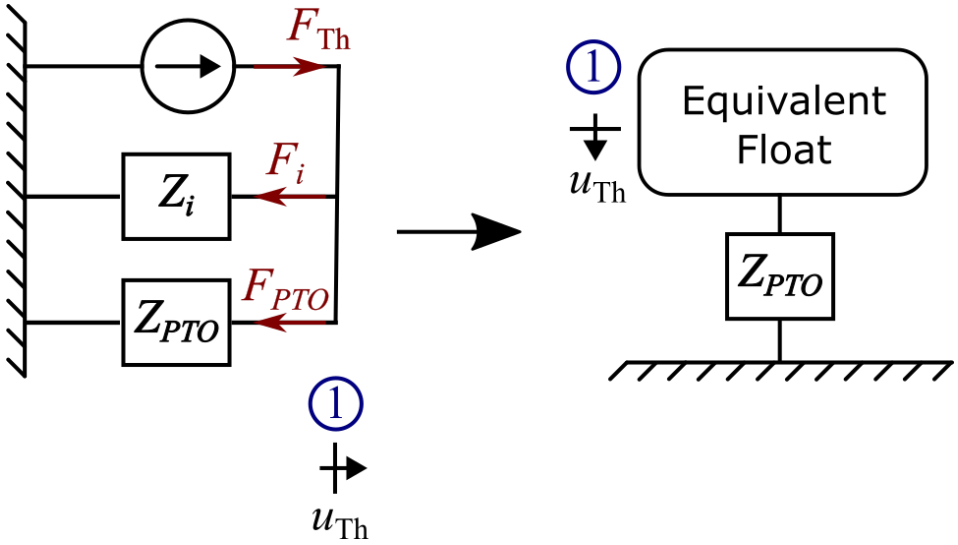

Figure 2-7 Equivalent SBPA circuit of an SRPA (left) and SBPA diagram (right). Recreated from [13].

A question that arises is why SRPAs are considered if an equivalent SBPA exists with the same characteristics and power production. The answer lies in the mathematic definition of the SBPA equivalent.

The equivalent SBPA can be imagined as having amorphous geometry which changes with frequency since the mass, radiation damping, added mass, and hydrostatic stiffness comprising Z_i may not be physically realizable as an SBPA. Meanwhile, the real SRPA has a constant hull form and can be constructed with conventional means. For example, the equivalent added mass may need to vary much more than would be achievable with a constant hull shape. Although some SBPA designs resulting from this process may in fact be constructable, the circuit provides no direction as to how to design its physical hull structure. The goal here is not to determine the

physical design of an equivalent SBPA, but rather to make use of previously derived expressions for optimal control of SBPAs. Fortunately, the shape of the equivalent SBPA is not necessarily important since the influence of the hydrodynamic coefficients of the float and spar on the single-body equivalent are defined. Since the reactive force source is embedded in the intrinsic impedance of the equivalent SBPA, that intrinsic impedance – and therefore the geometry of the equivalent SBPA – may be controlled and adjusted to increase the power extracted from the waves.

2.7 SRPA Model Parameters

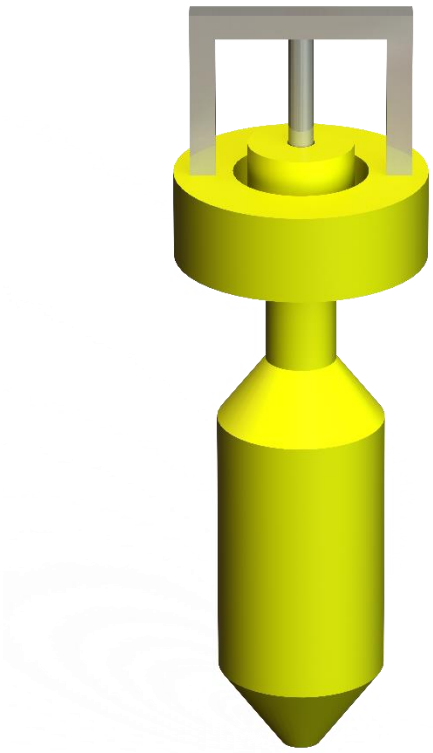

Figure 2-8 Model of WaveBob SRPA.

The model used in this work is the WaveBob SRPA, which is comprised of a toroidal float and a tall spar. This model has been studied extensively [13], [16], [26], [37], [40], so sufficient data on the device is available for use. Beatty et al. modelled this WEC at scale and compared

numerical models with experimental results for regular [40], and irregular waves [16]. A key factor for selecting this device is that the spar has sufficient internal space for the components of the reactive force source. Two further reasons for selecting this WEC are for its potential to improve in performance as demonstrated by Bubbar et al. [13], [26], as well as readily available models and parameters from Ortiz et al. [37] and Beatty et al. [16], [40]. The model parameters are derived from characterization of the physical scale model completed by Beatty et al. [40], and scaled to full scale by maintaining a constant Froude number.

$$F_r = \frac{v}{\sqrt{gD}} \tag{2.47}$$

As discussed by Beatty [41], Froude scaling is commonly employed for floating offshore structures due to the dominance of gravity and inertia in the dynamic response of those systems. By equating the model and full-scale Froude numbers one may define the scaling parameter α to be the ratio of model to full-scale diameters:

$$\alpha = \frac{D_{full}}{D_{model}} \tag{2.48}$$

The scaling parameter used in this work is $\alpha = 25$ to return to full-scale from the modelling completed by Beatty et al. [16]. Applying this scaling factor as an equivalency between model and full-scale versions of equation (2.47) and eliminating the diameters using equation (2.48) yields the scaling factor for velocity:

$$\frac{v_{model}}{\sqrt{gD_{model}}} = \frac{v_{full}}{\sqrt{gD_{full}}} \rightarrow v_{full} = v_{model}\sqrt{\frac{D_{full}}{D_{model}}} = v_{model}\alpha^{1/2} \tag{2.49}$$

With scaling factors determined for velocity and length, analysis of the units can be employed to find the scaling for period and any other parameters of interest. Note that the scaling factors are used to transfer from model-scale to full-scale in this work; to go from full-scale to model-scale one would simply take the inverse of each scaling parameter or could redefine α .

Table 2 Scaling factors used to maintain a constant Froude number.

Parameter	**Scaling Factor**	**unit**
Length	α	m
Time	$\alpha^{1/2}$	s
Frequency	$\alpha^{-1/2}$	Hz
Mass	α^{3}	kg
Velocity	$\alpha^{1/2}$	m/s
Acceleration	1	m/s^2
Force	α^{3}	N
Stiffness	α^{2}	N/m
Damping	$\alpha^{5/2}$	Ns/m

A limitation of Froude scaling is the necessary assumption that viscous effects are negligible. This conflict arises when determining the Reynolds scaling factor for velocity. By applying the same process that was used to find the scaling factor for velocity for a constant Froude number, the velocity scaling factor for a constant Reynolds number may be found.

$$R_e = \frac{vD}{\nu} \tag{2.50}$$

$$\frac{v_{model} D_{model}}{\nu} = \frac{v_{full} D_{full}}{\nu} \rightarrow v_{full} = v_{model} \frac{D_{model}}{D_{full}} = v_{model} \alpha^{-1} \tag{2.51}$$

Since there are only trivial values of α that satisfy equations (2.49) and (2.51) simultaneously, only one of these dimensionless parameters can be maintained when scaling a WEC.

Applying Froude scaling and not maintaining the Reynolds number is a reasonable approximation for SRPAs and is commonplace in offshore system modelling [42]. Placing more importance on the Froude number than the Reynolds number aligns with the inviscid flow assumption commonly made in the derivation of the dynamics of WECs [27]. The reasoning behind the inviscid assumption is that body motion is small, and the forces contributing most to the system dynamics are inertia and gravity rather than viscosity.

Applying the parameters from Table 2 to the scale-model data characterized by Beatty et al. results in the physical and hydrodynamic parameters of the full-size WaveBob WEC [16]. The scaled parameters which are constant are presented in Table 3, and the detailed physical dimensions are provided in Appendix A – WaveBob SRPA Dimensions. The scaled parameters which vary with frequency are presented in Figure 2-9 and consist of the excitation forces $F_{ex1}(\omega), F_{ex2}(\omega)$, the added masses $A_1(\omega), A_2(\omega)$, and the radiation damping terms $b_1(\omega), b_2(\omega)$.

Table 3 Dimensions and constant parameters of SRPA studied.

	Float – Body 1	**Spar – Body 2**
Height	5.8 m	35 m
Diameter D	7.43 m	4.85 m
Mass m_i	187.5 t	1797 t
Hydrostatic stiffness k_i	1.251 MN/m	0.3184 MN/m

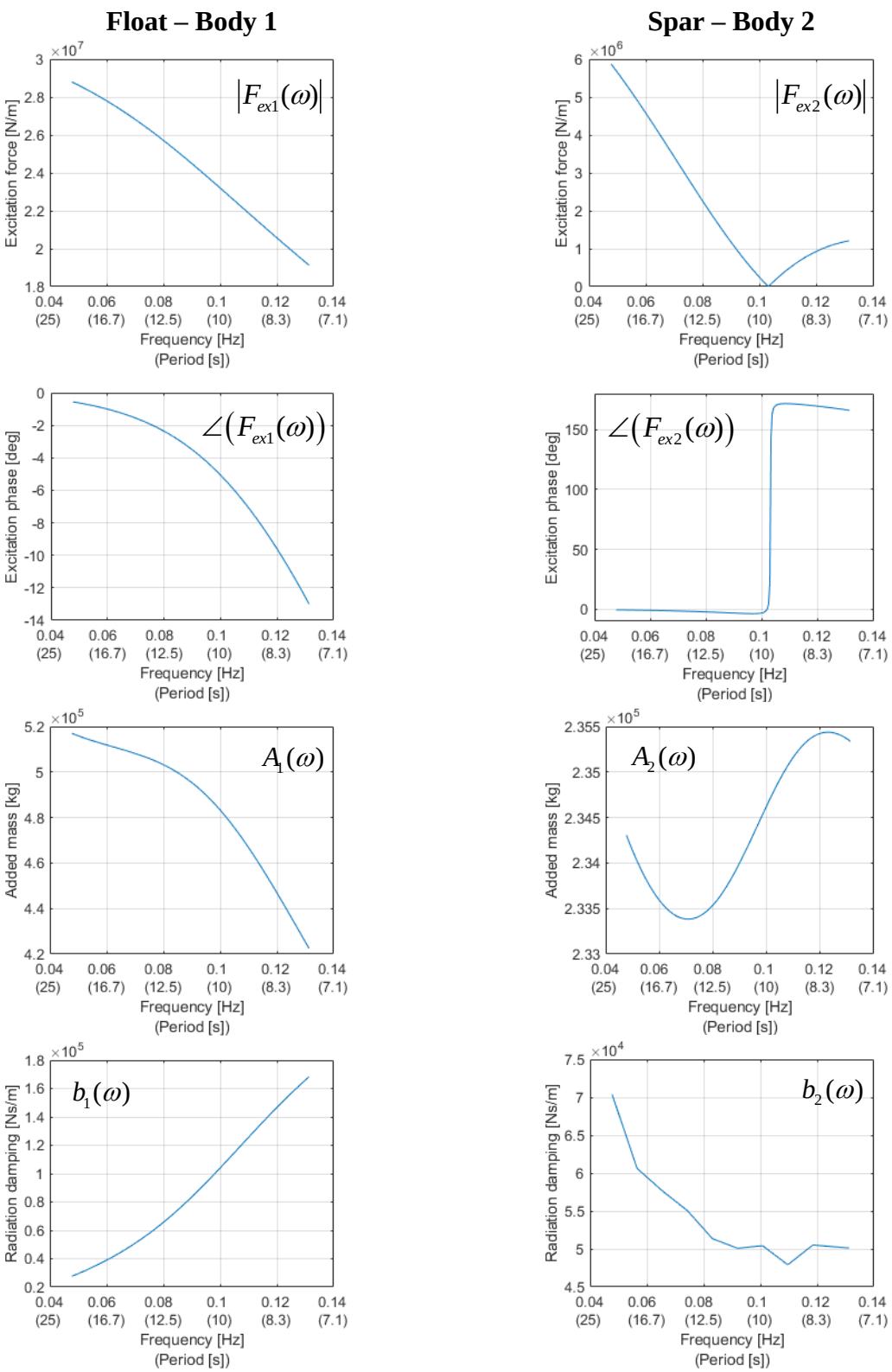

Figure 2-9 Characterized parameters of full-scale float (left), and spar (right). Data Froude-scaled from [40].

Note that the excitation forces in Figure 2-9 have a phase. This phase is a measure of the delay between a wave crest passing through the midpoint of the spar or float and the peak of the excitation force. The other parameters are mass and damping which have phases of 90° and 0° relative to body motion respectively due to their definitions as reactive and real impedances in the circuit model.

Also worth noting is the inflection point in the excitation force of the spar. The excitation force magnitude decreases to near-zero and the phase switches from 0° to 180° at 0.103 Hz. This inflection is characteristic of a change in the mode of the oscillation of the body and affects the useful power and control further on.

Most of the data presented in Figure 2-9 is sourced from Boundary Element Method (BEM) characterization of the bodies completed by Beatty et al. [40]. The hydrodynamic parameters of the float and spar can easily be computed at any frequency with the BEM analysis and would permit studying the SRPA response, power, and control at any excitation frequency. However, it was found that the BEM results for the radiation damping of the spar were two orders of magnitude less than from physical testing due to viscous damping [40]. Beatty et al. ran these discrete physical tests between 0.045 Hz and 0.13 Hz [40][2], so the data which is considered more accurate is limited to this range. The choice made in this work is to use the physical test data, since that data contains an important physical factor which would otherwise be neglected. This choice comes with the

[2] The work of Beatty et al. was for a 1/25th scale physical model and has a different frequency range as a result. This range has been converted to full-scale frequency for clarity as only full-scale values are used in this work.

limitation that the frequency domain analysis of the SRPA is restricted to be between 0.045 Hz and 0.13 Hz.

Chapter 3

Mooring Characterization

The goal of this chapter is to demonstrate and discuss methods of characterizing a mooring in a way that facilitates representation of the mooring dynamics in a mechanical circuit. In Chapter 4, these characterizations will be used to investigate any effect the mooring may have on the design and performance of the inerter system as a means to tune the WEC response across a broad range of wave frequencies.

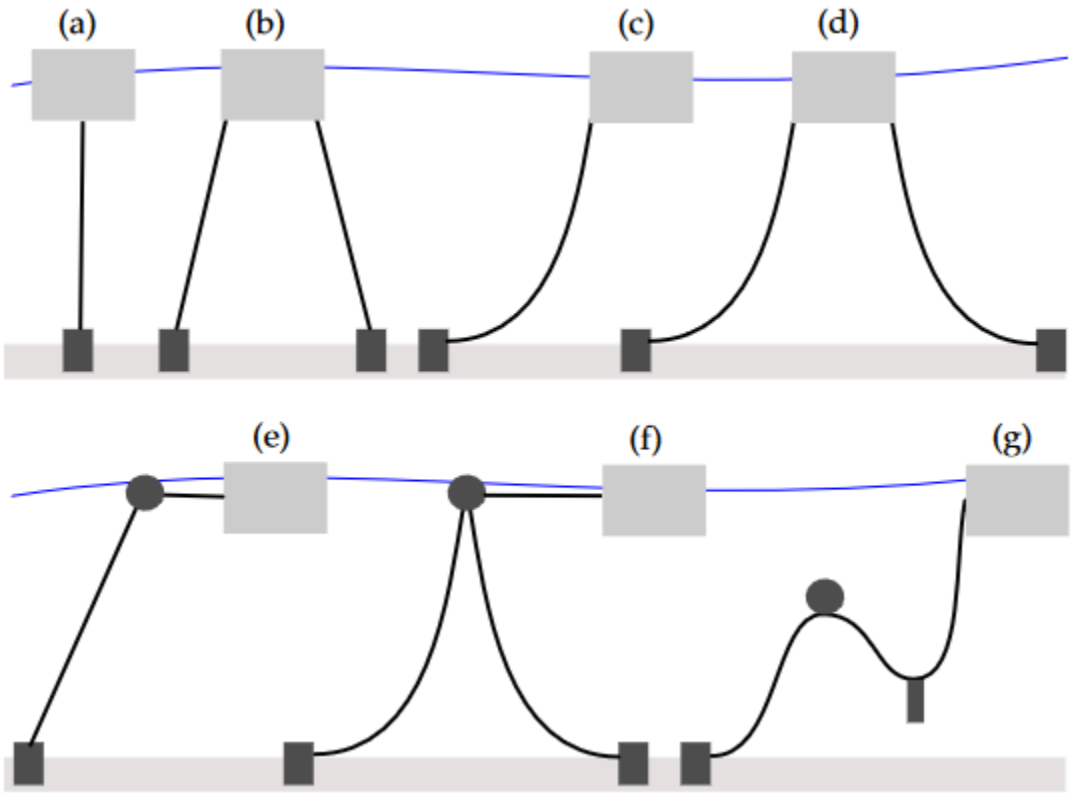

Figure 3-1 Mooring line configurations for (a) tension-leg, (b) taut, (c) catenary, (d) multi-catenary, (e) single anchor leg, (f) catenary anchor leg, and (g) lazy-S. Figure from [30].

The purpose of a mooring is to maintain the station or position of a floating body, but this can be achieved through a variety of designs for different deployment conditions as shown in Figure 3-1 [30]. For example, a near-taut mooring may be used when the position of the body must be tightly limited such as in high-traffic areas. In another deployment condition, line floats and weights may be used to form the mooring into a lazy-S shape that lowers line tensions and allows largely unconstrained heave movement, but still serves to gently return a buoy back to its original lateral position. The lazy-S concept might be used in rougher seas where one must limit the extreme loads experienced in the mooring and anchor points. In consideration of the range of potential designs of moorings, four representative moorings have been selected and simulated in this work. Simulations are used as there are currently no means to gather the data required from a field operation to characterize a mooring. Two characterization methods discussed and demonstrated to be suitable across the diversity of moorings considered in this work. Once characterized, the mooring model may be manipulated as part of the circuit model of Chapter 2 where knowledge of the mooring may be used to refine the control design.

3.1 Mooring Forces

Characterizing a mooring in the mechanical circuit framework can be thought of as transforming the mooring dynamics into three reaction forces which act on the spar. These forces are an elastic force which is proportional to the displacement of the spar; a viscous force proportional to the velocity of the spar; and an inertial force proportional to the acceleration of the spar. Although the mooring material has its own characteristic stiffness, this is only engaged when the line is taut. A stiffness force is simply a force which is proportional to position, and as a mooring rises and falls, some of the mooring mass is lifted from or returned to the seabed. Additional mass hanging on the mooring increases tension on the WEC, and since this force is

proportional to its position, it is ultimately modelled as a stiffness. Viscous damping develops as the mooring is pulled through the water and the inertia of the mooring line adds the third force. Importantly, these physical forces actually depend on the movement of the mooring, so a phase shift between the spar motion and these responses may also be present.

3.2 Mooring Configurations

The four mooring systems considered in this work are referred to as:

a. Catenary mooring
b. Heavy catenary mooring
c. Taut leg mooring
d. Lazy-S mooring.

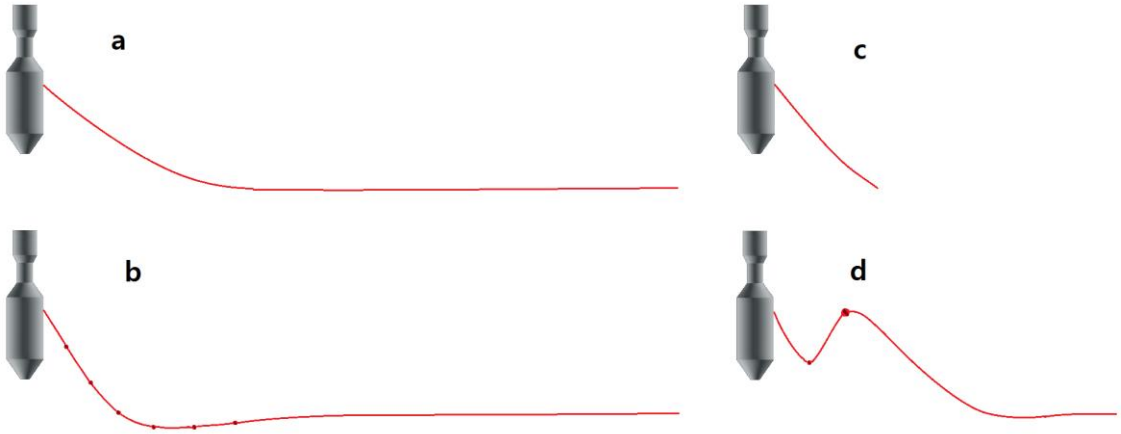

Figure 3-2 Mooring diagrams of a) catenary mooring, b) heavy catenary, c) taut-leg mooring, d) lazy-S mooring.

The catenary is an example of the most basic possible mooring which is deployed with extra chain to act as an anchor on the seabed. The heavy catenary has additional steel weights along its length to judge what effect mooring mass may have on the controllers. Counterintuitively, the taut leg mooring engages less of the geometric stiffness of the cable since none of the line rests on the

seabed. Since the taut leg mooring is not fully taut, the stiffness of the line itself is not engaged, and with no geometric stiffness due to line resting on the seabed this mooring actually has much less total stiffness than the others. This low net stiffness allows investigation of the effects of a weaker spring. Finally, the float of the lazy-S mooring supports much of the weight of the cable and most of the mooring motion occurs between the spar and the line weight in the U-shaped section which is commonly referred to as a false bottom. This mooring is included to check if the impact of the mooring is reduced with the effective reduction of the mooring length and if the characterization approach yields a reasonable result with more complicated geometry. Each mooring system is designed with four legs to represent a realistic system deployment, but only one leg is simulated for each mooring. Only simulating one leg of each mooring is acceptable as the simulations are constrained to move in heave only and the change can be accounted by multiplying resultant forces by four since each leg will have the same dynamics. A diagram of each mooring is shown in Figure 3-2, and the cable segment parameters of each are given in Table 4. The raw initialization data required by Proteus is provided for each mooring in Appendix B – Mooring Initialization Data.

Table 4 Mooring specifications.

Mooring Design	Wire Rope 8cm Ø, 40kg/m	Wire Rope 8cm Ø, 580kg/m	Dyneema Rope 10cm Ø, 7kg/m	Studlink Chain 8cm Ø, 40kg/m	Float 2m Ø, 1680kg
Catenary	65m	-	-	105m	-
Heavy Catenary	-	65m	-	105m	-
Taut leg	40m	-	-	-	-
Lazy-S	-	-	65m	50m	34m (on rope)

3.2.1 Catenary Mooring

This mooring simulation is loosely based on a design optimization completed by Ortiz [37]. The design optimization led to an edge case of mooring material with a material density that is not commonly available. The catenary model replaces that material with industry standard wire rope. A significant portion of the mooring rests on the seabed and models what might be expected for a typical WEC deployment. This design is light and has no extra features, so it is expected to have a minimal impact on the SRPA dynamics. As simulated, this mooring has 8 nodes and 7 segments.

3.2.2 Heavy Catenary Mooring

This mooring realizes the optimized mooring result from [37] by using standard mooring line with steel weights hanging along its length. The effect of these weights is that a heave motion of the spar lifts or returns a significant amount of mass to the seafloor, effectively increasing the perceived spring force the mooring provides. The weight of the mooring also causes it to sink into the silty seafloor. As simulated, this mooring has 8 nodes and 7 segments.

3.2.3 Taut-Leg Mooring

This mooring is anchored closer to the spar so that none of the mooring line rests on the seabed. This mooring would have a smaller impact on the seafloor and would be cheaper to construct than the others due to its much shorter length. This mooring is expected to have a similar impact to the catenary mooring due to the lack of external features and small amount of cable undergoing significant movement. However, since the mooring is not quite taut the stiffness of the mooring line material is not engaged and with no line resting on the seabed it has a low total stiffness. The impact of this style of mooring on a different WEC was investigated by Gubesch et al. who found it to perform well among other designs [43]. As simulated, this mooring has 5 nodes and 4 segments.

3.2.4 Lazy-S Mooring

This mooring is an example of a mooring system designed to gently correct the position of the WEC and reduce the load on the lines in rough seas. Much of the weight of this mooring line is supported by the line-float, which should reduce inertial effects by limiting the amount of the mooring which moves with the spar. A similar mooring was studied by Yang et al. who developed and validated a model for use on a WEC [44]. As simulated, this mooring has 10 nodes and 9 segments.

3.3 Mooring Simulation

The data necessary to characterize a mooring can be sourced from numerical simulations, scale modelling, or full-scale testing. Wave tank testing is time-consuming and expensive, even at small scale where the desired mooring characteristics may be difficult to achieve, so white noise or multisine approaches are generally used in these cases. However, numerical simulations are relatively cheap and simple to prepare and run. Many numerical simulations can even be run at once, greatly reducing the time commitment of generating data. Given those qualities, simulations of regular monochromatic waves are employed to gather data on the response of each mooring design across a range of frequencies.

Each mooring is simulated in the simulation suite ProteusDS to generate data for characterization [45]. Proteus simulates moorings using a finite element model by discretizing the mooring into nodes and segments. The segments are massless, while the nodes are point masses whose motions are driven by fluid interaction and tensile forces in the segments. This concept maps well to the mechanical circuit approach and this comparison leads to a multi-block mooring model. Effects simulated by Proteus include axial and tangential drag, buoyancy, tension, and

bending stiffness. These effects and how they may be modelled in a mechanical circuit are discussed further in section 3.7.

Each mooring is constructed in a finite element model using segments and nodes. A convergence analysis on the tension of the spar-mooring connection of each design was completed for each mooring design to ensure the number of nodes was sufficient. The tension profile of the topmost mooring segment was compared for simulations with increasing amounts of nodes until the tension profile converged to within 1%. As new nodes were added the segment lengths were adjusted for equal spacing across the entire mooring. This approach was adjusted slightly for the lazy-S mooring with the U-shaped section in Figure 3-2 having shorter segments to allow for the tight curvature of that region. This convergence analysis approach led to the number of nodes and segments used in each mooring design.

Each simulation contains a mooring connected to a body defined to follow a sinusoidal path with a given frequency and amplitude. These sinusoidal profiles are generated externally and loaded into Proteus to define the motion of the body as a series of waypoints. To ensure at least one full period of steady-state response is captured, each simulation is set to run for two minutes or four times the period of excitation, whichever is greater. The first third of the data is removed to eliminate any transient response as the mooring begins to move.

Although the frequency-dependent float and spar parameters from Figure 2-9 are bounded between 0.045 Hz and 0.13 Hz, there is no indication if that range is sufficient to characterize a mooring. Since the motions of the moorings are driven by tension their dynamics are substantively different from the float or spar. So, although the analysis of this frequency domain study is limited

to the (0.045, 0.13) Hz range, the frequency range of the mooring characterizations was expanded until a clear pattern emerged. This range was (0.001, 4) Hz for the four moorings studied.

A total of 320 discrete simulations of each mooring system were executed in this range with less density in higher frequencies as a pattern emerged. Simpler moorings with no line weights or floats could be simulated faster than real time at about 40 seconds per simulation, but others took up to 30 minutes to simulate two minutes of oscillatory motion. By queuing and running 15 simulations at a time the total time to generate the data for the most complicated mooring was about 10 hours, while the simplest mooring took 30 minutes.

One clear limitation of this approach to data generation is that the mooring model will only be as good as the original simulation. Although Proteus has been designed for simulating moorings, every model has its limitations and simplifying assumptions. One simplification is the finite element mooring model. The designer may choose how many segments a mooring line should have, which may lead to unrealistic behaviour due to numerical instabilities. The issue of reducing numerical effects was addressed by performing a convergence analysis on the number of mooring segments. An example of this is the resolution of tension differences at a node. When a node moves in a time step it changes the tension in the segments on either side which move the next node and so on until an end of the mooring line is reached. Tension spikes tend to travel back and forth along the cable at high frequency, introducing noise into the actual tension data. These tension spikes do not tend to occur in reality as they are quickly dampened out by fluid interactions, but this is not easily simulated numerically. Proteus approximates this with a coefficient of internal damping, but increasing it drastically increases simulation times. Generally, Proteus is a good first

step for generating a mooring simulation, but some unrealistic numerical effects may also become part of the characterization.

The steps used to characterize the mooring are described below, and detailed in the following sections.

1. Excite the system at a single discrete frequency.
2. Measure the amplitude and phase of the mooring response in terms of force.
3. Use force amplitude, velocity amplitude, and relative phase to find impedance.
4. Consider how much frequency content is rejected.
5. Repeat steps 1-4 for all frequencies of interest.
6. Generate frequency-continuous model using system identification.

3.4 Characterization Approach

The missing piece of information necessary to determine the effect of the mooring in the mechanical circuit model is the mooring impedance Z_{moor} which is expressed as a function of frequency as in equation (2.35). The aim of this section is to outline an approach to determine this function for an arbitrary mooring.

Two approaches to characterize a mooring are considered but both operate on the same principle. The first is to rearrange equation (2.35) and solve for the single impedance block Z_{moor} using equation (3.1).

$$Z_{moor}(\omega) = \frac{F_{moor}(\omega)}{u_2(\omega)} \tag{3.1}$$

This *single-block* approach compresses the effects that the motion and dynamics of all the mooring nodes have on the WEC into one impedance block. This impedance block relates the velocity of the top-most mooring node to the heave force it exerts on the spar.

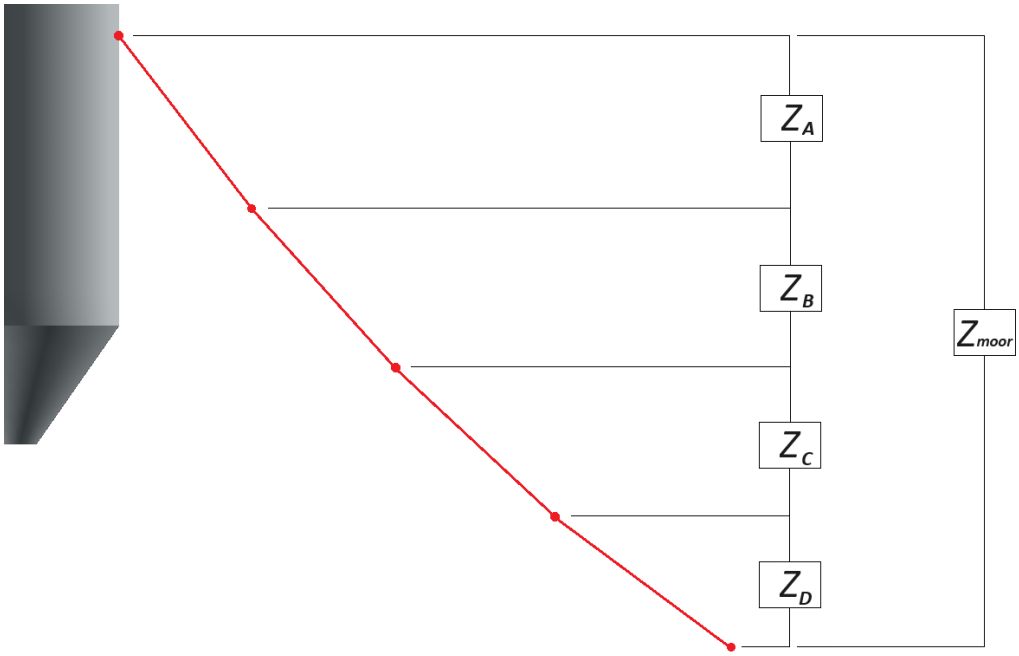

Figure 3-3 Mapping of simulated mooring to single-block mooring model (right) and multi-block mooring model (left).

Another approach to heuristically discretizing the mooring is to apply the same principle as the single-block approach and equation (3.1), but between individual mooring nodes rather than just the top and bottom most nodes. This *multi-block* approach, stemming from the segments of the finite element model of the mooring segments, results in a multi-block circuit model of the mooring. From the multi-block model, one may apply circuit theory to find the equivalent single-block impedance. This process is explained further in section 3.7.

The spectral model of a mooring may be identified by exciting the system dynamics in other ways, but there are a few reasons for using the selected method. A common method to excite a system for characterization is to employ white noise excitation [30], [46]. When white noise excites

the system across a range of frequencies the resulting data has all of the frequency content and can be decoded with system identification (SID). Another example is the multisine signal employed by Paduano et al. signal for characterizing a mooring [47]. The multisine signal is comprised of specific frequencies and amplitudes to excite the mooring dynamics similar to wave motion while having comparable energy to that which would be imparted by natural wave motion. Both these approaches would excite the mooring with a broadband input motion of the spar and then extract the resulting mooring response for the individual frequency components. The obvious advantage of these approaches over the one-at-a-time approach is that they require only one simulation or test and can be completed considerably more quickly.

However, the one-at-a-time approach is expected to provide better accuracy and completeness for two reasons. The first is that there is less opportunity for error or cross-contamination in a targeted frequency band from excitation in other frequency bands. However, due to the nonlinearity of mooring systems even a monochromatic input will lead to a broadband response. It is shown in section 3.5 that excitation of the mooring at one frequency results in a response at integer multiples of that frequency due to asymmetries in the mooring motion. In a multisine or white noise analysis the response at the multiple of the frequency would effectively be added to the response to excitations at that higher frequency, leading to error tending to increase with frequency.

3.5 Frequency Range and Motion Amplitudes

The frequency range for the mooring characterization was selected with the use of wave resource data from a representative WEC deployment site off the West Coast of British Columbia. Further information on the site and why it was selected in this work are given in Chapter 5 where

the data is primarily used. The dataset given in Figure 3-4 includes information about how often each sea state occurred with the number in each cell indicating hours per year, how energetic it is represented by the colour of each cell, as well as the significant wave heights H_{m0} and energy periods T_e corresponding with each sea state on the y and x axes respectively.

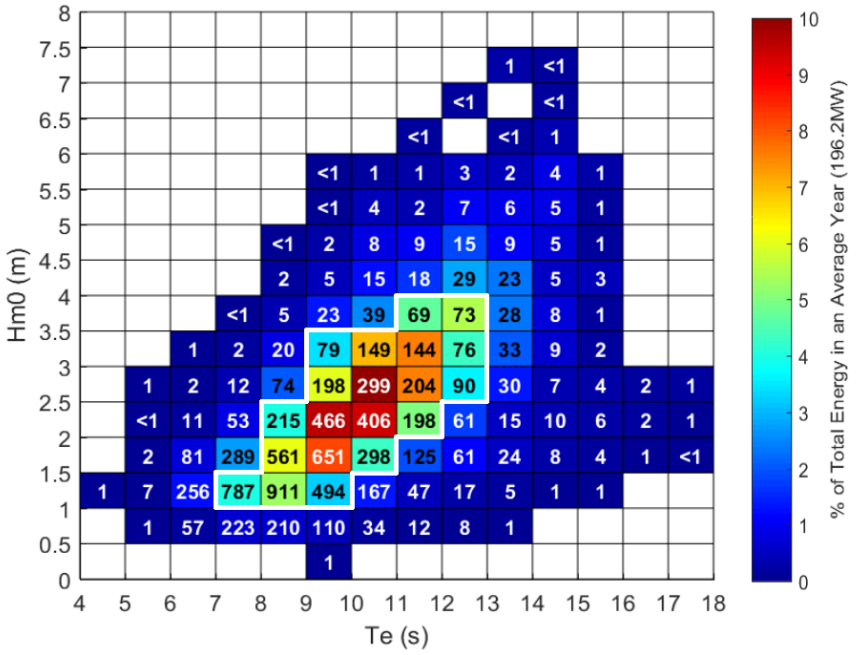

Figure 3-4 Sea state data from a resource assessment completed by PRIMED [48]. Twenty most energy intensive sea states indicated with bold outline.

The energy period and significant wave height values are noted for the twenty most energy intensive sea states. It is commonplace to represent this binned data as a single-peaked spectrum model such as Joint North Sea Wave Project (JONSWAP) or Pierson-Moskowitz (PM) [16], [49], [50], [51, p. 145], [52]. In this work PM spectra are used to model the data using equation (3.2) as PM spectra have been identified as being representative of the waves off the West Coast of Canada [53]. Energy period is converted to peak period using the heuristic $T_p = 1.25T_e$ [50].

$$S(f) = AT_p^5 e^{-\frac{B}{f^4}}, A = \frac{B}{4} H_{m0}^2, B = \frac{5}{4} \frac{1}{T_p^4} \tag{3.2}$$

Each of these PM spectra are plotted together in Figure 3-5.

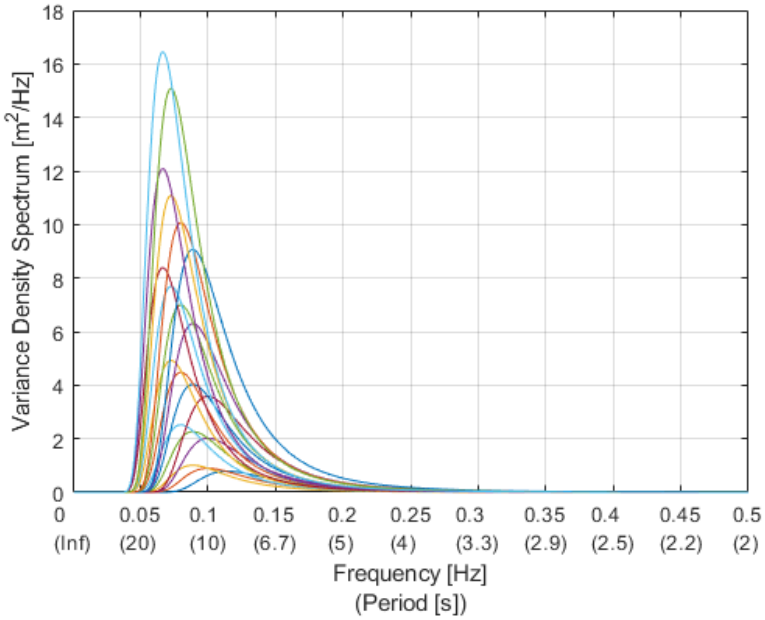

Figure 3-5 PM spectra off the coast of Nootka Island. Generated from PRIMED resource assessment [48].

Plotting these PM spectra provides an indication of the amplitude of the waves and which wave frequencies to expect. The amount of variance density plotted on the y-axis provides information on the height and energy of a wave. The range (0.045, 0.13) Hz range where data is available for the spar and float contains 90% of the variance density of all of the superimposed PM spectra. This range provides some confidence that the frequency range of the available spar and float data Hz is valid in terms of calculating the frequency domain response and power.

Along with the frequency of each simulation, the motion amplitude must also be defined. The choice of motion amplitude for each frequency test has to consider any amplitude dependence of the mooring forces. As an example, if the motion amplitude was set unrealistically high the

mooring may be pulled taut, or lead to faster motion bringing non-linear viscous effects. Fitzgerald et al. suggested using the response amplitude operator (RAO) of the floating body to determine representative motion amplitudes [29]. An RAO describes the amplitude and phase of a response and is normalized to a unit magnitude input. The idea of using the RAO reduces the impact of amplitude on the mooring response by keeping the motion amplitude close to what would be experienced in reality. The RAO of the unmoored spar motion shown in Figure 3-6 was generated through BEM modelling by Beatty et al. [40]. This RAO is multiplied by the wave heights corresponding with a representative PM spectrum to estimate the expected motion amplitude for each frequency of wave excitation as shown in Figure 3-7. A lower bound of 0.1 metres is set for the motion amplitude to ensure sufficient excitation of the mooring at the limits of the frequency range considered.

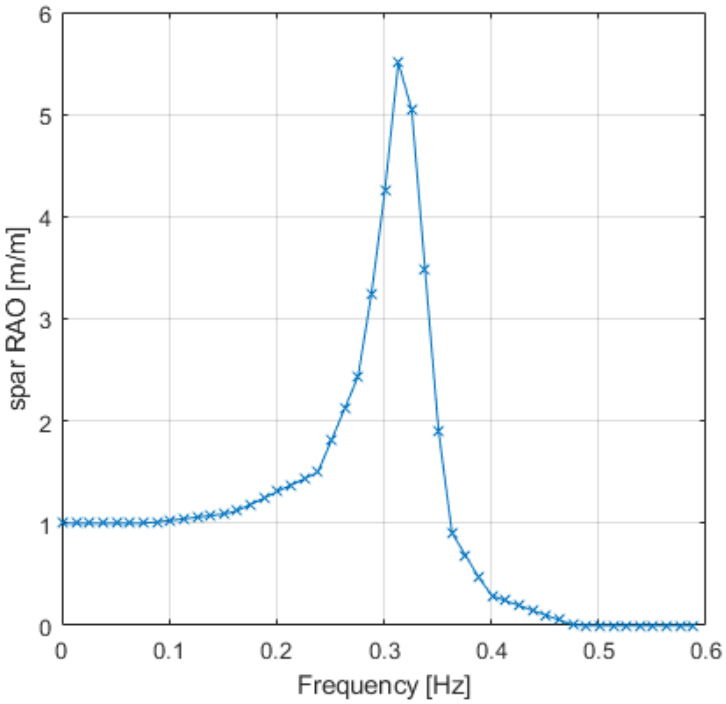

Figure 3-6 Spar RAO reproduced from [40].

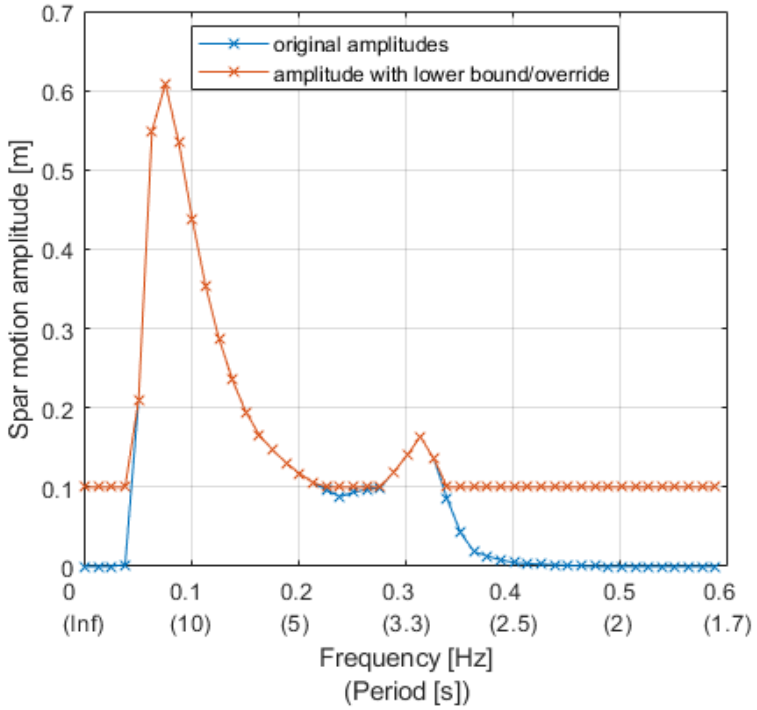

Figure 3-7 Amplitudes of motion used for mooring characterization.

3.6 Characterization of a Single-Block Mooring

The Fourier transform highlights the frequencies at which the mooring responds when excited at a single frequency. The Fast Fourier Transform (FFT) algorithm is used to analyze the frequency content in the mooring force response from Proteus. Windowing is used which smears the data slightly but leads to a more accurate amplitude estimate with the correct considerations. Smearing of the response helps normalize the amplitude response when a discrete sample point does not align perfectly with the excitation frequency as is commonly the case. The frequency content near the excitation frequency in Figure 3-8 (left) is associated with the response and is smeared out due to the windowing. Summing the variance stems and moving them to the excitation frequency extracts the amplitude of the response from the data as shown by accurate recreation of the signal in Figure 3-8 (right). The vertical bars in indicate the upper and lower bounds of the data used for this estimate.

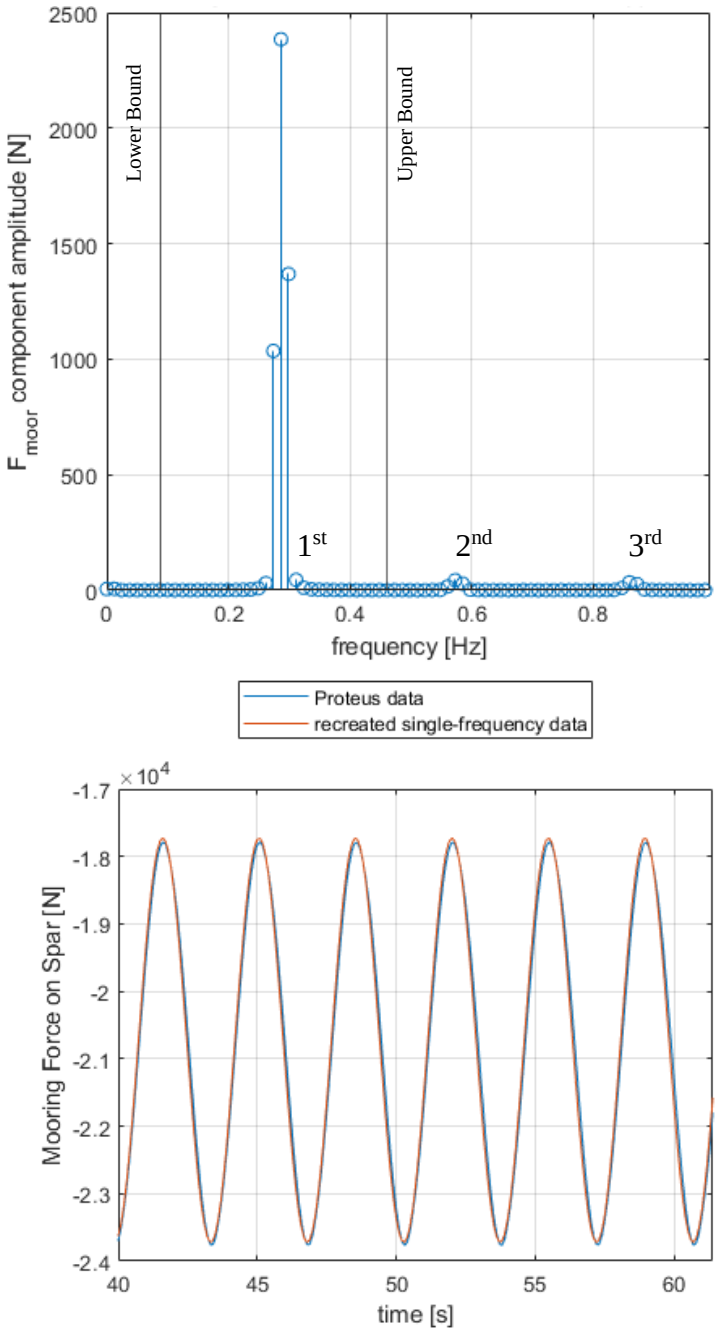

Figure 3-8 FFT of force response with data used to generate fit indicated with vertical bars (top) and example of good linear fit (bottom).

The sample frequency data of the catenary mooring in Figure 3-8 generally shows some response at frequencies other than the excitation frequency which must be rejected in a monochromatic analysis. An excitation at one frequency must correspond with a single impedance,

so any response at frequencies other than the excitation frequency is rejected. Then, just the variance near the excitation frequency is used to recreate the signal. The Fourier transform also provides information on how much the mooring leads or lags the spar velocity from the phase.

When the mooring is sinusoidally excited there is always some steady-state response at other frequencies. These additional peaks can be observed at integer multiples of the excitation frequency or harmonics. If these peaks are small, then there is little to no response at the harmonics, and overlaying the linearized response with the original data shows excellent agreement. If the harmonic responses are a considerable portion of the overall response, then fitting a sine wave to the original signal has poorer agreement as shown for a different excitation frequency of the catenary mooring in Figure 3-9.

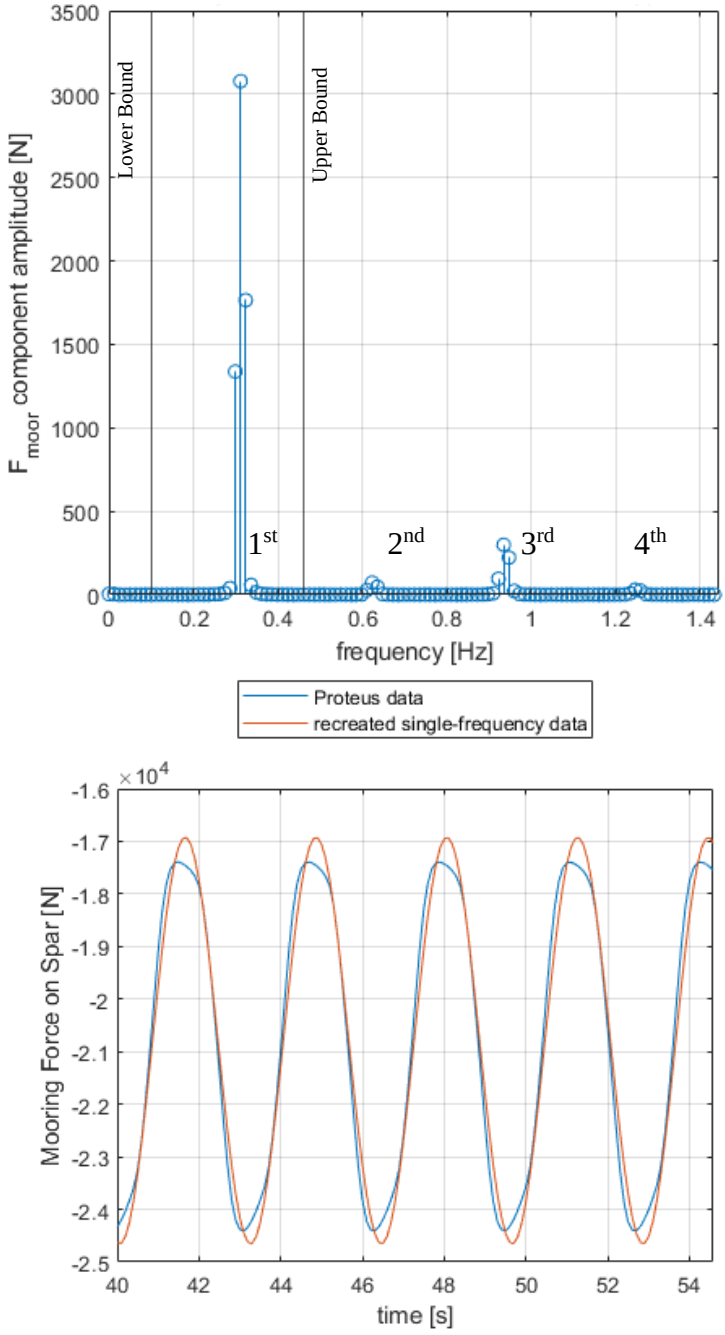

Figure 3-9 FFT of force response with data used to generate fit indicated with vertical bars (top) and example of so-so linear fit (bottom).

The frequency data in Figure 3-9 has a larger frequency content spike at its third harmonic. This additional content stems from reduced peaks of the simulated mooring heave force oscillations. The shape is still periodic and nearly sinusoidal. The difference between the Proteus

data and recreated monochromatic response comes from regular interference by the third harmonic. However, the linear fit in Figure 3-9 is not only less accurate at the peaks and troughs, but the different shapes of the peaks and troughs are not captured. This difference highlights that the external loads driving the mooring motion are not consistent throughout the motion. Varying external loads are likely caused by different forces driving the mooring upwards and downwards. As the spar starts to rise it pulls the mooring taut and line tension suddenly rises. When the spar moves back down it cannot push the cable, rather, gravity returns the cable to its original position more slowly. Figure 3-10 shows this effect with the position of each node of the heavy catenary mooring when the spar is exactly at the middle of an upward or downward motion where its velocity is maximized.

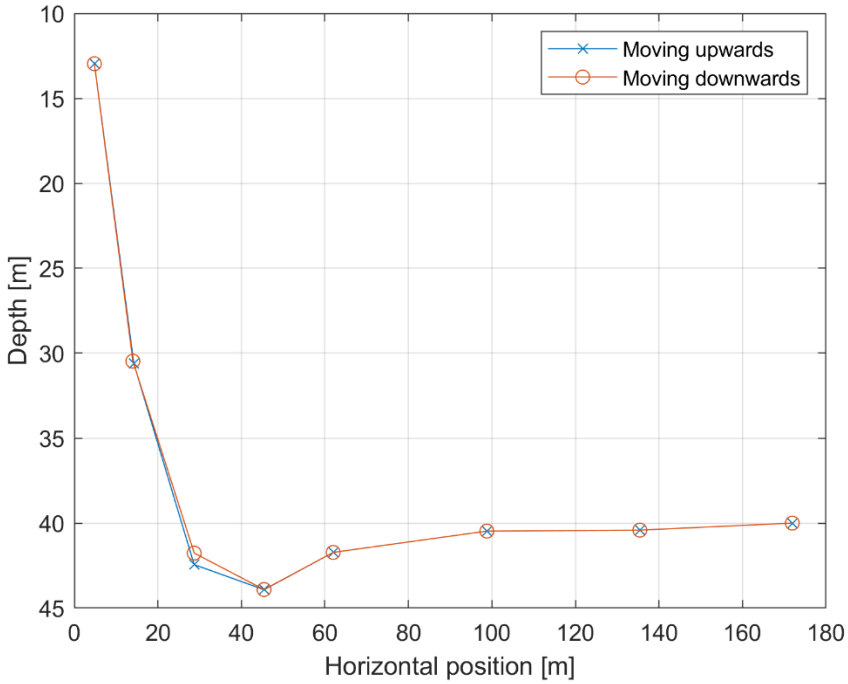

Figure 3-10 Difference in mooring position when mooring is being pulled up or falling due to gravity.

Most of the nodes are in the same position, but the third node on the left differs by 0.5 metres. When the spar is moving up the segment between the second and third nodes is stretched to 10%

of it’s original length as it pulls the mooring line out of the silt and mud in the seabed. During downward motion the mooring sinks into the seabed under its own weight. These interactions at the seabed lead to specific periodic variations in stretch and tension that are distinct for each mooring segment. This, in turn, results in non-sinusoidal oscillation in the heave force at the connection between the mooring and spar.

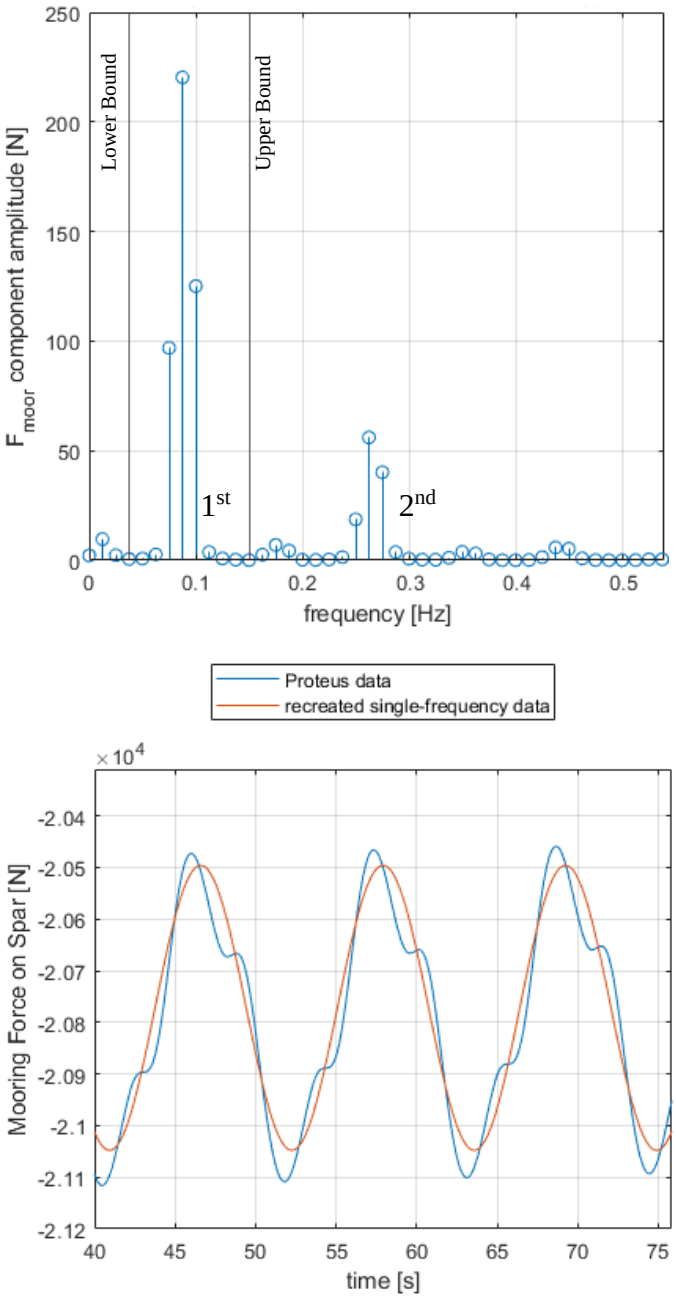

Figure 3-11 FFT of force response with data used to generate fit indicated with vertical bars (top) and example of poor linear fit (bottom).

Figure 3-11 highlights a larger distortion of the of the heave force signal at the mooring-spar connection. The frequency content near 0.27 Hz is a significant portion of the overall response. The single-frequency response still looks reasonable, but some details are lost when the higher frequency content is rejected.

In the worst cases a significant amount of frequency content occurs at frequencies other than the excitation frequency or its harmonics as shown in Figure 3-12. These harmonics tended to be stronger for higher frequencies of the lazy-S mooring which also had a noisy steady-state response. This is thought to be an artifact of regular snap loads caused by the configuration of the lazy-S design and its depressor mass. Regular snap loads would appear in the Fourier transform as strong harmonic responses which are exactly what are observed in Figure 3-12. Some noise is also present in the Fourier transform of Figure 3-12, which is believed to result from the extraneous motion of the depressor mass between snap loads as it oscillates in heave subject to drag forces. In this case, the linear model is a less accurate fit and highlights the limit for which the linear characterization approach is valid.

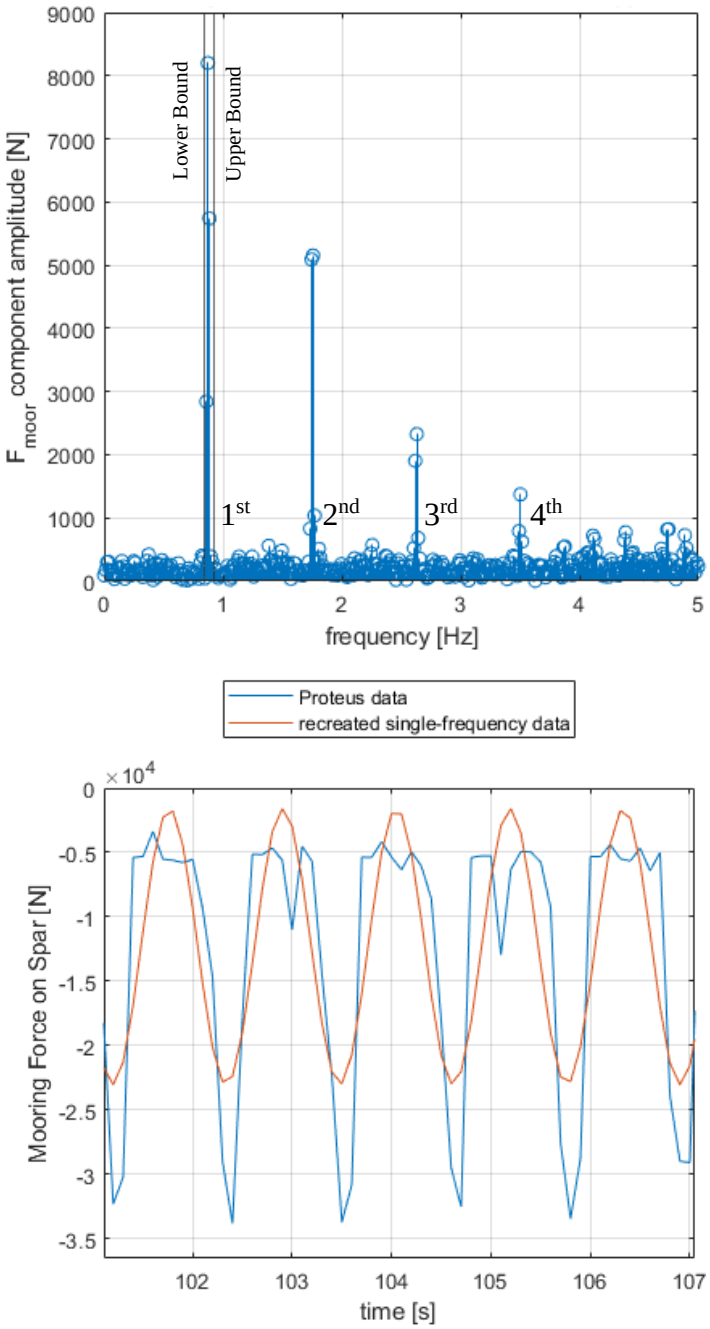

Figure 3-12 FFT of force response with data used to generate fit indicated with vertical bars (top) and example of very poor linear fit (bottom).

A measure of how well the single-frequency linearization matched the simulated response can be made by examining how much frequency content is rejected for each excitation frequency. This measure can be made by computing the percentage of the total variance from the FFT which

is retained by the sinusoidal fit, which helps to inform where the mooring model is most and least accurate as shown in Figure 3-13.

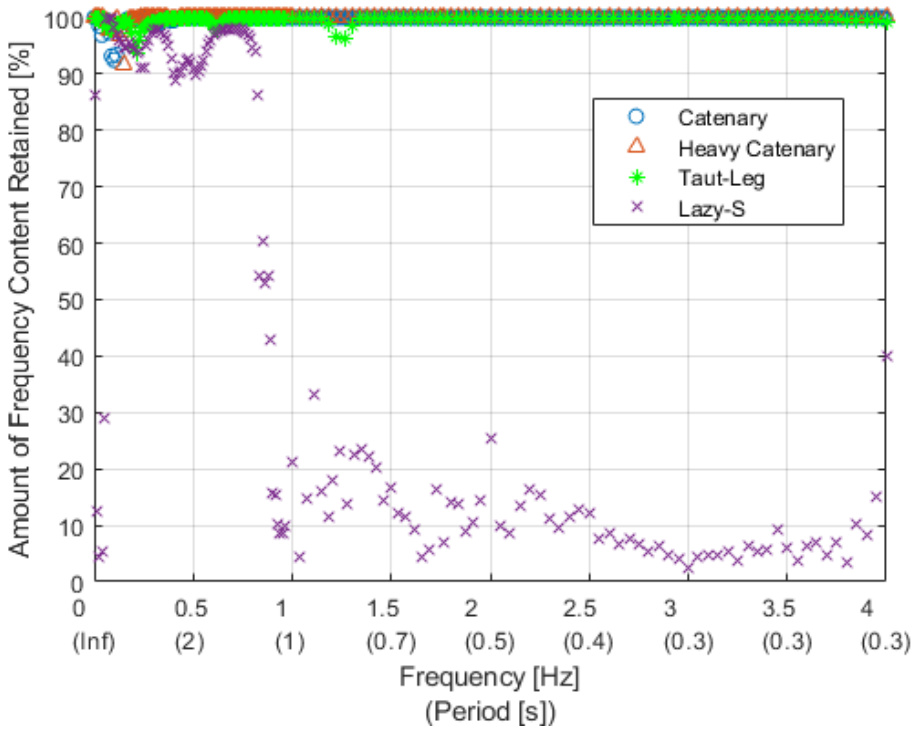

Figure 3-13 Amount of variance retained in the linearization step.

Figure 3-13 shows that the accuracy of the linear models are generally excellent, with over 90% of the frequency content included for all but the lazy-S design. The lazy-S mooring has a poor fit at very low frequencies and frequencies above 0.8 Hz. The low fit percentage likely stems from snap loads that occurred when the depressor mass of the lazy-S design bounced under high frequency excitation. However, the model is still reasonably accurate in the (0.045, 0.13) Hz range where most ocean waves occur at the test site as shown in Figure 3-14.

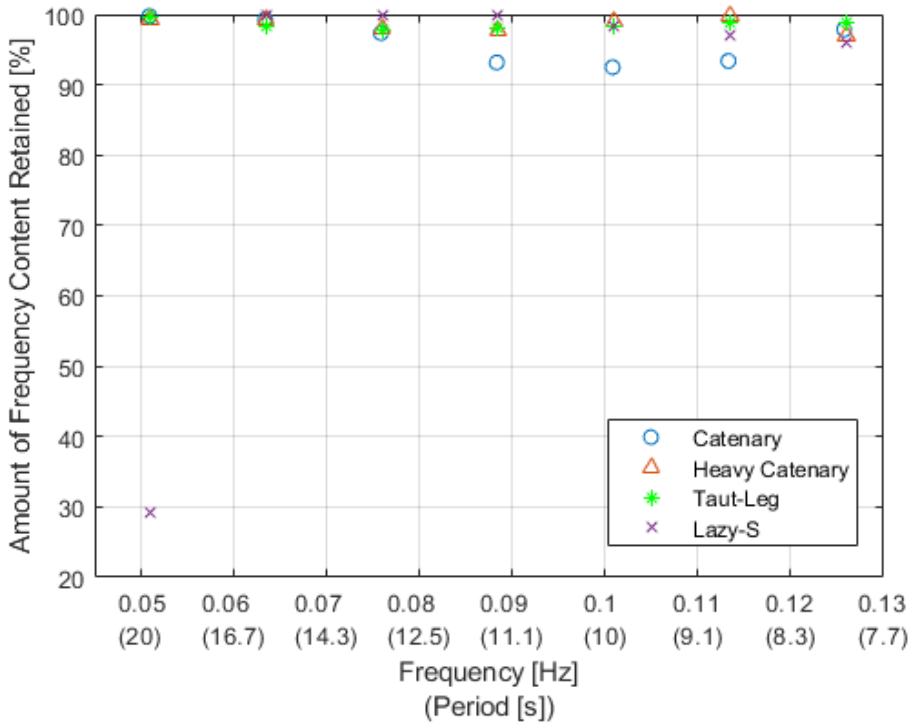

Figure 3-14 Amount of variance retained in linearization step within frequency bounds of interest.

With the motion and force response amplitudes and relative phase known, the next step of the characterization is to determine the impedance of the mooring. Applying equation (3.1) to calculate the impedance amplitude and carrying the relative phase through results in the linear impedance of each mooring as shown in Figure 3-15.

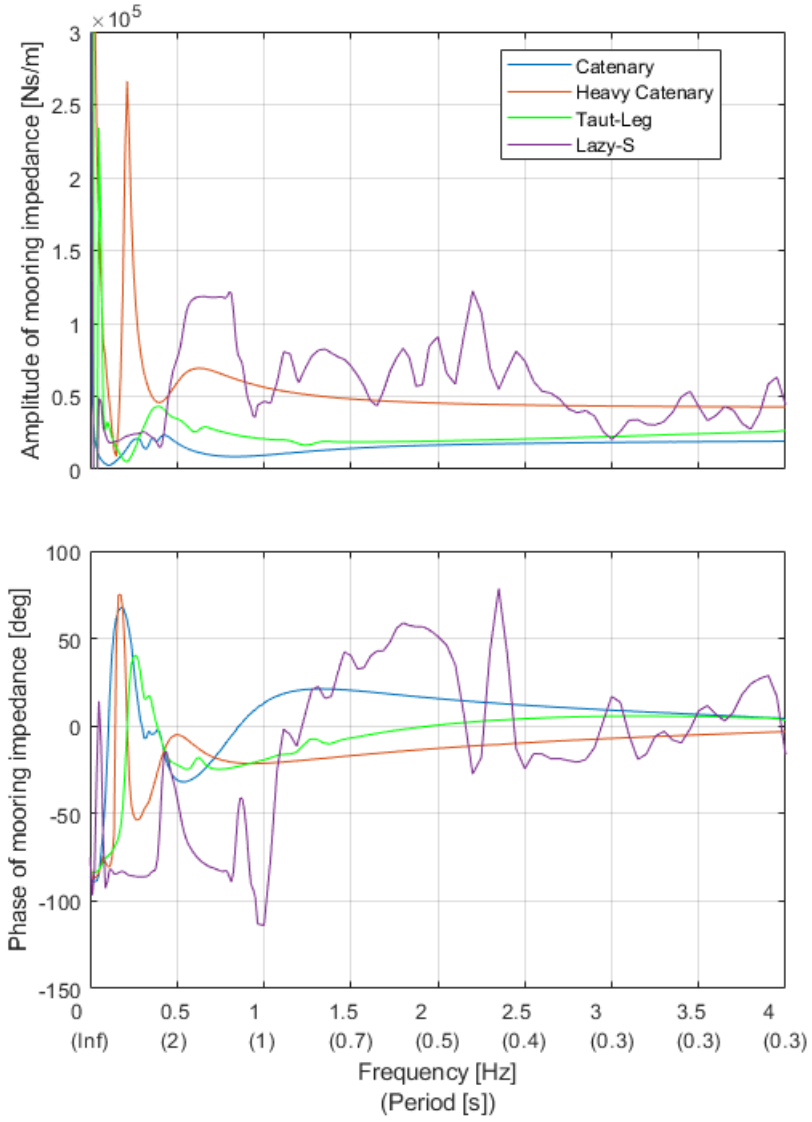

Figure 3-15 Characterized impedance of each mooring.

Characterization is completed up to 4 Hz where most moorings approached a constant impedance, but the impedance of the lazy-S mooring failed to converge due to noisy force responses for some excitation frequencies in the simualtions. The buoyant line used in the lazy-S model tended to oscillate easily due to its low mass and generated the tension spikes previously discussed. Increasing internal damping slightly alleviated these tension spikes, but proved to drastically increase simulation time. Increasing the internal damping by two orders of mangitude

changed the simualtion time ratio from 4:1 to 50:1 and was not sufficient to eliminate the noise in the force response. The lazy-S mooring may be better suited for other characterization methods when the high-frequency response must be understood, but is well behaved in the range studied further in this work, as shown in Figure 3-16.

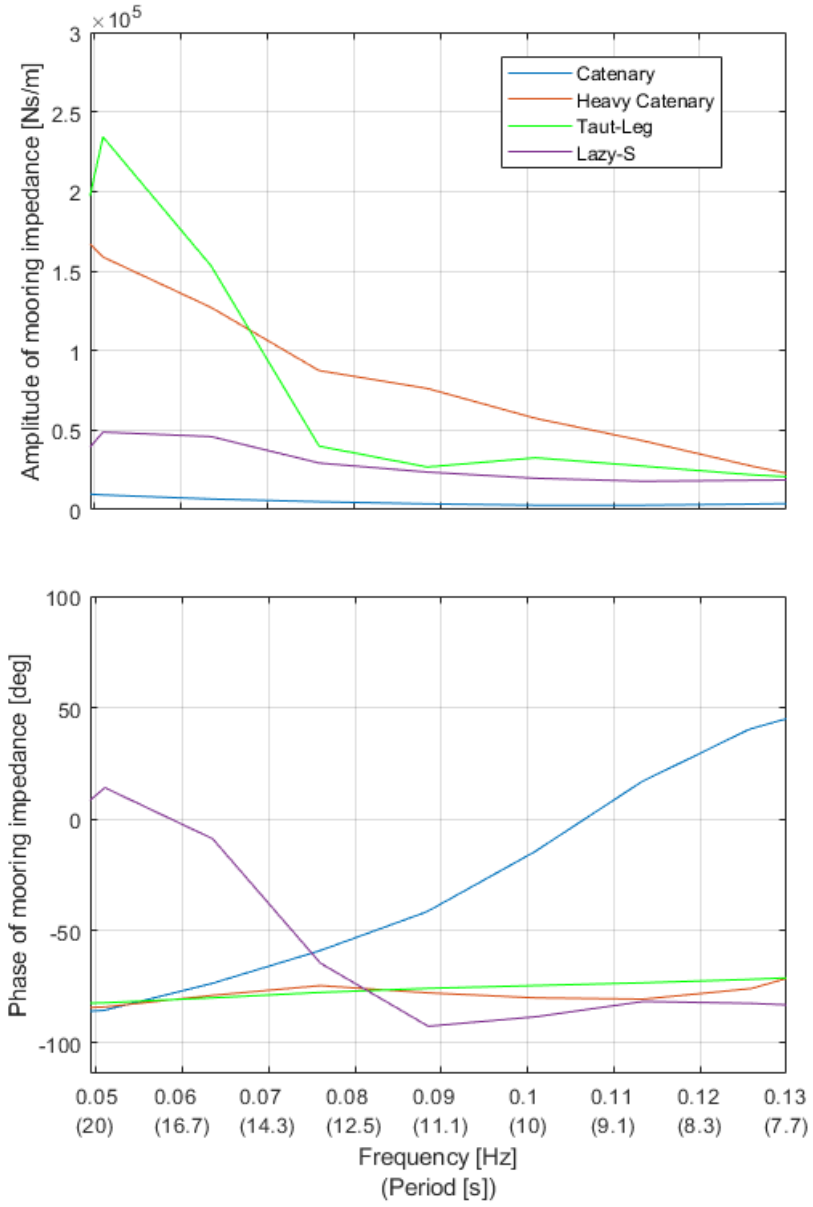

Figure 3-16 Characterized impedance of each mooring in the range where SRPA parameter data is available.

3.7 Multi-Block Mooring Analysis

As previously mentioned, the mooring itself can be represented as a mechanical circuit. This approach yields insight into the mooring which may allow for inferences into how to improve its design for better power capture or control. For example, if a specific phase of the mooring response would somehow benefit the overall system it is not clear which physical parameters should be adjusted to achieve that effect. The parameters available are the choice of assembled components such as type of chain, synthetic line, floats, weights, and equipment; and it may not be obvious which should change or by how much. A multi-block mechanical circuit of a mooring may provide insights to guide that design process. This approach separates the forces acting on the mooring which culminate in tension on the WEC and relates them to the overall impedance as well as providing a point of comparison to the single-block model.

The mooring can be represented as impedances between the nodes representing the force between mooring nodes as well as impedances between the nodes and ground representing added mass, damping, and soil interactions. Forces caused by interaction with the water are included in the connection to ground as well to linearize the system because the amplitudes of fluid motion compared to the cable are considered negligible. Essentially, any force which acts from one mooring node to the next can be expressed in terms of an impedance for that segment and any forces relative to a comparably static frame of reference, such as the water or seabed, are accounted for with an impedance to ground as shown in Figure 3-17. Notably the latter also includes the inertial force felt due to the mass of each node which is always connected to ground. Notably, the multi-block study uses data from the finite-element mooring simulation and is necessarily affected by the choice of number of nodes and segments to discretize the mooring into. The forces relevant

to the multi-block analysis are only computed at the nodes of the discrete mooring which determines the layout of the circuit.

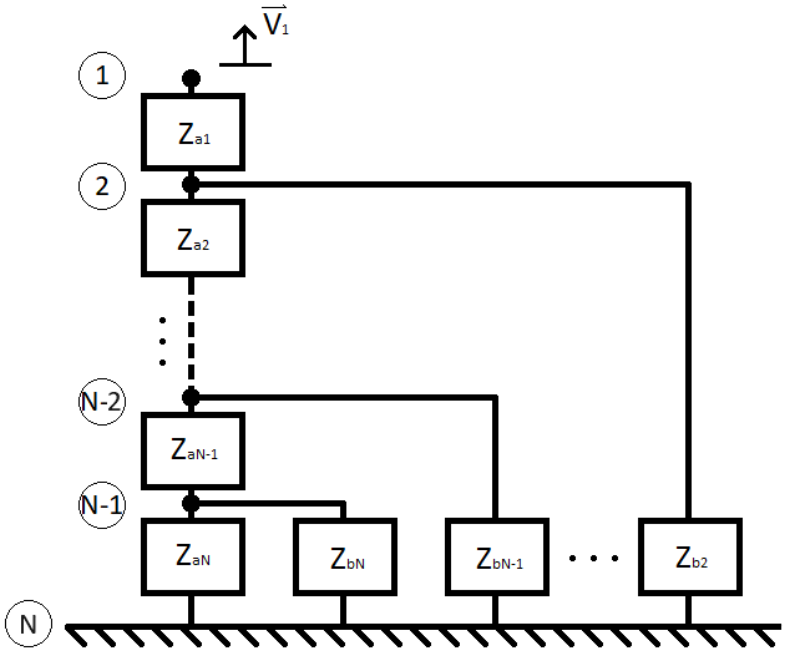

Figure 3-17 Mechanical circuit model of a mooring.

Once each impedance is characterized, this circuit can easily be compressed down to a single impedance by starting from node N and adding the parallel impedances followed by summing the resulting impedance in series with Z_{aN-1} and repeating.

The impedances contributing to Z_{ai} are those which are internal to the mooring. These are the line stiffness k_{ai} and internal damping b_{ai}. The remaining forces are due to the motion of each node in the environment and are given by Z_{bi}; their impedances are node mass m_{bi}, added mass A_{bi}, linearized drag b_{bi}, seabed stiffness k_{bsi}, and seabed damping b_{bsi}. These circuit elements and their simplification are summarized in Figure 3-18.

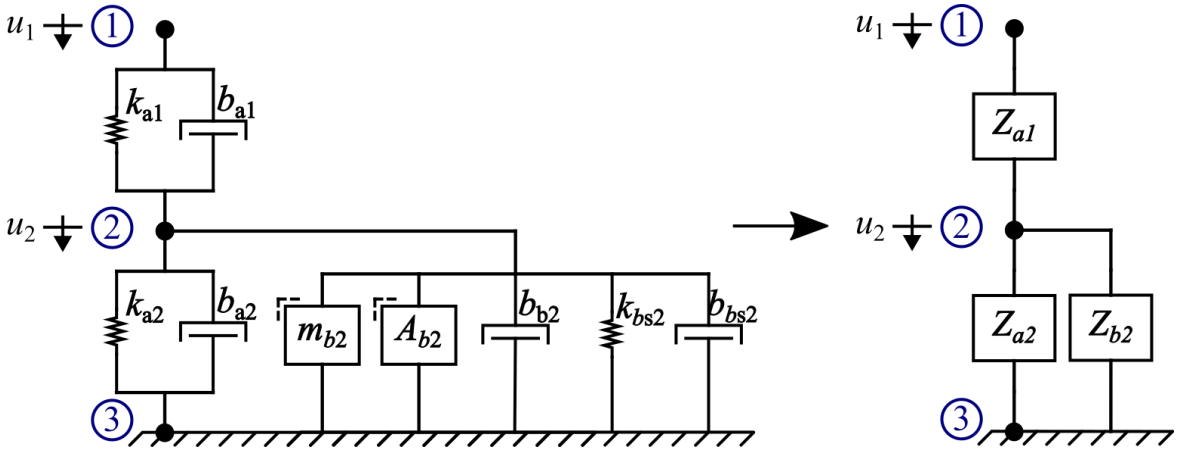

Figure 3-18 Mechanical circuit of a mooring with 3 nodes with all impedances (left), and equivalent impedances (right).

The multi-block approach opens the door to informed design of the mooring system in order to improve SRPA power capture. With an understanding of the forces throughout the mooring and how they fit into the mechanical circuit, a WEC designer may adjust particular parameters of the mooring to move towards a net impedance which may be desirable for the SRPA controller. This concept is only proposed in this work and not studied, but some theories on how a particular circuit element may be affected are presented.

- The viscous damping b_{bi} and added mass A_{bi} terms may be adjusted with changes to the mooring diameter or roughness.
- The internal stiffness k_{ai} and damping b_{ai} could be changed by using different mooring materials.
- The mass m_{bi} can also be changed by introducing weights such as in the case of the heavy catenary design, or by changing materials.

3.7.1 Transfer Function Order of a Simple Mooring

If one considers a simple mooring with three nodes, two of which are kinematically controlled, a simple circuit analysis leads to a suggestion as to the order of the mooring system

transfer function which describes the total impedance of the mooring. The mooring forces of each impedance are described and the circuit simplification process is used to solve for the overall impedance. Applying the circuit methodology from Chapter 2 enables some insight into the order of the system model. In this case it is convenient to use the Laplace domain rather than the frequency domain for simplicity. Switching from frequency to Laplace is realized by substituting $i\omega$ with s for the definitions of the circuit element impedances in Table 1.

$$Z_{ai} = \frac{1}{s} k_{ai} + b_{ai} \tag{3.3}$$

$$Z_{bi} = sm_{bi} + b_{bi} + b_{bsi} + \frac{1}{s} k_{bsi} \tag{3.4}$$

The total impedance resulting from node N, or just node 2 in the analysis of the 3-node case is:

$$Z_N = Z_{aN} + Z_{bN} \tag{3.5}$$

That impedance can then sum in series with Z_{aN-1} and then in parallel with Z_{bN-1} to get Z_{N-1} as shown in Figure 3-19. This procedure can be repeated in general up the mooring circuit with each Z_i being comprised of the force generated by node i and all the nodes below it.

$$Z_i = \frac{Z_{i+1} Z_{ai}}{Z_{i+1} + Z_{ai}} + Z_{bi} \tag{3.6}$$

Note that a special case of equation (3.6) exists for $i = 1$ since there is no Z_{b1}. From here, the impedances can be combined until node 1 is reached and the equivalent impedance $Z_1 = Z_{moor}$ is found.

In the case of the simple two-segment mooring:

$$Z_{moor} = Z_1 = \frac{Z_2 Z_{a1}}{Z_2 + Z_{a1}}, Z_2 = Z_{a2} + Z_{b2} \tag{3.7}$$

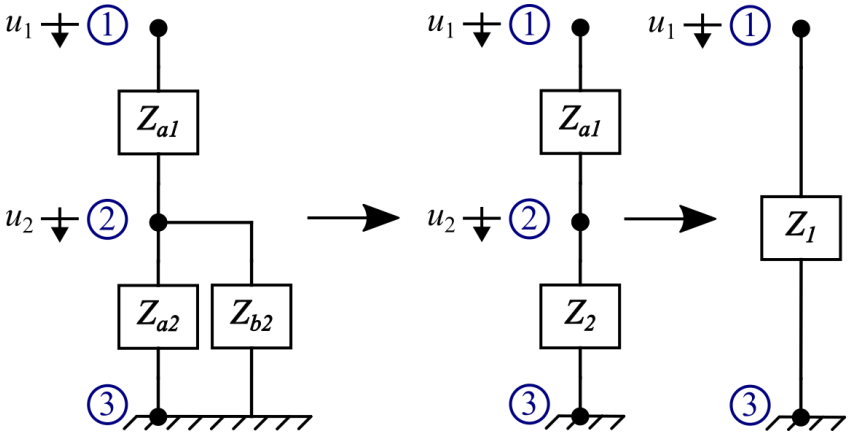

Figure 3-19 Simplification of mechanical circuit of a 3-node mooring by summing impedances in parallel and series.

Substituting in Equations (3.3) and (3.4) for nodes 1 and 2 and grouping terms based on their order results in:

$$Z_1 = \frac{\left[b_{a1}m_{b2}\right]s^3 + \left[b_{a1}C + k_{a1}m_{b2}\right]s^2 + \left[k_{a1}C + b_{a1}k_{a2}\right]s + k_{a1}k_{a2}}{\left[m_{b2}\right]s^3 + \left[b_{a1} + C\right]s^2 + \left[k_{a1} + k_{a2} + k_{bs2}\right]s}, \tag{3.8}$$
$$C = b_{a2} + b_{b2} + b_{bs2}$$

This expression has an order $O\left(s^3\right)$ in both the numerator and denominator. Repeating this process for a 3 segment mooring yields $O\left(s^5\right)$, and again for a 4 segment mooring yields $O\left(s^7\right)$. This pattern suggests that the transfer function order increases by two with each additional segment and the order of the full transfer function follows the expression $O\left(s^{2n-1}\right)$ where n is the number of segments used to discretize the mooring into the finite element model.

3.7.2 Characterization of Multi-Block Mooring

The data for this characterization is found through enabling “verbose mode” in Proteus and extracting the tension in each segment from the “tensions.dat” file and finding the vertical component using the positions of the nodes. The characterization procedure of one segment is then identical to that of the entire mooring but with the velocity of the mooring replaced with the velocity difference between the nodes at each end of the segment for Z_{ai}, and the velocity of node i for Z_{bi}. The Z_{ai} impedances are characterized using the tension force in each segment; and Norton’s node law is used to characterize the Z_{bi} impedances since the force acting through this impedance is simply the difference in tension forces on either side of node i. The procedure of combining impedances is then used to find the equivalent impedance which can be compared with the single-block characterization method.

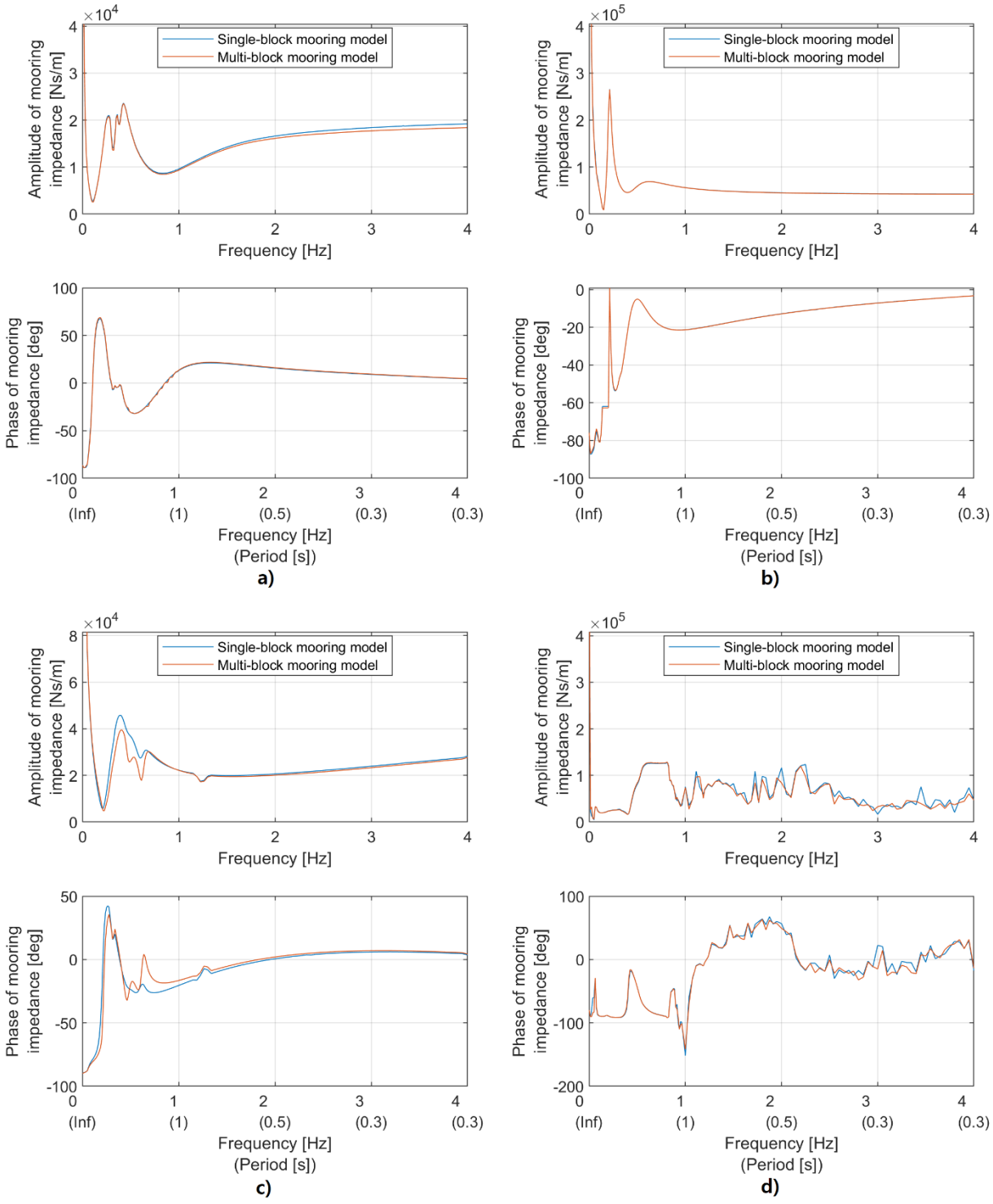

Figure 3-20 Comparison of single-block and multi-block characterization of a) catenary mooring, b) heavy catenary, c) taut-leg mooring, and d) lazy-S mooring.

Figure 3-20 shows that the single and multi-block mooring approaches are in reasonable agreement. Both approaches give nearly identical results for the catenary moorings, while the taut-leg and lazy-S moorings differ slightly, even despite the noise present in the lazy-S response. Two reasons for this could be the accumulation of poor individual impedance characterizations and the heave-only assumption. If one impedance is poorly characterized it may propagate through the process of combining impedances and corrupt the final impedance. Any corruptions are more likely for the multi-block characterization because characterization is only completed for the heave DOF of each node. Any horizontal motions caused by tension are ignored in a single DOF analysis. For example, the nodes of the taut-leg mooring move somewhat horizontally as the line tightens and loosens, and the same is true of the lazy-S mooring, while the long catenary shapes lead to nearly pure vertical motion.

3.8 System Identification

At this point the discrete response could be interpolated to fulfill the frequency domain modelling of the mooring in the circuit model, but it would not be feasible to transform the data to a time domain response function as it is. System Identification (SID) is employed to generate a frequency domain model which fits the frequency domain characterization of the four moorings. The SID process also allows some control over the type and order of the model to be fitted, but does not guarantee a good fit. The models used in this work are transfer function models and state-space models. These are used as they are both linear models which are simple to interpret and interchangeable. All state-space models have an equivalent transfer function model which can be determined mathematically and vice-versa, so, for the sake of simplicity all models will be expressed in transfer function form.

The transfer function model is a ratio of two polynomials, a numerator $N(\omega)$ and a denominator $D(\omega)$.

$$Z_{moor}(\omega) = \frac{N(\omega)}{D(\omega)} \tag{3.9}$$

Two important characteristics to enforce for the transfer functions are that they be both stable and minimum-phase. Stability ensures the system behaves as one would expect of a real system where bounded inputs result in strictly bounded responses. A system is stable if the denominator has only positive zeros as defined by equation (3.10). Minimum-phase means that the SID model responds in the expected direction when excited rather than initially opposite by a phase offset. This condition is held if all *zeros* of the SID model have a negative real component as shown in equation (3.11).

$$Re\left\{Zeros\left\{D(\omega)\right\}\right\} < 0 \tag{3.10}$$

$$Re\left\{Zeros\left\{N(\omega)\right\}\right\} \leq 0 \tag{3.11}$$

When fitting a model, the stability condition is enforced by only allowing positive polynomial coefficients in the denominator [54]. The same condition applies to the numerator to achieve minimum-phase. However, in this case it is necessary, but not sufficient [55], so the pole-plot of each model must be checked for agreement.

System identification is completed using Matlab's System Identification Toolbox which allows the desired conditions to be enforced. The best fit is found through trial and error by incrementing the number of zeros and poles of each transfer function and the order of state-space models up to 18 degrees of freedom. This limit is set above the maximum expected from the multi-

block analysis to allow the opportunity for a good fit. However, it must be noted that a higher order system is less desirable because of its greater complexity. The lowest order transfer function or state-space model to have less than a 1% difference in fit from the previous order is taken as the representative transfer function for each mooring as some may be better suited to a linear fit.

3.8.1 Catenary Mooring

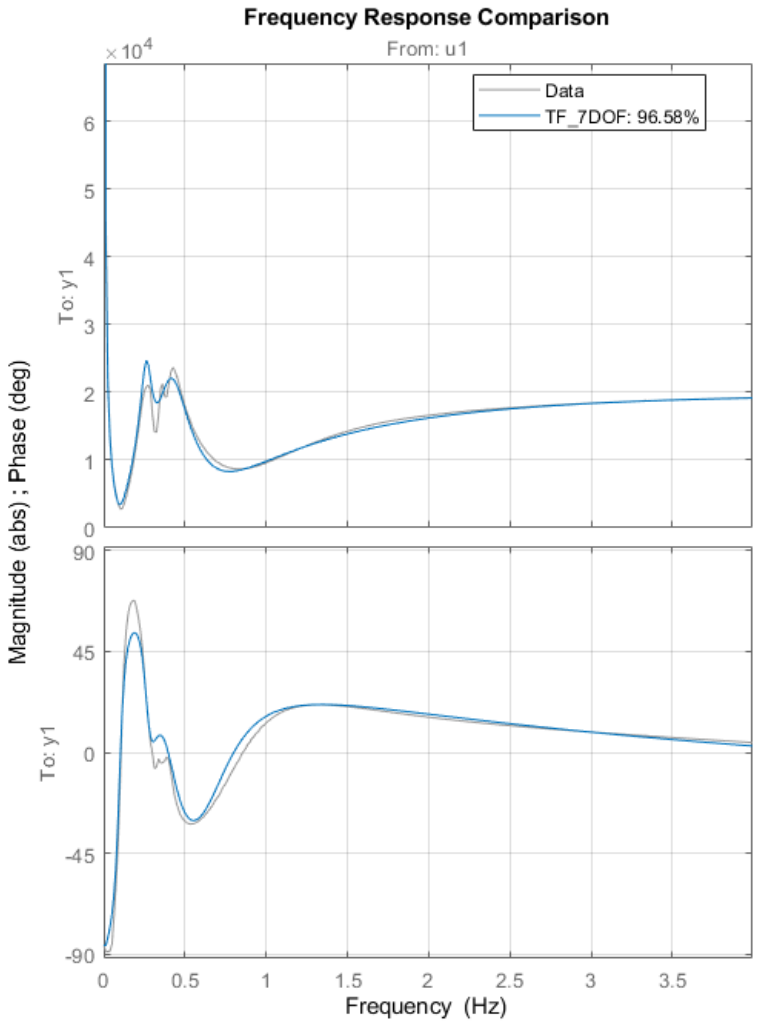

Figure 3-21 SID transfer function fit to characterized catenary mooring.

The best fit for the catenary mooring is a 7 DOF state-space model with a 96.58% match. The fit value is calculated using the normalized root-mean squared error (NRMSE) of the two curves. The expected order of this system stemming from the 7 segments in the multi-block model is $O\left(s^{13}\right)$. However, only 4 segments move substantially in the simulations, so it follows that the remaining segments do not contribute to the system dynamics or the model. Using this heuristic instead leads to a matching $O\left(s^{7}\right)$ and suggests that the last 3 segments could be modelled as a single segment instead. The alignment of node segments to transfer function order appears to be a consequence of using a finite element mooring model, so it may be interesting to characterize a real mooring and compare the resulting order.

3.8.2 Heavy Catenary Mooring

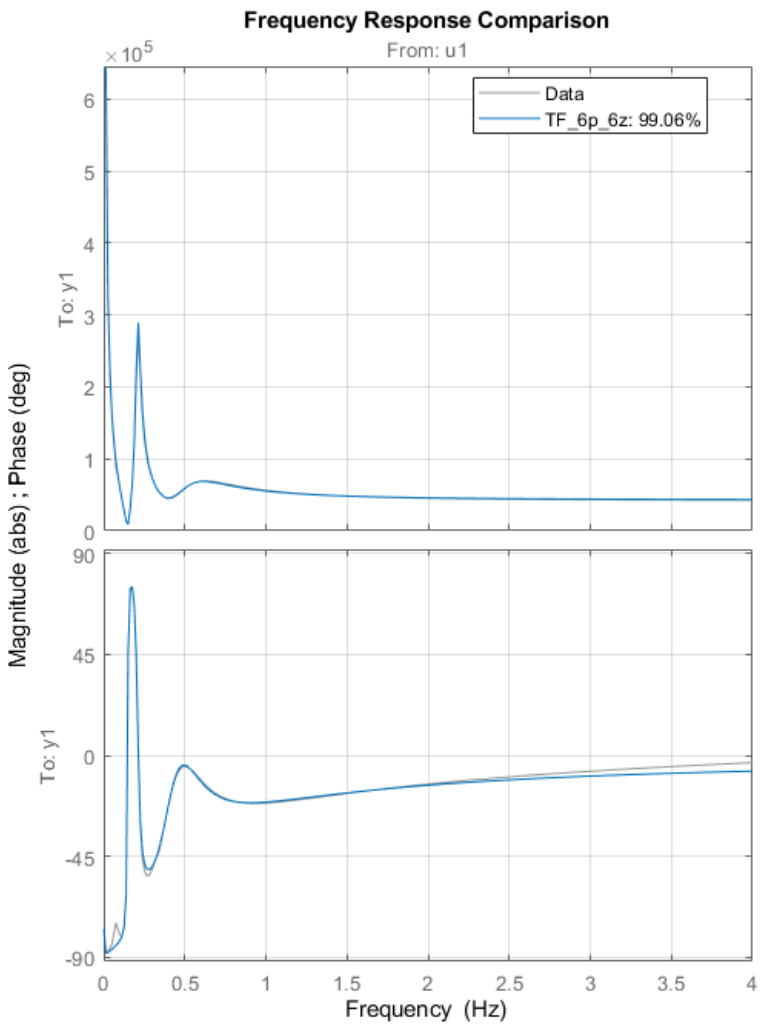

Figure 3-22 SID transfer function fit to characterized heavy catenary mooring.

The best fit for the heavy catenary mooring is a 6 DOF transfer function with 99.06% agreement. The transfer function order nearly aligns with the expectation of an order of $O(s^7)$. A 7 DOF model is also a good fit, but the 6 DOF model is desirable for its lower order. This suggests a pole and zero of the 7 DOF model are close enough to nearly cancel out for this particular

mooring. The pole-zero maps of each transfer function are provided in Appendix C – SID Pole-Zero Plots.

3.8.3 Taut-Leg Mooring

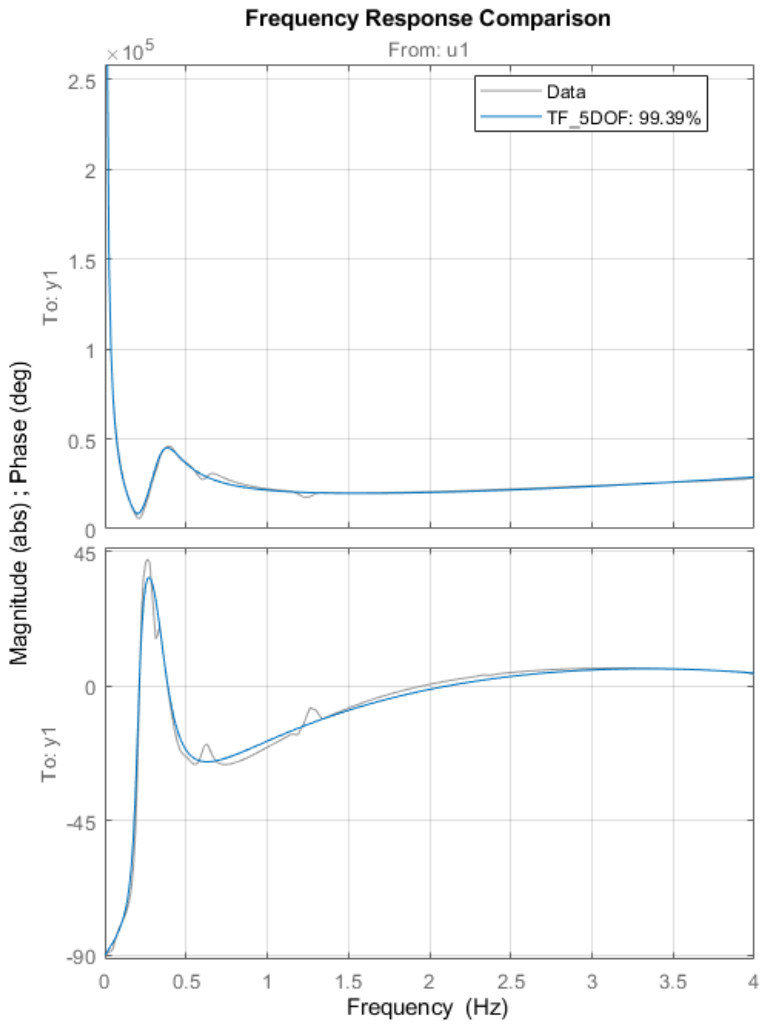

Figure 3-23 SID transfer function fit to characterized taut-leg mooring.

The best fit for the taut-leg mooring is a 5 DOF transfer function with 99.39% agreement. The expectation for this mooring is that it should have an order of $O(s^7)$. Again, this suggests one of the segments modelled is redundant.

3.8.4 Lazy-S Mooring

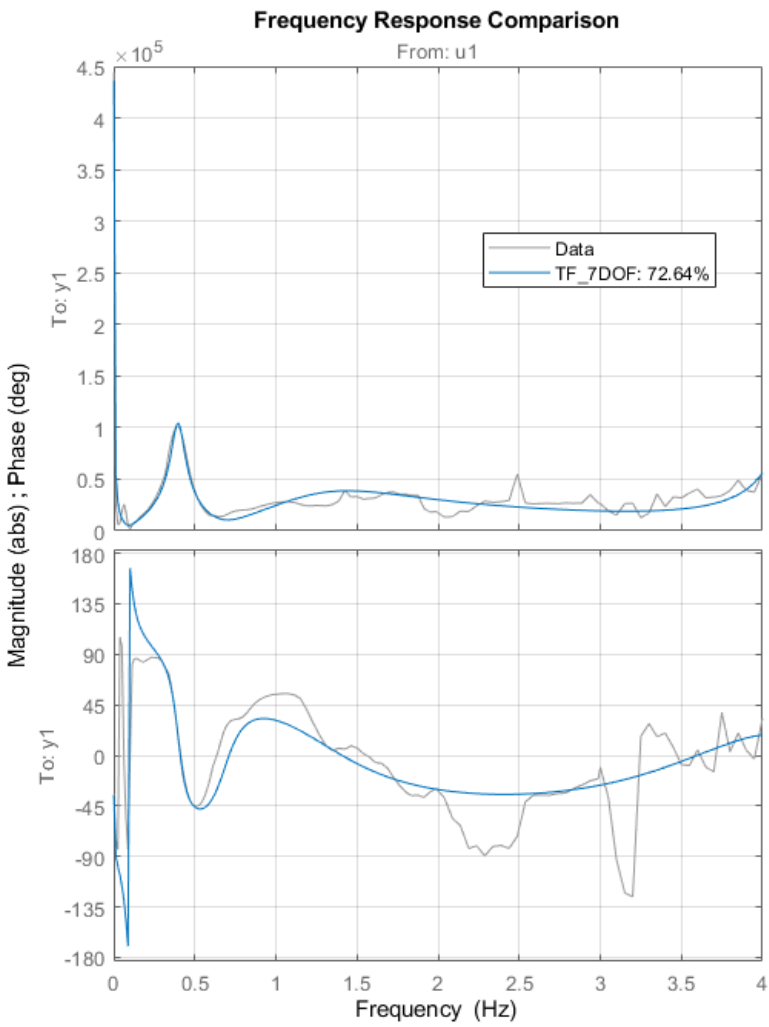

Figure 3-24 SID transfer function fit to characterized lazy-S mooring.

The best fit for the lazy-S mooring is a 7 DOF transfer function with 72.64% agreement. The fit is significantly worse than the previous moorings due to the noise at high frequencies. The SID process is repeated over the frequency range used in the analysis within Chapter 4 in an effort to generate a better fit in that critical region.

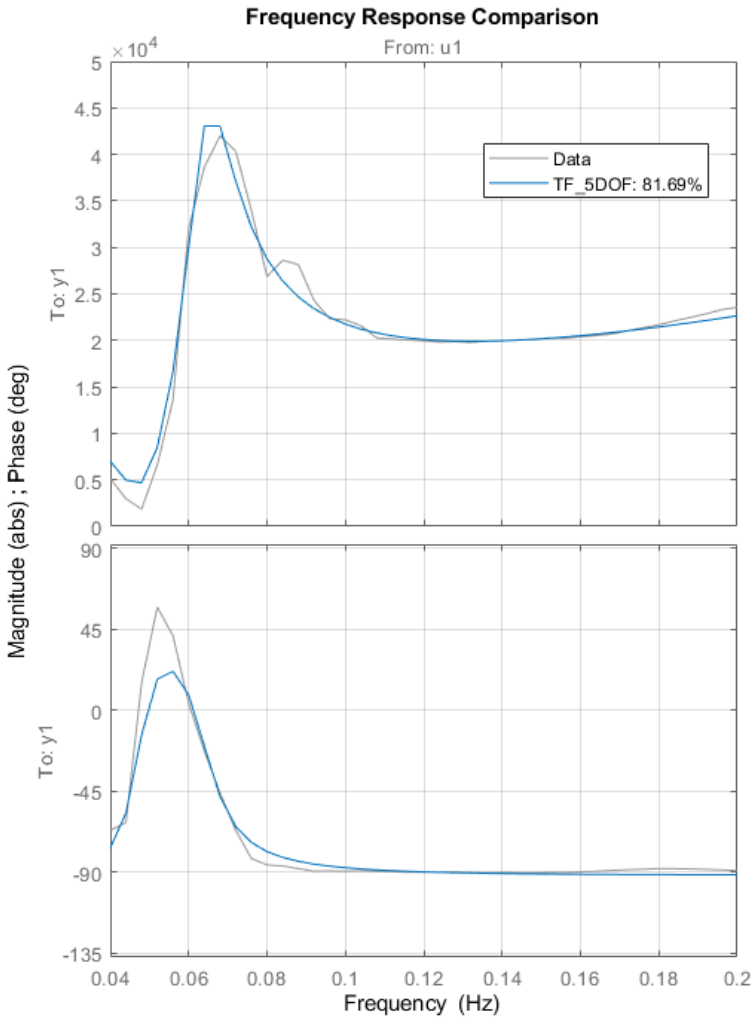

Figure 3-25 SID transfer function fit to characterized lazy-S mooring between 0.04 Hz and 0.2 Hz.

The best fit for the lazy-S mooring in the reduced frequency range is a 5 DOF transfer function with 81.69% agreement. This fit is an improvement from the full frequency range, but not as good as the other mooring designs. The lazy-S design is also the only mooring for which the minimum phase condition could not be met. The noisy response, moderate linear fit, and failure to achieve minimum phase suggest that this mooring is highly non-linear and poorly suited for a

linear analysis. The impacts of this mooring on the power capture and control of the SRPA are still investigated in Chapter 4, but it is considered the upper limit of what is feasible with this approach.

Despite these issues, the order of the transfer function still agrees with the hypothesis that the order of the transfer function aligns with that of the multi-block mechanical circuit. The first two segments of this mooring move the most, while the third moves slightly, suggesting an order of $O\left(s^5\right)$.

Chapter 4

Impact of Moorings on WEC Control

Control of a WEC is an implicit exercise – the WEC operator, whether artificial or human, must attempt to adjust the mechanical impedance of the device to maximize the power transfer into the PTO. In the case of the SRPA, the control exercise is the same as bringing the single body equivalent into resonance. To complete that exercise, the control mechanism must manipulate the intrinsic impedance to this desired result. This is in stark contrast to control systems typical to most mechanical systems where actuators are used to add new forces to the system to achieve the desired motion. In that case, the actuators must overcome the mechanical resistance to motions such as inertia, drag, and friction; which can be assured through proper sizing of those actuators. In the case of SRPAs, it is infeasible to use external actuators to introduce new forces – rather, the designer must manipulate reaction forces by augmenting the impedances of internal systems such as the PTO and reactive force source. This task requires detailed knowledge of the SRPA systems to inform on the intrinsic impedance.

Previous research on WECs suggests implementing a control scheme is also necessary to achieve the power gains required to be cost-competitive with other renewable energy technologies. Bubbar et al. demonstrates the potential performance improvements available through new mathematical approaches to SRPA control including optimization of the device geometry [13]. It is worth stating that this approach differs from optimization through iteration of the shape of a WEC as demonstrated by Gilloteaux and Ringwood [56]. While the latter iterates on the shape

parameters, and consequently the intrinsic impedance of the WEC to maximize power, the former applies a mathematical formulation to maximize power through internal modification of the intrinsic impedance. Additionally, as mentioned in Chapter 1, Weber suggests that the best approach to designing a WEC is to maximize its performance early on when design alterations are still feasible and inexpensive [20]. The mathematical formulation of optimal control and maximizing performance in early design both suggest the need for detailed and accurate models of WECs. Such a detailed model would necessarily include the mooring system but is generally not included in early-stage control formulations. With an approach for characterizing a mooring to be included in this model, the impact a mooring system has on the SRPA performance and controllers may be determined.

4.1 Control Types

Having characterized a mooring as a frequency-dependent complex impedance, the equivalent single body point absorber can be found as described in section 2.6 that includes the mechanics of the spar, float and mooring. Given that equivalent canonical representation, ideal SBPA control can be implemented inclusive of the mooring. In this work, the sensitivity of the control performance to the mooring impedance is quantified by comparing system performance between cases where the mooring impedance is included and not included in the control implementation.

4.1.1 Amplitude Control

Three types of control are examined with varying complexity. The first is amplitude (AM) control, given in equation (4.1) [38].

$$Z_{PTO} = R_{PTO} = \left|Z_i\right| \tag{4.1}$$

This is the optimal control type if the PTO is limited to being comprised of real or resistive elements, and is one of the simplest types of control. The drawback is that the controller is unable to bring the point absorber into resonance with the waves and so power capture is significantly reduced.

A resonant condition exists if the excitation force and body velocity are in phase, which cannot be achieved if the net impedance of the WEC and PTO has an imaginary component. This condition can be demonstrated with equation (2.46) restated here for convenience:

$$u_{Th} = \frac{F_{Th}}{Z_i + Z_{PTO}} \tag{4.2}$$

Taking the phase of F_{Th} to be the reference, with $\mathrm{Im}\{F_{Th}\} = 0$, if the denominator of equation (4.2) has an imaginary component, then the velocity will also have an imaginary component which is realized as a phase shift from the reference F_{Th}. This imaginary component can be accounted for by adding counteracting imaginary elements to the PTO which are designed such that they cancel the imaginary part of the intrinsic impedance of the SRPA so that the imaginary part of the denominator of equation (4.2) is always zero. This idea comprises the next type of control referred to as complex-conjugate control.

4.1.2 Complex-Conjugate Control

Complex-conjugate (CC) control is the logical evolution of amplitude control and serves to bring the point absorber into a resonant state which produces more energy. As suggested by its name, complex-conjugate control is enacted when the PTO impedance is set to the complex-conjugate of the intrinsic impedance as shown in equation (4.3). The complex-conjugate is an operator denoted with a star which swaps the sign of only the imaginary part of a complex number.

$$Z_{PTO} = Z_i^* = \mathrm{Re}\{Z_i\} - i\,\mathrm{Im}\{Z_i\} \tag{4.3}$$

The CC control type maximizes power capture with the given hull geometry and subsequent intrinsic impedance. That CC control acts on the existing geometry provides some distinction from the following control type and hints as to why CC control is not necessarily the optimal type of control overall.

4.1.3 Geometry plus Amplitude Control

The final type of control explored in this thesis is geometry plus amplitude (GA) control. As discussed by Bubbar et al. this control type achieves improved performance by modifying the system architecture with geometry control and maximizing power with amplitude control [13]. This control type brings the imaginary part of the SRPA intrinsic impedance to zero with an additional controller which connects the spar to ground. By eliminating the imaginary component of the SRPA impedance in advance, when amplitude control is enacted, the velocity is already in phase with the excitation force.

$$\mathrm{Im}\{Z_i\} = 0 \tag{4.4}$$

Bubbar et al. uses equations (2.43) and (4.4) to solve for the optimal spar reactance $X_{eq2_{opt}}$ which has two solutions [13]. The two solutions stem from the choice of whether the positive or negative root of the discriminant is used when solving the quadratic equation.

$$X_{eq2_{opt}} = \frac{-\left(R_{eq1}^2 + X_{eq1}^2\right) \pm \sqrt{\left(R_{eq1}^2 + X_{eq1}^2\right)^2 - 4\left(X_{eq1}\right)\left(R_{eq2}^2 X_{eq1}\right)}}{2X_{eq1}} \tag{4.5}$$

The negative root proved to lead to an operating mode which produced less power in the work of Bubbar et al. [13]. This solution corresponds to another resonant mode, which for the case

of this SRPA architecture, produces less power. This result was independently verified in this research, so the negative solution is neglected going forward and only the positive solution is used. By solving for the optimal spar reactance in this way the intrinsic impedance is constrained to have an imaginary component of zero, effectively bringing the SRPA into phase with the excitation force of the waves.

The optimal spar reactance $X_{eq2_{opt}}$ represents part of the geometry of the SRPA. Spars with different shapes and sizes may have drastically different reactances which vary with frequency. It is unfeasible to design a hull geometry that would align with the optimal spar reactance across a wide range of frequencies, so there is a need to be able to modify or control the spar geometry. Control of the spar geometry could be achieved by adjusting its physical parameters such as its mass as studied by Wang and Ringwood [25]. Bubbar et al. proposes the inerter space as another tool for modifying the spar geometry without the need to add or remove ballast from the SRPA [13]. The reactive force source achieves this effect with an inerter. The inerter generates a force proportional to acceleration, suggesting that the inerter has some *effective mass*. Importantly, this effective mass can be controlled with dynamic weights on the flywheel or by utilizing a variable ratio gear system and can achieve the desired spar reactance at all frequencies.

The reactance required by the reactive force source is computed by Bubbar et al. by extracting the imaginary parts of equation (2.39) to solve for X_{FS} [13]. In this work the imaginary part of the mooring impedance is also included in this calculation:

$$X_{FS}(\omega) = X_{eq2_{opt}}(\omega) - \omega\left(m_2 + A_2(\omega)\right) - \frac{1}{\omega}k_2 - \mathrm{Im}\left\{Z_{moor}(\omega)\right\} \tag{4.6}$$

Equation (4.6) defines the geometry control law which, when coupled with amplitude control becomes a form of master-follower control.

4.2 Velocity and Force Response

Bubbar et al. presented the velocity, force, and power response of a theoretical SRPA operating under the three previously discussed control types [13]. Matching that previous work, these responses are calculated from known parameters using the circuit approach by:

1. Solving for the Thevenin equivalent excitation force using equation (2.42) (repeated in Chapter 4 as equation (4.7) for convenience)
2. Solving for the velocity of the Thevenin equivalent circuit using equation (2.46) (repeated in Chapter 4 as equation (4.2) for convenience)
3. Finally, the average useful power extracted by the PTO as derived by Falnes [35], is computed with the real part of the PTO impedance and Thevenin equivalent velocity amplitude in equation (4.8).

$$F_{Th}(\omega) = \frac{F_{ex1}(\omega) Z_{eq2}(\omega) - F_{ex2}(\omega) Z_{eq1}(\omega)}{Z_{eq1}(\omega) + Z_{eq2}(\omega)} \tag{4.7}$$

$$P_{RAO} = \frac{1}{2} Re\{Z_{PTO}\} u_{Th}^2 \tag{4.8}$$

The results of Bubbar et al. [13], are hereafter reproduced with these expressions to highlight the difference each control type has on these responses to inform on the influence of the mooring.

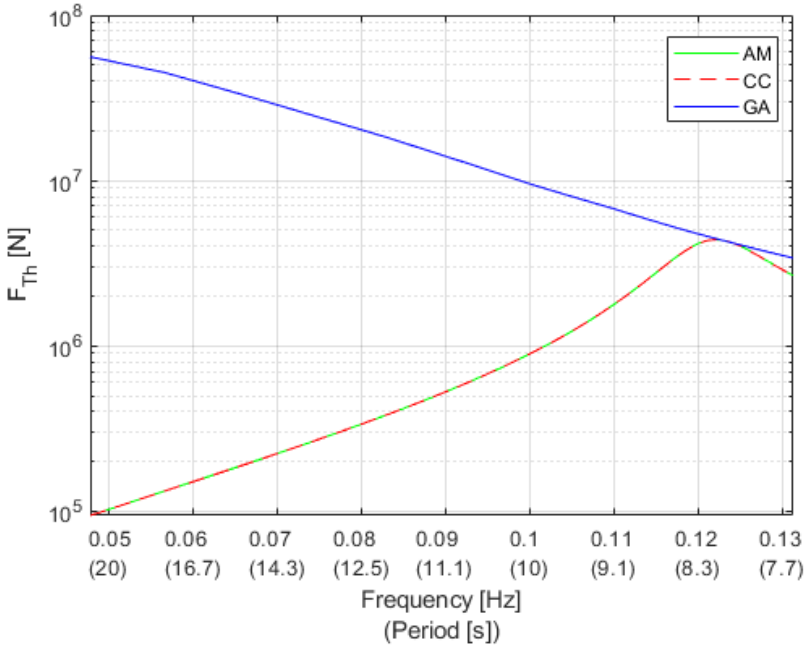

Figure 4-1 Thevenin equivalent excitation force generated by SRPA operating with three control types.

Figure 4-1shows the Thevenin excitation force is much higher for GA control. Notably, these forces are all upper limits of what is achievable for each control type and real-world effects such as viscous drag would lower the bounds of these force responses. It also highlights the point in AM and CC control where the intrinsic impedance of the Thevenin equivalent SBPA naturally has an imaginary component equal to zero and aligns with the principle of GA control. The point where they meet indicates the frequency the SRPA is tuned to, or where it is in natural resonance with the waves. Here, GA control demonstrates the upper bound which may be achieved by tuning an SRPA to a given frequency by changing design parameters beyond the PTO such as body diameter and mass. Additionally, the Thevenin equivalent excitation under AM and CC control are identical because the SRPA parameters are the same except for the PTO impedance which is not present in equation (4.7).

It is worth reiterating that all of these responses are generated using inputs described as excitation force per metre of wave amplitude, with amplitude being half of the observed wave height. Using these input parameters means that these responses all scale linearly with the amplitude of the ocean waves which may reach half a dozen or so metres in extreme conditions.

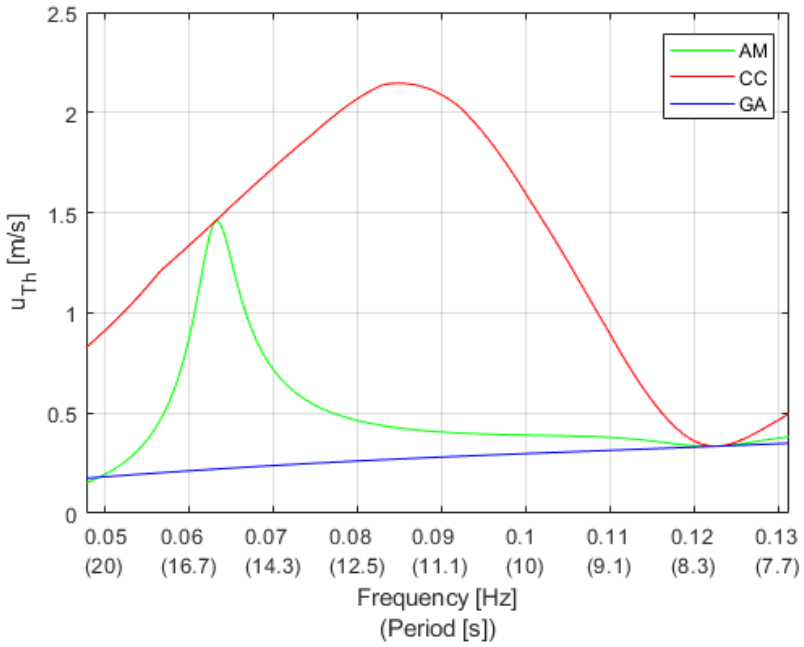

Figure 4-2 Thevenin equivalent velocity of SRPA operating under three control types.

Figure 4-2 shows the same point where AM, CC, and GA control converge around 0.123 Hz, but also highlight a second point where AM and CC control converge around 0.063 Hz indicating that the PTO under CC control is purely real at this frequency and again that the intrinsic impedance is zero at this frequency. This trend differs from GA control because this point aligns with the other solution discussed in section 4.1.3 which also places the SRPA into resonance with the waves, but with a less energetic mode. The interested reader is directed to [13] for more detail on this second mode referred to as “config 4” in that work.

Another important aspect of the velocity amplitude plot is that it provides some indication of the amount of relative travel will occur for this device. Transforming the velocity amplitude to position amplitude is as simple as dividing by angular frequency as shown in the previous discussion of circuits.

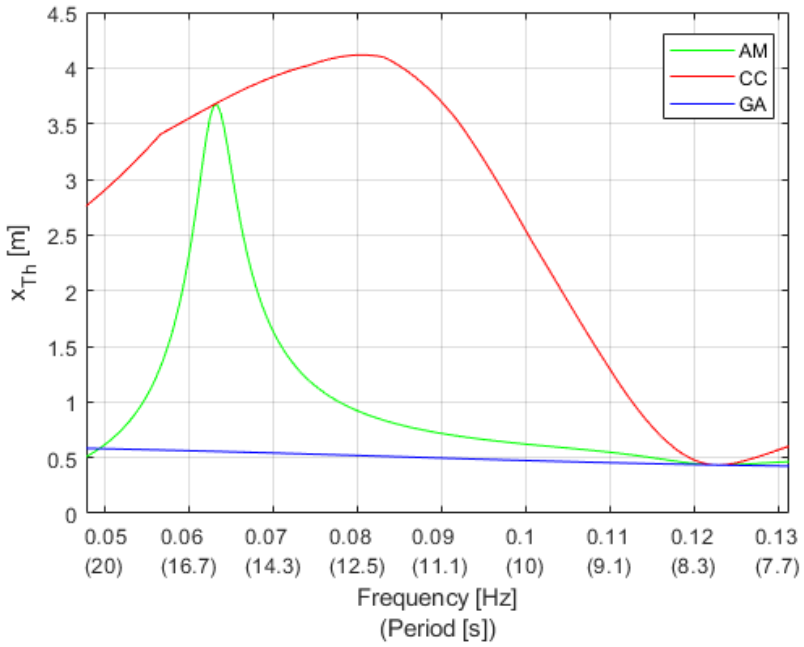

Figure 4-3 Thevenin equivalent position of SRPA operating under three control types.

Figure 4-3 demonstrates the first obvious advantage of GA control with its very low position amplitude response. The Thevenin equivalent position response is equal to the relative position of the float and spar, and thus is also a measure of the travel which must be allowed for the SRPA to operate without hitting end stops. Highlighting here again that the response is *per metre wave amplitude* one may surmise that the SRPA operating under AM or CC control cannot be designed to travel to their full extent without hitting end stops which would significantly curtail their motion and power output since larger waves also contain more power.

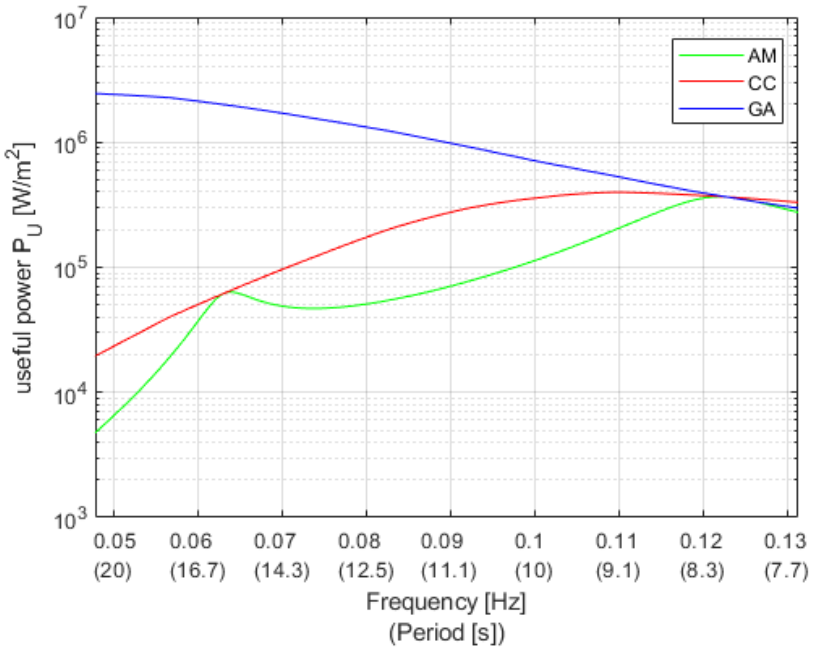

Figure 4-4 Power response of SRPA operating under three control types.

Finally, Figure 4-4 shows the useful power resulting from each control type on a logarithmic scale and demonstrates the magnitude of the improvement achieved for this SRPA when operating under GA control at mid to low frequencies. This performance gain is physically achieved by a change in the resonant mode of the SRPA brought about by the reactive force source. It is important to note that these curves should be understood to be upper bounds on the power due to the real-world effects not included in the model. Notably, CC control produces slightly more power above 0.123 Hz. It happened to be that the second solution for GA control produced two orders of magnitude less power on average despite also being a resonant condition, and the same occurs here for CC control. Note that AM control never produces more power than CC or GA at any point since it nearly never achieves resonance. This highlights that all resonant modes are not equal and should be compared for each WEC architecture, as well as when any changes are made to a WEC architecture such as iterating mooring designs.

4.3 Mooring Influence

Three cases are used to determine what effect the mooring has on both the control and average power.

Case 1 (C1) is a baseline performance calculated with no mooring present; this case matches the scenarios considered in the results of [13].

Case 2 (C2) adds the mooring models to the simulation of the system dynamics, but knowledge of the mooring impedance *is not included* when designing the controller.

Case 3 (C3) applies the optimal control design with the mooring, meaning that the mooring is included in the calculation of the optimal controller parameters.

Any differences in calculated performance of the point absorber between C1 and C2 indicates the amount of power which is added or lost with the addition of the mooring and no compensation for the dynamic footprint of the mooring on the system. Comparison of C1 and C3 results reveal the minimum performance impacts of each mooring.

The expressions used in the frequency domain simulation of each case stem from equations (2.43) and (2.45) which define the intrinsic impedance, or dynamics, of the single-body equivalent WEC. The other parameter affecting the system response is the control input from the PTO and reactive force source which are governed by equation (4.1) for AM control; equation (4.3) for CC control; and equation (4.6), then equation (4.1) for GA control. The cases where Z_{moor} are and are not included are highlighted in Table 5 using CC control for demonstration, with the same principles applied to the expressions for AM and GA control in the studies of those types of control.

Since the mooring is not present in C1, the expression for the intrinsic impedance does not include Z_m, while it is included in C2 and C3. The expressions for Z_{PTO} are similarly set, with Z_m only included in C3. Applying these restrictions leads to the expressions governing the dynamics and control in each case, which are given in Table 5 below.

Table 5 Expressions governing the dynamics and control of the three test cases.

	Dynamics	Control
Case 1	$Z_i = \frac{Z_{eq1} Z'_{eq2}}{Z_{eq1} + Z'_{eq2}}$	$Z_{PTO} = \left[\frac{Z_{eq1} Z'_{eq2}}{Z_{eq1} + Z'_{eq2}}\right]^*$
Case 2	$Z_i = \frac{Z_{eq1}(Z'_{eq2} + Z_m)}{Z_{eq1} + Z'_{eq2} + Z_m}$	$Z_{PTO} = \left[\frac{Z_{eq1} Z'_{eq2}}{Z_{eq1} + Z'_{eq2}}\right]^*$
Case 3	$Z_i = \frac{Z_{eq1}(Z'_{eq2} + Z_m)}{Z_{eq1} + Z'_{eq2} + Z_m}$	$Z_{PTO} = \left[\frac{Z_{eq1}(Z'_{eq2} + Z_m)}{Z_{eq1} + Z'_{eq2} + Z_m}\right]^*$

4.3.1 Solution Procedure

Each case is simulated by loading the parameters from Table 3 and Figure 2-9 into a programming environment and solving the system of equations. The solutions are computed monochromatically and discretely in the frequency range defined by the bounds of the SRPA data used, from 0.045 Hz to 0.13 Hz.

First the intrinsic impedance is found using equation (2.43) with (C2 and C3) or without (C1) the mooring impedance. Next the control parameters for each type of control are computed using equation (4.1) for AM control, equation (4.3) for CC control, and equations (4.5) and (4.6) for GA control. As shown in Table 5, C2 uses the mooring impedance in the dynamics, but not the

controller calculation. Finally, the excitation force, velocity response, and useful power are calculated using equations (4.2), (4.7), and (4.8) as discussed in section 4.2. Worth noting is that these responses are all complex amplitudes with oscillations occurring at different phases and amplitudes but at a single frequency – that of the incident wave considered. This is naturally the case as the frequency domain solutions are, by definition, steady-state; and a system with forced oscillations can only oscillate at the frequency of that forcing when at steady-state.

The useful power leaving the SRPA through the PTO is calculated by taking the real part of the PTO impedance. Then, the average power across a resistive circuit element with a sinusoidal excitation is half of the amplitude as per circuit theory.

4.3.2 Frequency Domain Simulation Power Results

The resulting power from the simulations are organized to exhibit the effect of each mooring on each of the three types of control. Note that the frequency range has been reduced to (0.045, 0.13) Hz due to limitations in the data available for the SRPA. As discussed, this range is still insightful as it contains much of the wave energy on the West Coast of Canada.

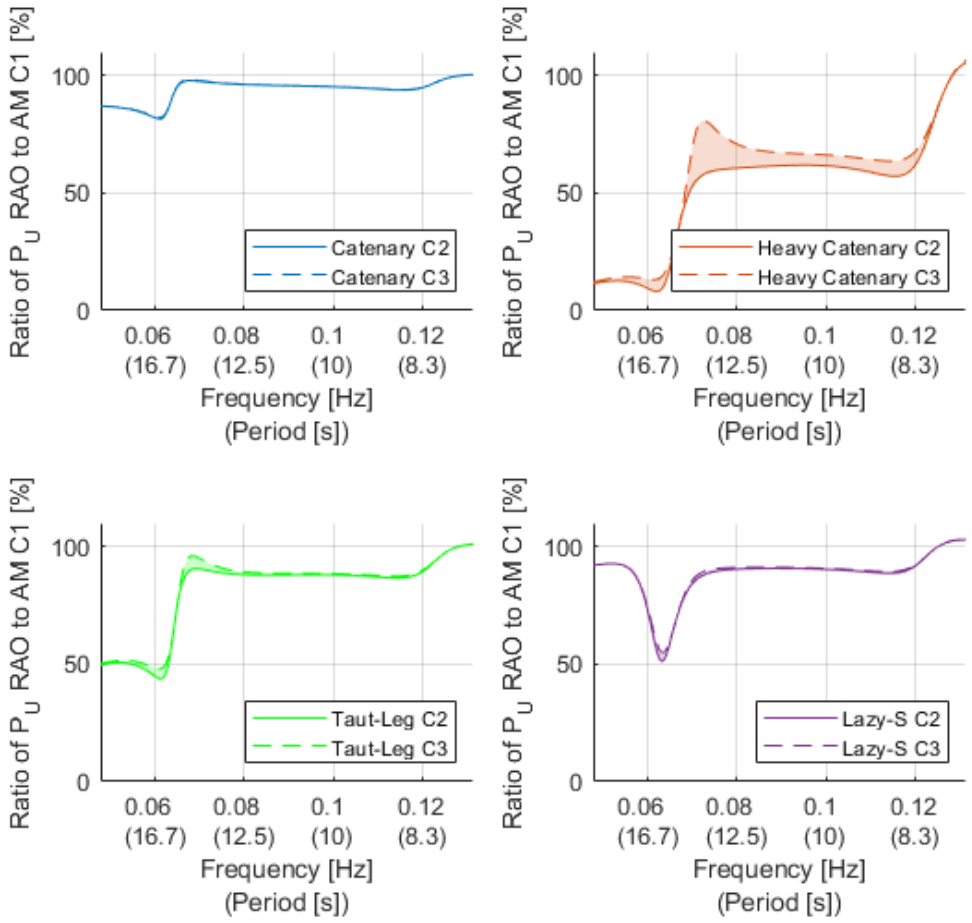

Figure 4-5 Useful power RAO of SRPA under AM control for case 2 and case 3 with each mooring. Expressed as a percentage normalized against case 1.

First, the general impact of the moorings on the power production is discussed. Note that the power response amplitude operator (RAO) is presented here rather than true power. The useful power can only be expressed as an RAO here because the wave excitation force in equation (4.8) was normalized to wave amplitude in the work of Beatty et al. [40]. In the case of AM control, each mooring has a significant impact on power production and is heavily dependent on the design of the mooring. The heavy catenary mooring has the greatest impact overall, reducing the useful power RAO to just 10% of the SRPA without the mooring. The regular catenary has the smallest effect and may be considered negligible. The magnitude of

effect the taut-leg mooring has is somewhere in between the two catenary moorings. Finally, the impact of lazy-S mooring has a different form, with a sharp dip at 0.65 Hz and otherwise moderate power reduction. A final note on the general shape is that the addition of the mooring would appear to increase the power capture at the upper end of the frequency range studied. The apparent increase in power is likely an artefact of the choice of mass-equivalency between all of the systems modelled. Mass-equivalency should lead to roughly similar overall dynamics, but some of the mass in each mooring moves very little, or not at all, and mass is effectively removed from the system. At high frequencies the reduced mass of the system leads to greater performance under AM control by bringing the imaginary part of the intrinsic impedance closer to zero and the SRPA closer to resonance.

The discussion of Figure 4-5 is concluded by observing the differences between cases 2 and 3. As a reminder, an increase in power from case 2 to case 3 indicates that designing the SRPA and controllers with knowledge of the mooring is useful. This increase is exactly what is observed and turns out to be strictly true throughout the range studied. Although, the impact is minimal for all but the heavy catenary mooring. The other designs provide some evidence for the claim that the mooring impact is the same regardless of any considerations in early design, but this is not the case for the other control types.

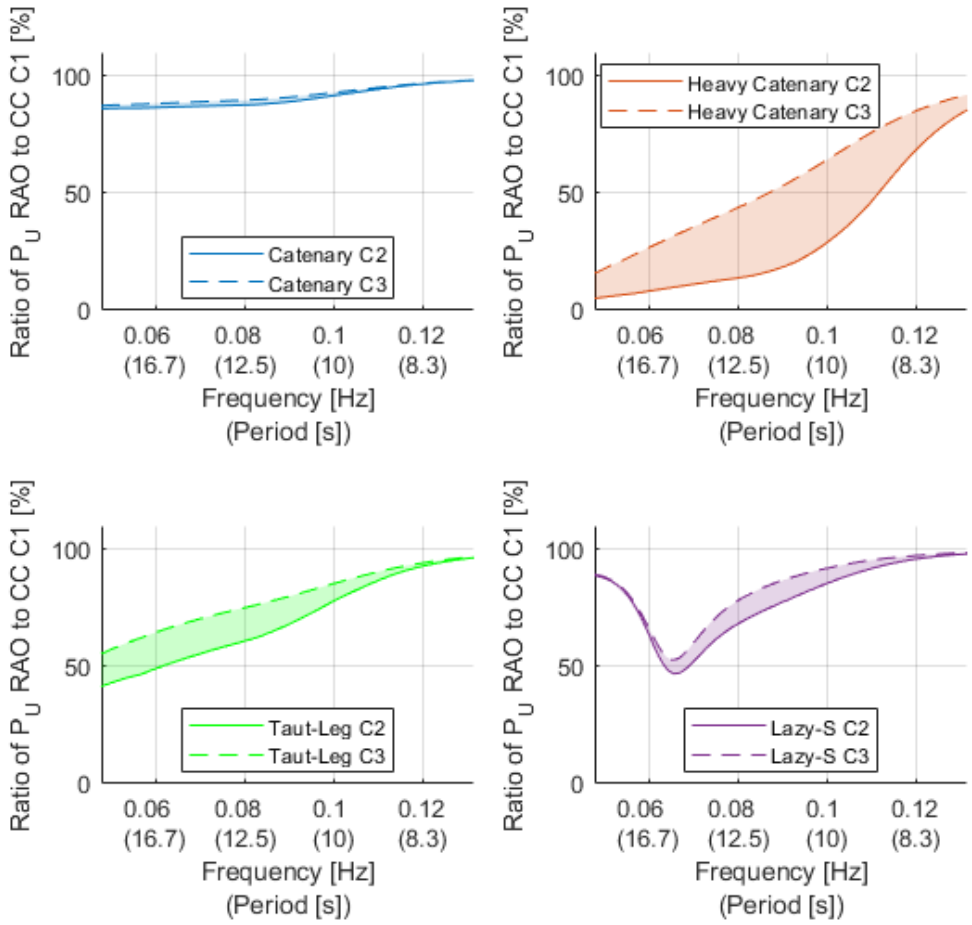

Figure 4-6 Useful power RAO of SRPA under CC control for case 2 and case 3 with each mooring. Expressed as a percentage normalized against case 1.

In terms of general impacts of the mooring on the useful power RAO, CC control is similar to AM control. The key result in Figure 4-6 is that cases 2 and 3 are drastically different. Including the catenary mooring in the design process still has a minimal impact, but the other mooring designs show increases in the useful power RAO of up to 35%. Note also that the apparent gain in power at high frequency is no longer present as the imaginary component of the intrinsic impedance is cancelled by the PTO and the SRPA is controlled to resonate with the excitation force for all frequencies.

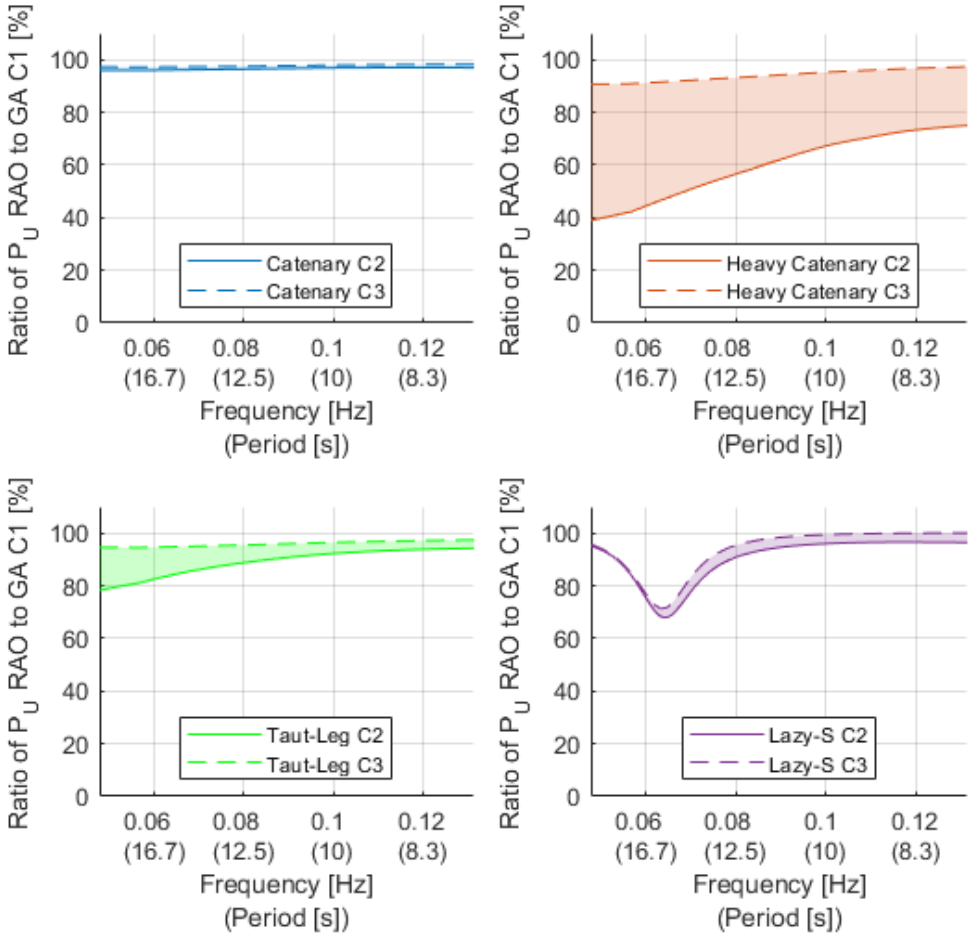

Figure 4-7 Useful power RAO of SRPA under GA control for case 2 and case 3 with each mooring. Expressed as a percentage normalized against case 1.

Finally, the effect the moorings have on an SRPA operating under GA control are discussed. Under this control type the mooring generally has less impact than complex-conjugate control. This reduced impact can be explained by the added benefit of master-follower control. Although this control type achieves the same resonant condition by cancelling the imaginary part of the intrinsic impedance it also brings the SRPA into a more energetic resonance as discussed by Bubbar et al. [13]. This resonant state was shown to have a low velocity amplitude, and the damping effects of the moorings is minimized as a result.

Interestingly, another effect of GA control is to slightly reduce the importance of including the mooring design in all cases except for the heavy catenary where it is greatly increased. The primary difference between the heavy catenary and other mooring designs is its large mass per unit length, which increases this mooring's impact on geometry control.

Some additional insights can be made from the data presented in Figure 4-5, Figure 4-6, and Figure 4-7 by integrating the average power RAOs to make a direct comparison of the power from each case and for each control type. Note that the vertical axes of Figure 4-8, Figure 4-9, and Figure 4-10 are each normalized to the power produced by case 1 for each control type and cannot be used to compare the control types.

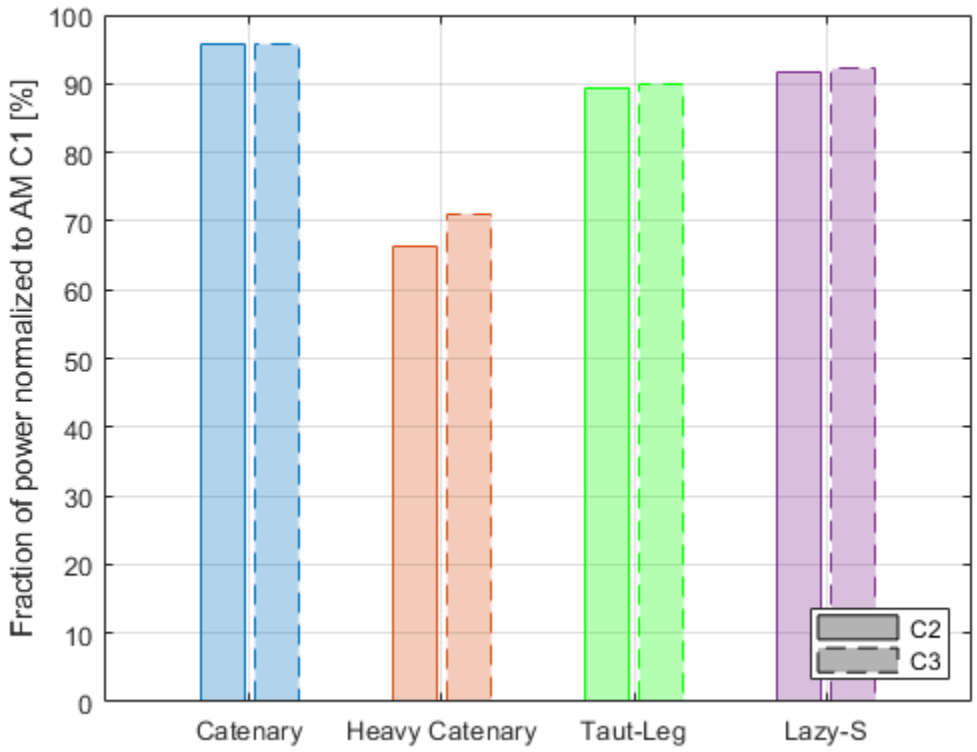

Figure 4-8 Integrated useful power RAO of SRPA with each mooring under AM control (normalized to AM control case 1).

Figure 4-8 reiterates that the difference in the integrates useful power RAO for all but the heavy catenary is insignificant when operating under AM control. The increase in power available by designing the controller with the heavy mooring model is 5%.

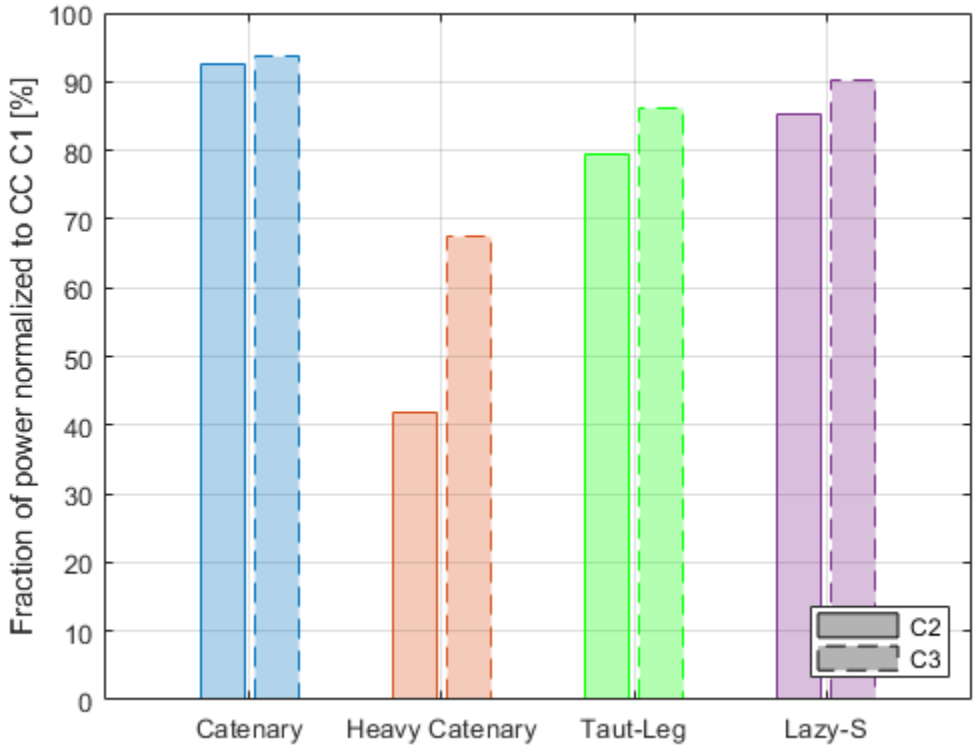

Figure 4-9 Integrated useful power RAO of SRPA with each mooring under CC control (normalized to CC control case 1).

Figure 4-9 shows greater dependence on the inclusion of the mooring model with a 6% and 5% difference for the taut-leg and lazy-S moorings and 25% difference for the heavy catenary design. The general impact of the moorings on the useful power RAO can also be reiterated. If any of these moorings would be suitable for deployment the best choices are the catenary, then the lazy-S, followed by the taut-leg and heavy catenary. As such, including the mooring in the power analysis may also be used as a method to inform the choice of mooring design. Applying this idea

with the detailed mooring analysis of section 3.7 could lead to an informed optimization of mooring designs to minimize the reduction in the useful power RAO.

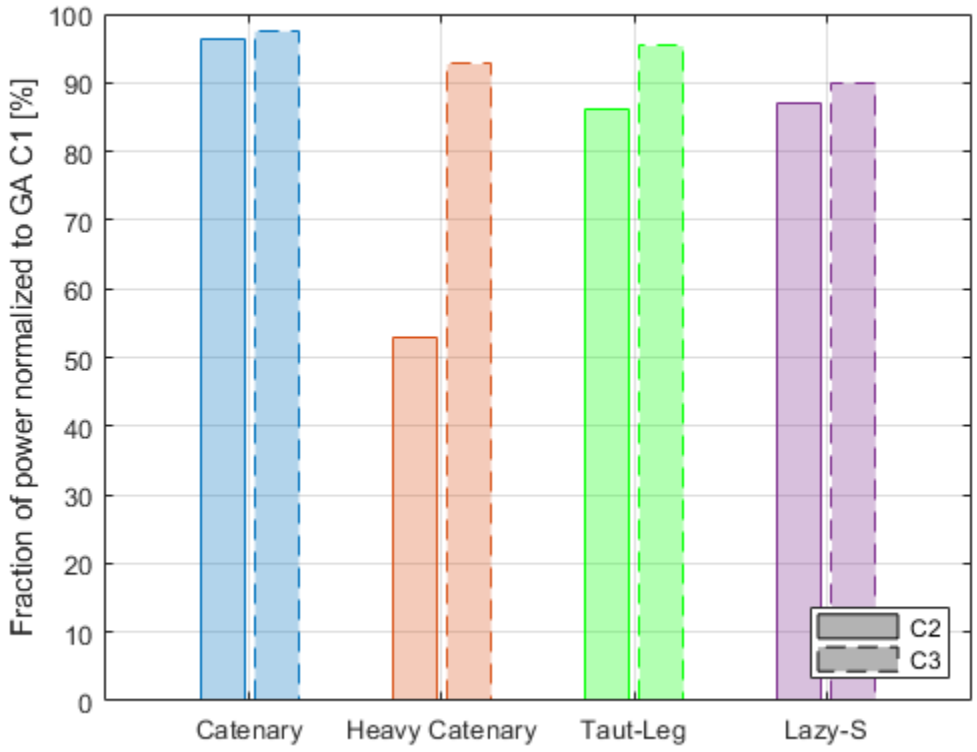

Figure 4-10 Integrated useful power RAO of SRPA with each mooring under GA control (normalized to GA control case 1).

Figure 4-10 shows the power for each mooring in case 3 is all greater than or equal to 90%, suggesting that the choice of mooring is less important under GA control. It also reiterates the large increase in power which is left behind for the heavy catenary if the mooring model is not included.

4.3.3 Comparison of Control Types

The plots of the previous section all expressed the power RAO of the moored SRPAs as a ratio to the power RAO of the unmoored SRPAs. Importantly, those plots were separated by control type, which could lead to the incorrect impression that each control type is as effective as

another. An additional comparison is made between A, CC, and GA control for each mooring to assess which control type has the best power performance with a mooring. The case 3 power RAO for each control type is normalized against the RAO of case 1 operating with GA control as shown in Figure 4-11 to Figure 4-14.

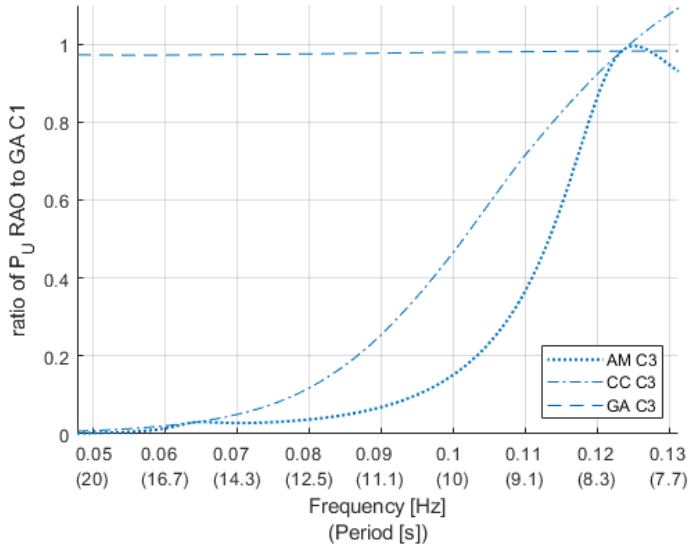

Figure 4-11 Useful power RAOs for SRPA with the catenary mooring operating under varied control. Expressed as a percentage normalized against GA control case 1.

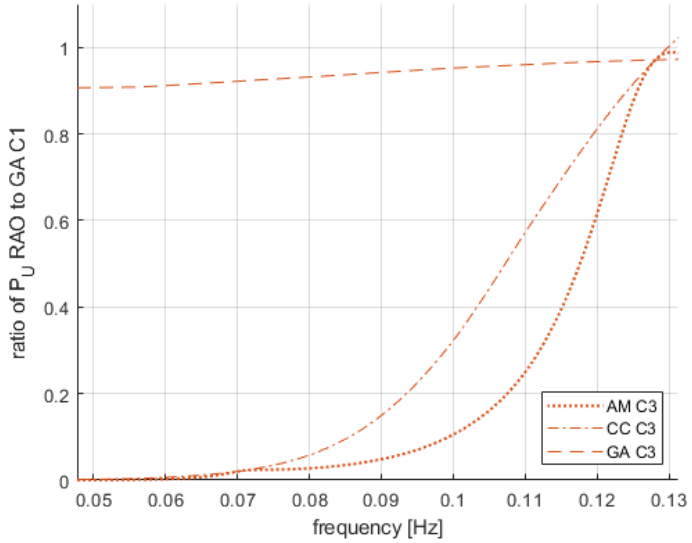

Figure 4-12 Useful power RAOs for SRPA with the heavy catenary mooring operating under varied control. Expressed as a percentage normalized against GA control case 1.

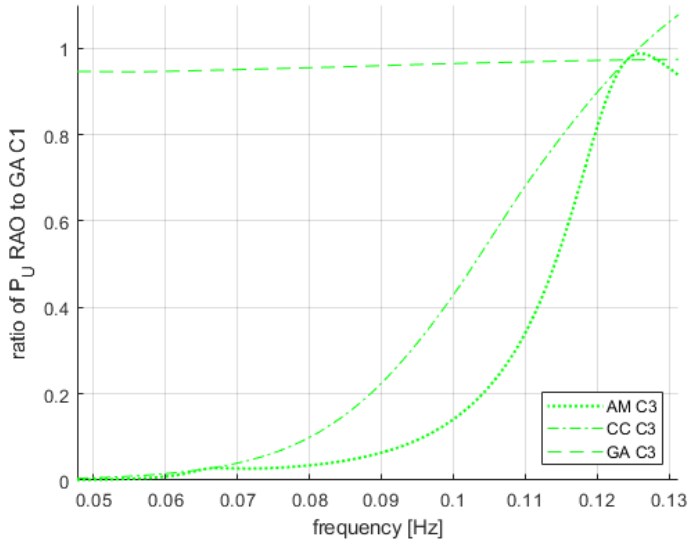

Figure 4-13 Useful power RAOs for SRPA with the taut-leg mooring operating under varied control. Expressed as a percentage normalized against GA control case 1.

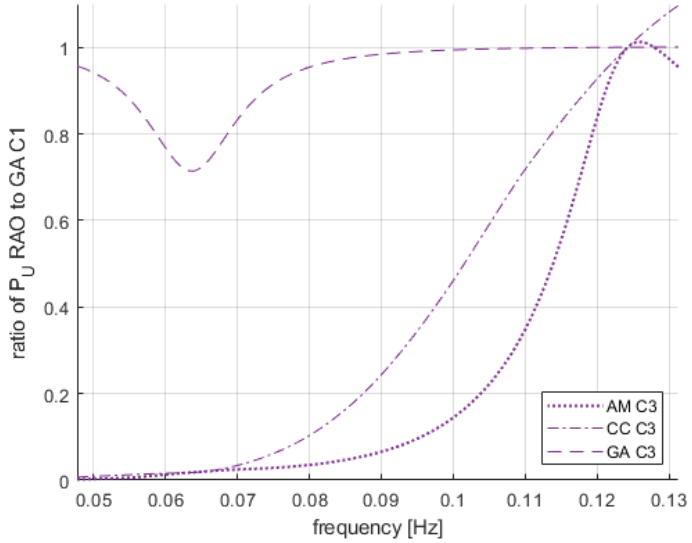

Figure 4-14 Useful power RAOs for SRPA with the lazy-S mooring operating under varied control. Expressed as a percentage normalized against GA control case 1.

Reflective of Figure 4-4, the useful power RAO resulting from GA control is orders of magnitude greater than AM or CC control for low frequencies for all four mooring designs. For higher frequencies AM and CC control slightly exceed GA control with and without the mooring.

However, it remains to be seen if those gains are significant for true power capture rather than the RAO. This idea is addressed in the following section and studied more rigorously in Chapter 5.

4.3.4 Impact on Control Design

The influence on the controller design is also investigated to paint a complete picture of the impact a mooring has on the SRPA. Cases 1 and 2 have identical control by definition, so only case 1 and 3 are compared. The control parameters and power RAOs stemming from each control type are plotted in Figure 4-15, Figure 4-16, and Figure 4-17. The same scale is used in each figure for comparison. The useful power RAO subplot includes the shadow of the PM spectra at the studied site to provide context as to how important any differences in the useful power RAO are. For example, if the useful power RAO of one control type is largely the same for low frequencies, but much greater than another at high frequencies where there is little variance density, the actual power gain of that type of control is small.

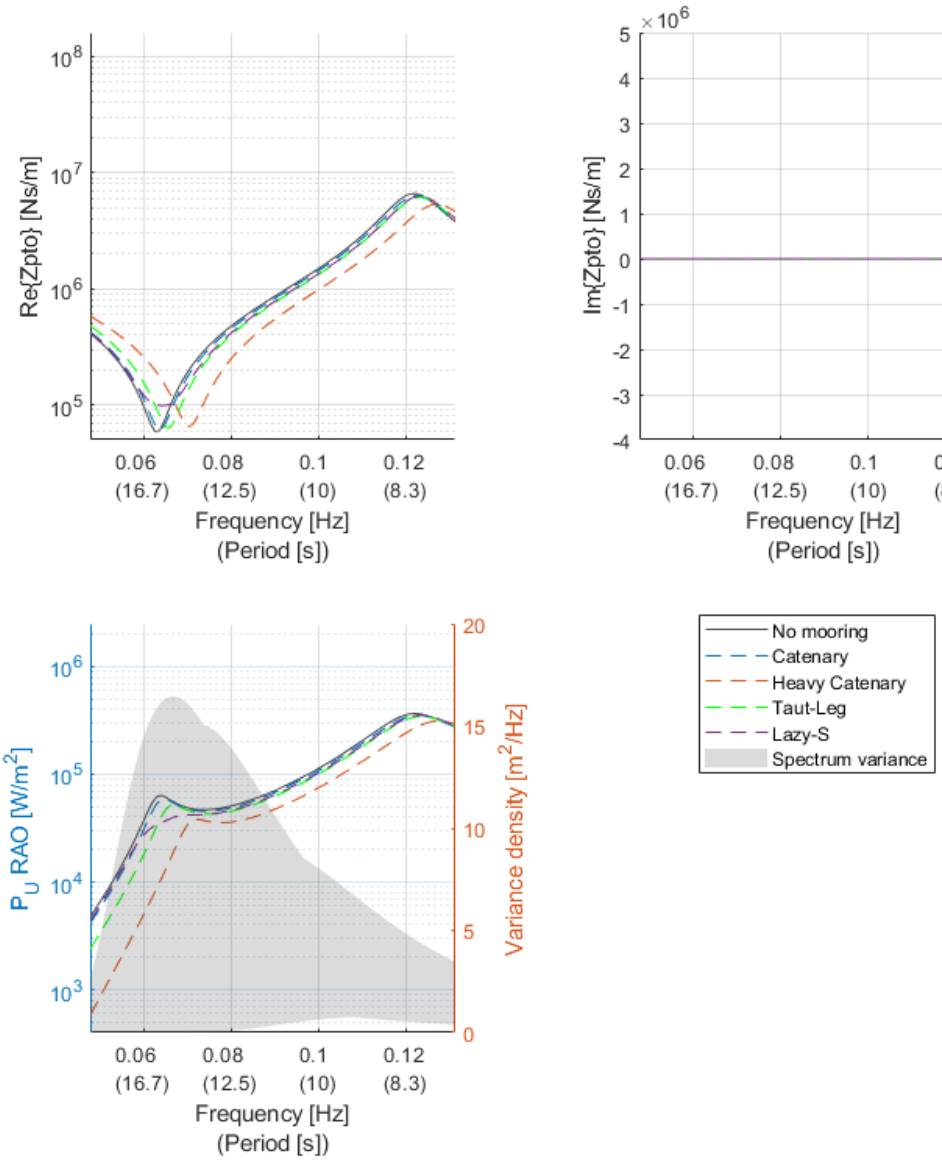

Figure 4-15 Impact of mooring designs on AM control impedance (top) and useful power RAO (bottom left).

Under AM control the PTO has no imaginary component, but the moorings have an interesting effect on the real component. Each mooring tends to reduce the maximum impedance necessary to control the SRPA. The heavy catenary reduces the peak by 30% while the lazy-S increases the trough by 30% and the others have a smaller impact of 8%. The reduction of the peak and increase to the trough is significant because a controller which must be able to achieve a large range of impedances would tend to be more expensive. By including the mooring design in the early stages of WEC design an Engineer may also reduce the cost of the PTO by ensuring it is not overdesigned.

In terms of power, AM control results in the highest power RAO where there are the least energetic waves. There is a peak with each mooring design between 0.06 Hz and 0.07 Hz where the most energetic waves are, but this peak is an order of magnitude smaller than the primary peak which was near 0.12 Hz for each mooring design. Also notable in Figure 4-15 is the relative impact of each mooring design on the useful power of the SRPA. The catenary and taut-leg moorings closely follow the no-mooring case, but the lazy-S design significantly reduces the peak at 0.65 Hz while the heavy catenary reduces and shifts it to 0.7 Hz.

Notably, adding any of the moorings to the system strictly reduced the power from the no-mooring case. This reduction occurs despite the mooring impedances having the effect of increasing the PTO damping for some frequencies while increasing it for others. The amplitude control equation uses the magnitude of the intrinsic impedance which complicates any intuition, so discussion of the interaction between the mooring impedance, controller impedance, and power RAO is pursued in the discussion of CC control.

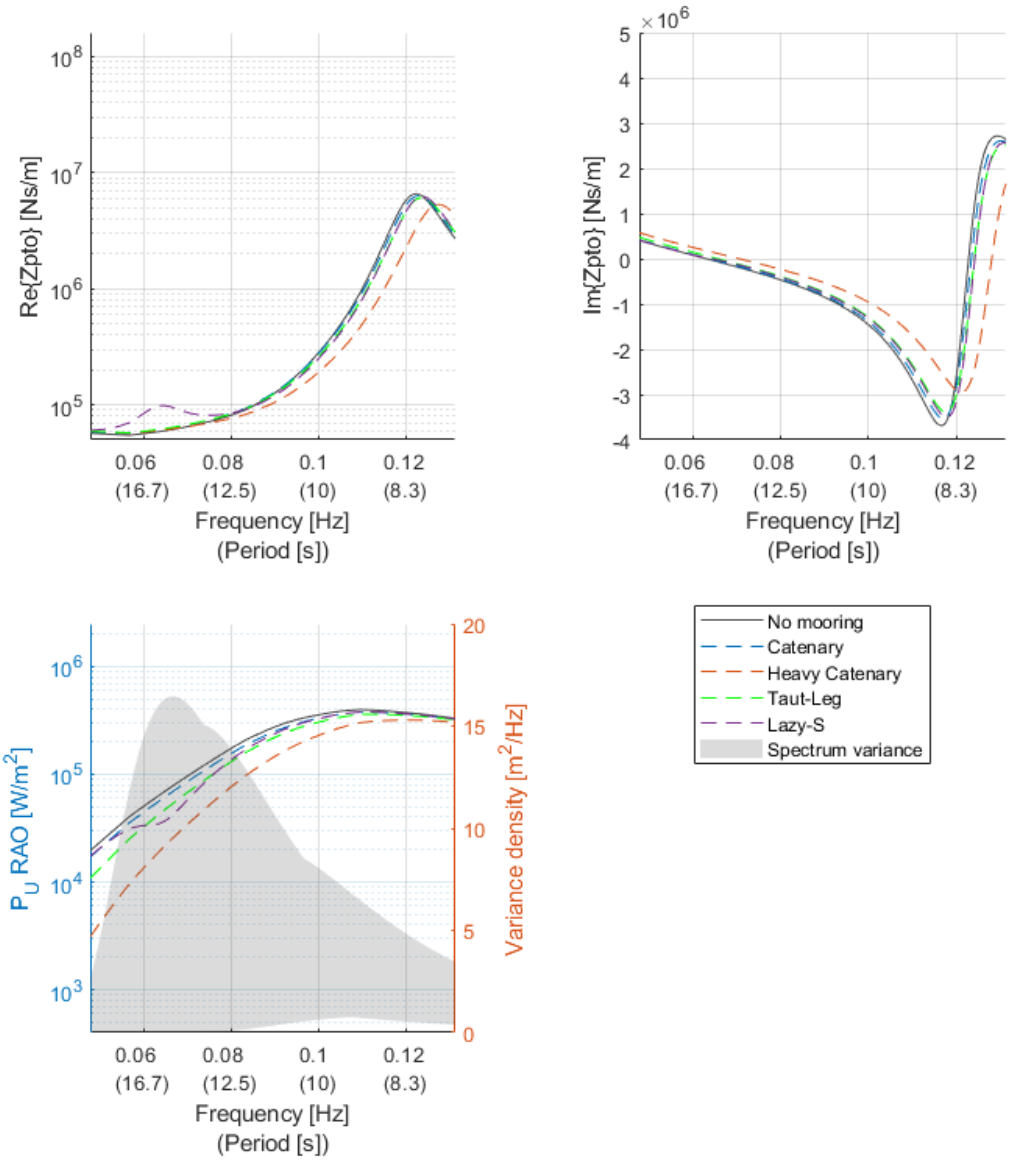

Figure 4-16 Impact of mooring designs on CC control impedance (top) and useful power RAO (bottom left).

Complex-conjugate control has a similar effect as AM control on the real part of the PTO, but the moorings also affect the imaginary part. Again, the heavy catenary mooring had the greatest impact on the range of the impedances, reducing the peak of the real part by 30% and the bounds of the imaginary part by 40%. The other moorings reduced the peak of the real part and bounds of the imaginary part by 7%. As a coincidence of the condition for CC control from equation (4.3), Figure 4-16 also depicts the intrinsic impedance of the SRPA with the sign swapped on the imaginary part. From this perspective it is interesting to observe that moorings tend to reduce the overall damping in the intrinsic impedance of the SRPA.

Continuing the discussion on the impact of the mooring impedance on power, one may expect that reducing damping would increase the useful power RAO since a lower damping suggests less energy is leaving the system, but that intuition neglects the system dynamics and control. When damping is reduced, Thevenin equivalent velocity increases as per equation (4.2) However, since the optimal control laws all base the PTO damping on the intrinsic impedance, the PTO damping is also reduced. The expression for the useful power RAO given in equation (4.8) demonstrates that the changes to the Thevenin equivalent velocity and PTO damping would increase and decrease the useful power RAO respectively. For the parameters of the SRPA and CC control, the reduction of the PTO damping dominates, and the useful power RAO is reduced in the frequency range studied.

As expected from the previous analyses of power, CC control leads to a greater useful power RAO than AM control but converges with AM control at 0.65 Hz. This frequency is where the optimal CC control is equal to AM control. This frequency is indicated by where the imaginary part of the PTO impedance crosses zero.

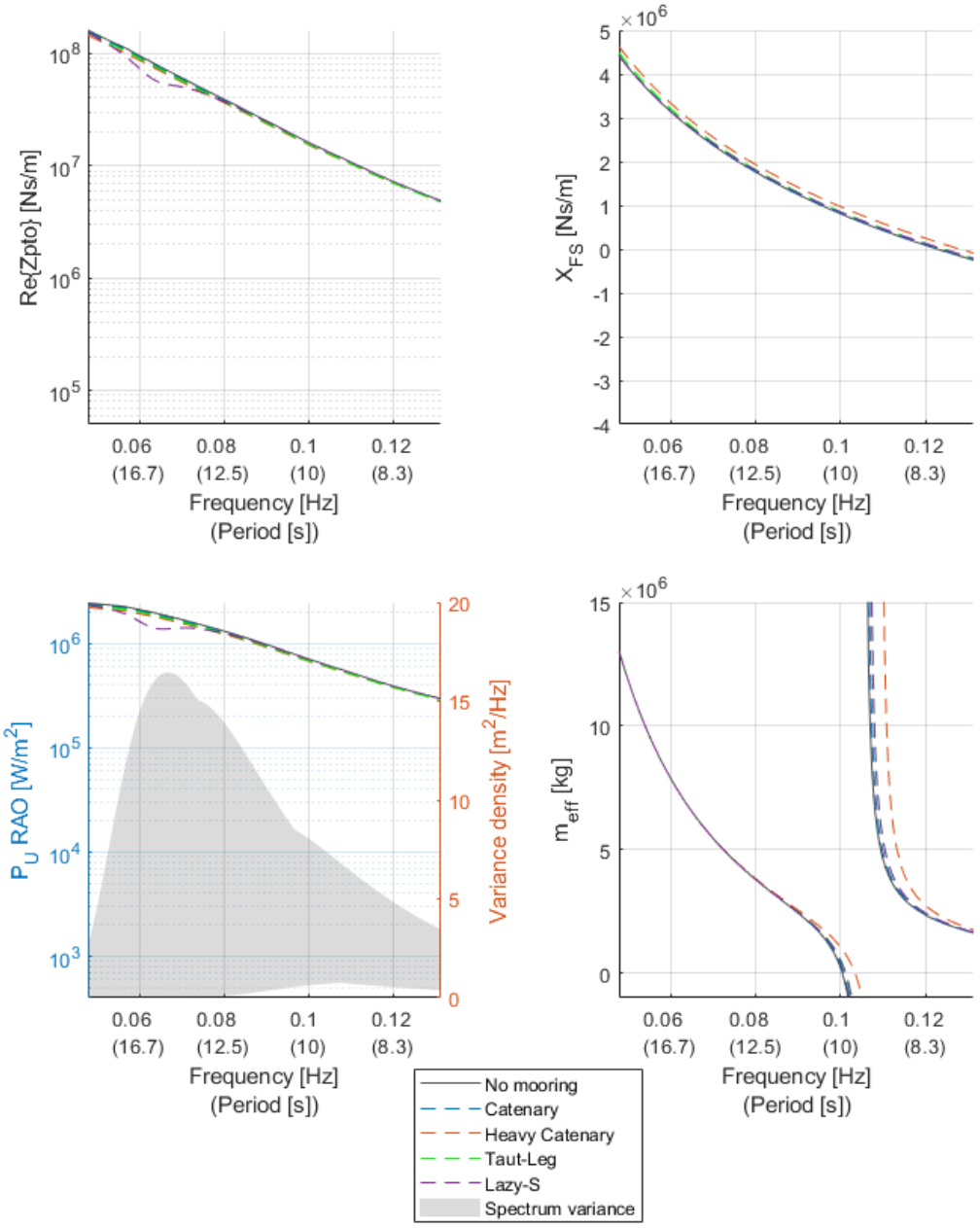

Figure 4-17 Impact of mooring designs on GA control impedances (top), useful power RAO (bottom left), and effective mass of inerter (bottom right).

Under GA control the tendency to reduce the peak impedances seen in AM and CC control is lost. In fact, and adding the mooring systems requires a slightly increased impedance from the reactive force source. Interestingly, the mooring has a positive impact on the necessary effective mass of the inerter. The effective mass necessary for control is calculated by rearranging equation (2.40) to solve for m_{eff}:

$$m_{eff}(\omega) = \frac{-\omega^2 m_3 X_{FS}(\omega) - \omega m_3 k + k X_{FS}(\omega)}{-\omega^3 + \omega^2 X_{FS}(\omega)} \tag{4.9}$$

The choice of reaction mass m_3 and spring stiffness k are made to be consistent with previous work by Bubbar et al. for ease of comparison [13], although it is important to highlight that these are creative choices which may warrant further study. The reaction mass is set to 898 tonnes, which is the full-scale equivalent of the reaction mass used by Bubbar et al. The spring stiffness k is set to 588 kN/m to balance the weight of the reaction mass when it is at the centre of its travel inside the spar. Then, the optimal force source reactance is used to solve for the effective mass of the inerter as shown in the bottom-right of Figure 4-17.

Two key features of the resulting function are the zero-crossing frequency and asymptote. The zero-crossing frequency is informative since the effective mass must be greater than or equal to zero as discussed in section 2.1. Obviously, control is not achievable at the asymptote of the function, since the limits from either side approach positive and negative infinity, but it indicates where the control begins to be feasible again. These features define the unoptimizable frequency band where control with the reactive force source implementation discussed is possible.

The moorings have the effect of increasing the required effective mass of the inerter with the largest change near the asymptote. This increase would be detrimental, as a larger control effort

would be required from the inerter, except that the moorings have a negligible effect at low frequencies which indicate the upper limit of the effective mass needed for control. In fact, the moorings have a somewhat positive effect, slightly increasing the zero-crossing frequency and the asymptote frequency. This shift has a positive effect despite the width of the unoptimizable frequency band not changing because the lower frequencies contain much more power than the higher ones. Again, the heavy catenary has the largest effect and could inform on design changes to shift the unoptimizable frequency band beyond typical ocean wave frequencies.

Overall, the impact of a mooring system on the SRPA controllers studied varies significantly with the control type used as well as the design of the mooring. Notably, the heavy catenary mooring tends to reduce the control effort of AM and CC control the most, while the others have a smaller effect on the control design.

Chapter 5

Impact of Control Choice on Annual Energy Production

The final contribution of this thesis is to assess if the competitive advantage of geometry control over complex-conjugate and amplitude control is eroded by the presence of the mooring. In this case, competitive advantage is defined in terms of annual energy production of the moored SRPA model studied over an average year in a realistic sea. Up to now, the performance of the moored SRPA has only been considered across a range of monochromatic inputs, so a method for assessing performance in a polychromatic spectrum is also introduced. An extensive data set defining non-directional wave spectra at a sample deployment site off the West Coast of Vancouver Island is employed to generate the sea states and then to compute moored SRPA energy conversion at an hourly resolution. The goal is to determine the sensitivity of annual energy production to the choice of control type and knowledge of the mooring.

Shifting from a monochromatic to a polychromatic study is not trivial however. In Chapter 4 each control type was studied on a frequency-to-frequency basis with the optimal response computed for each frequency. Those results provide little indication as to how a moored SRPA would respond to waves at frequencies it had not been optimized for. The chief issue is that looking at the control problem in the frequency domain leads to an optimal impedance of the PTO and reactive force source for each frequency, while in reality, multiple waves at differing frequencies may be exciting the SRPA at the same moment.

Due to this reality, implementing SRPA controllers in the time domain is an area of continued research. Bacelli states the two main issues of control in the time domain are that of noncausality and nonlinearities and proposes a control scheme which simplifies these problems [57]. Another approach was employed Faedo et al. which similarly simplified the model and made it suitable for forming a control problem which could be solved in real time [58]. Such approaches are typically improved by predicting future wave elevations to achieve active control in the time domain as was done in a more recent study by Faedo et al. [59]. Further, others such as Anderlini et al. have made use of recent developments in machine learning to estimate the future wave elevations with some degree of success [60].

Research on WEC control in the time domain tends to focus on active control approaches where an effort is made to extract the most power on a wave-to-wave basis. This is realized by making constant adjustments at the controller to keep the force and velocity response across the PTO in phase at all times. In contrast, an alternative approach which more easily bridges the gap between frequency and time domain is passive control. A passive control approach makes adjustments to the controller on a longer time scale by selecting an impedance to operate with for a given length of time that maximizes power within that constraint.

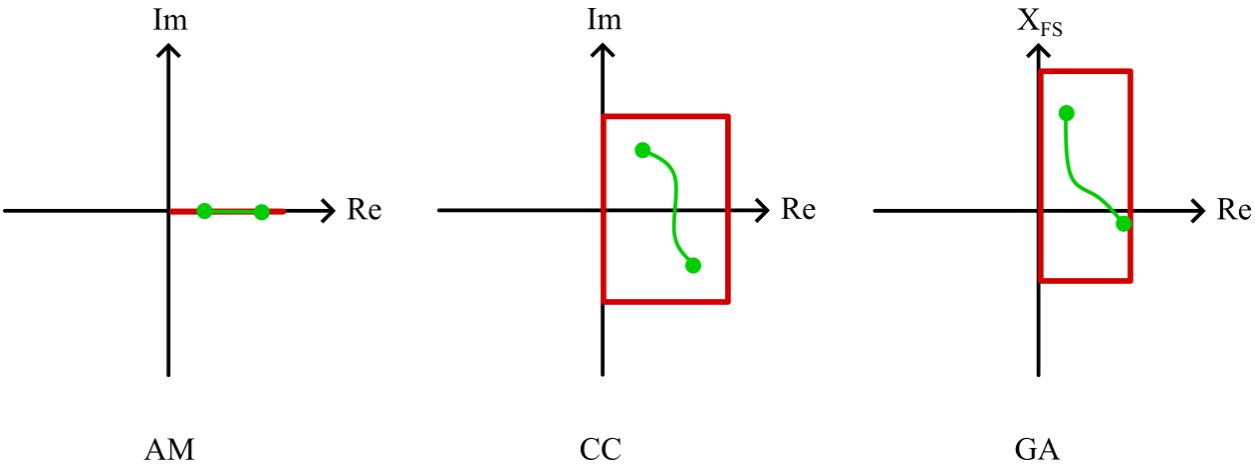

Figure 5-1 Visualization of differences between types of control and control approaches.

The discussion of active versus passive control approaches also provides an opportunity to delineate between control approaches and control types as keywords used in this work. The type of control concerns the physical design and choice of controller, while the control approach governs the variation of the control variables in that space. These concepts are visualized in Figure 5-1 which depicts the three control types discussed in this work, the limitations each type has on the range of control variable, and the control variable points and paths within as determined by the control approach. The choice of control type defines the bounds of the control variable shown in red with AM control limited to positive real values, while the CC control variable also has an imaginary component, and GA control operates in a different plane by controlling X_{FS}. The choice of control approach determines which points or impedances shown in green should be applied in any given moment to yield maximum useful power. The difference between active and passive control approaches in this analogy is the time step between changing from one impedance to next and the path taken to get there. Active control changes impedances often and quickly while passive control changes slowly or less frequently.

Since the master-follower type of control is new to the study of SRPAs, the choice made in this work is to apply a simple control approach which is easily understood in the time domain, but is based on the fundamentals of frequency domain control. The passive control approach applied herein consists of selecting a single impedance for the controllers to operate under based on the current sea state. This approach is referred to in this work as sea state-based (SSB) to differentiate this implementation from the general concept of passive control.

Applying the SSB control approach reduces the decision of selecting the control variables from a line or plane as depicted in Figure 5-1 to a single point for each frequency. This reduction is achieved by making use of the optimal controller impedances from the monochromatic study of each control type as shown in Figure 4-15, Figure 4-16, and Figure 4-17 for AM, CC, and GA control respectively. For those control types the control impedances were a function of frequency, so the choice of impedance is fundamentally a choice of frequency. Any deviations from those impedances leads to a reduction in power in the monochromatic case, and should yield the same result for the polychromatic case. Some power can still be collected from waves with frequencies above and below the tuned frequency, but this would be expected to decrease for more distant frequencies as the optimal impedances corresponding with those frequencies increasingly differ from the actual impedance of the controller. Despite this, using the SSB control approach has the beneficial effect of reducing the question of which impedances to use down to which frequency to *tune* to.

However, the SSB control approach as described thus far provides no indication as to what frequency to actually tune to for any particular sea-state. Analyzing a sea-state as a spectrum reveals the frequencies of waves which comprise it, and it follows that the tuned frequency should

be taken from one of those. However, the question remains of which of those frequencies results in the most SRPA power, or restated: which frequency is the best to tune to?

5.1 Selected Site and Wave Data

An estimation of annual power production requires wave elevation data. The wave elevation data used in this work is sourced from a SWAN (Simulating Waves Nearshore) model developed by Delft University of Technology in the Netherlands and previously used to model ocean wave propagation off the West Coast of Canada [7]. The specific data used in this work stems from a resource assessment completed by the Pacific Regional Institute for Marine Energy Discovery (PRIMED) at a prospective wave energy site near Nootka Island [48]. The data was generated using the SWAN model in the region and validated with buoy data near the site.

By utilizing the SWAN model, a hindcast of wave data from 2004 to 2014 could be generated and used to estimate the average annual occurrences of each sea state. The histories of the significant wave heights H_{m0} and energy periods T_e of each spectrum are binned to create the histogram in Figure 5-2. Since the SRPA has radial symmetry the direction of the waves has no bearing on its motion and knowledge of the significant wave heights and energy periods alone are sufficient to compute its power response.

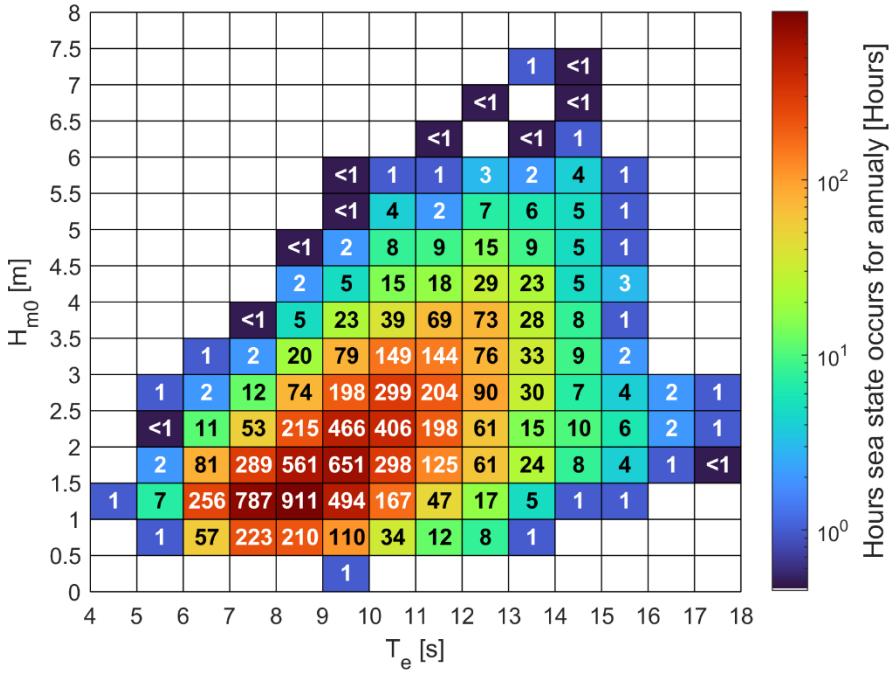

Figure 5-2 Average number of hours per year which each sea state occurs for at Nootka Island site. Reproduced from PRIMED resource assessment [48].

5.2 Device Configuration

Since a detailed comparison of the power capture of an SRPA with various moorings has already been completed in Chapter 4 , this chapter focuses on the competitive advantage of GA control. The catenary mooring is selected from the four for having the least impact on power with 95%-97% of the no-mooring power being preserved as shown in Figure 4-8, Figure 4-9, and Figure 4-10. As such, just the catenary mooring is used going forward with comparisons made between the three types of control studied: AM, CC, and GA control.

5.3 Controller Setpoint in Irregular Wave Conditions

With knowledge of the sea states which occur at a site, one may compute an estimate of the useful power which can be extracted by the SRPA model for each sea state. This computation may be completed for any configuration of the controllers. By also making use of knowledge of how long each sea state occurs for each year, the annual energy production may also be estimated for

each control configuration. The annual energy production serves as a single value for comparing the performance of the SRPA while operating under each control configuration.

5.3.1 Wave Heights

A series of Pierson-Moskowitz (PM) spectra are generated from the bins of significant wave height and energy period using the same approach as in section 3.5. In section 3.5, wave spectra were used to determine frequency and wave height ranges; here, the aim is to accurately represent the PM spectra. A spectrum can be discretized into any number of points N, with $N = 200$ used in this work for a smooth fit. Each point represents a bin of variance with some width Δf and height S_i. Each bin represents a monochromatic wave with a frequency f_i from the centre of the bin as shown in Figure 5-3.

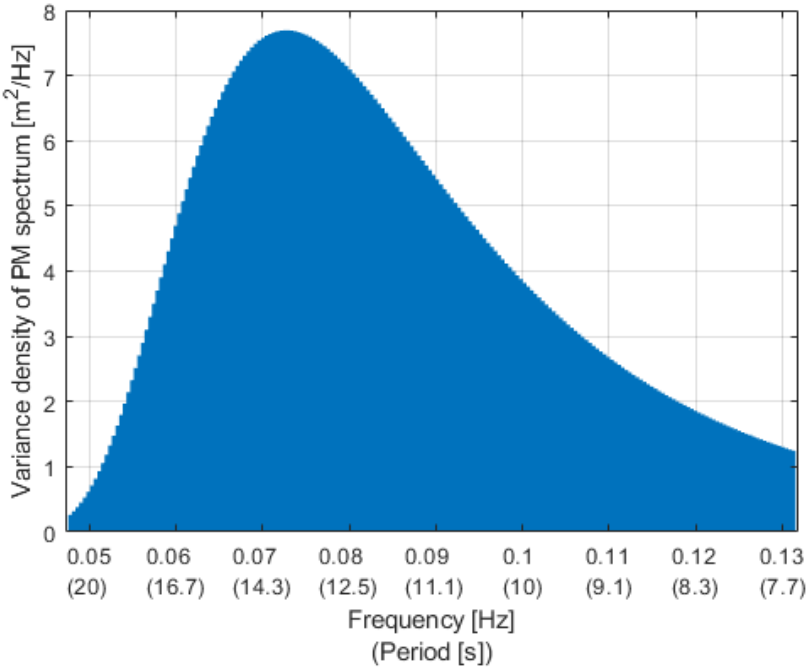

Figure 5-3 Variance density of PM spectrum expressed with individual bins.

The wave amplitude at each frequency is calculated from the binned variance density spectrum using the bin height and width. An example of the wave amplitudes for a PM spectrum are shown in Figure 5-4.

$$A_{wi} = \sqrt{2S_i \Delta f} \tag{5.1}$$

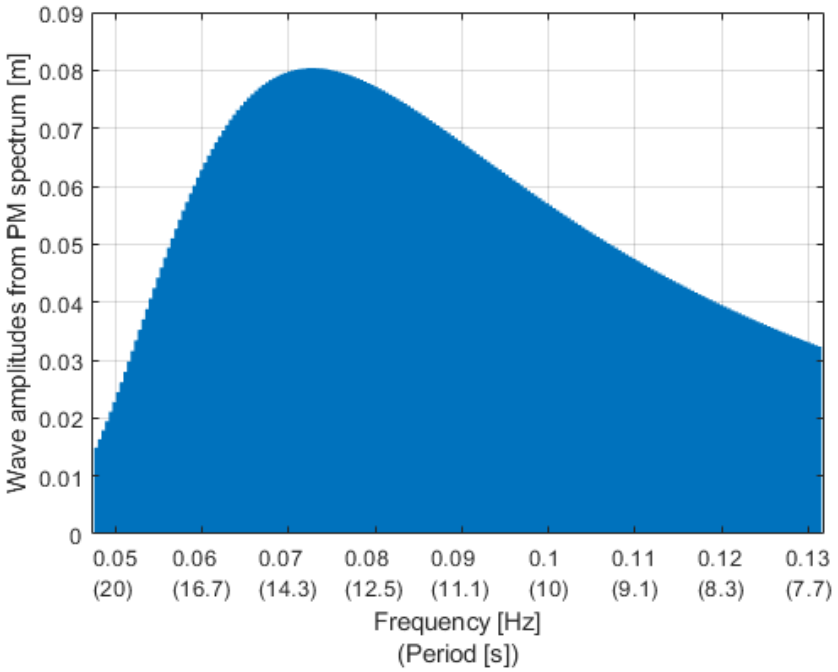

Figure 5-4 Example of wave heights from a PM spectrum used in power calculation.

5.3.2 Response Amplitude Operator in Sea-State Based Control

The study of SRPA power in Chapter 4 showed an RAO with optimal power at each frequency, but that RAO is not representative of the SSB control approach.

It is critical to highlight once more the distinction between the types of control which can be applied to the SRPA and the SSB control approach which governs the implementation of those types of control. The type of control is defined by the design of the control system with examples from this work being AM, CC, and GA control. Meanwhile, the approach defines how an operator

chooses to make use of the gains made available by those control types. Figure 5-5 displays the control hierarchy with the input and output variables of each.

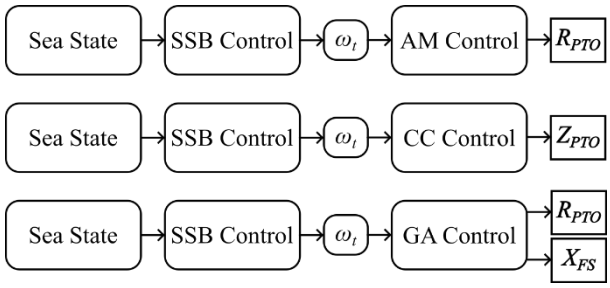

Figure 5-5 Hierarchy of control approach, control type, and control variables.

As described, SSB control utilizes knowledge of the current sea state to determine an optimal frequency to tune the SRPA controller to. Then, that optimal frequency is used by each of the control types to set the impedance of the PTO and reactive force source and tuning the SRPA to that frequency. In the frequency domain this is realized by setting the PTO and reactive force source to a single impedance across the entire frequency range.

As mentioned, the choice of SSB control as the control approach will impact the power RAO as the impedance can only be optimal at the tuned frequency ω_t. Knowledge of the optimal impedance at each frequency may be used to inform the decision of what impedance value to use, but the choice of which frequency to tune to is not necessarily obvious.

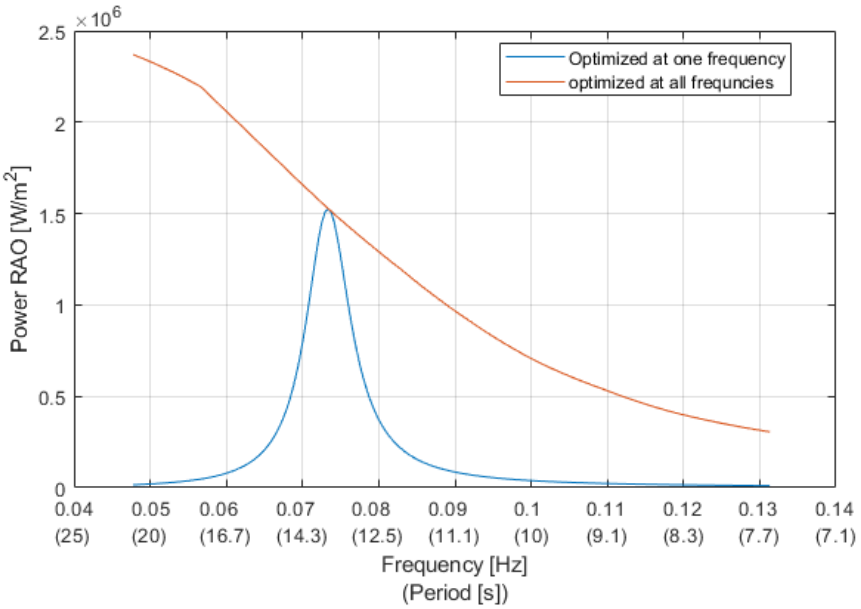

Figure 5-6 Example of SRPA power RAO with GA controllers set to optimal values at 0.073 Hz.

A comparison of the RAO for GA control from Chapter 4 with an RAO with constant impedances across the frequency range is given in Figure 5-6. This RAO is produced by setting the system to $\omega_t = 0.073\,\text{Hz}$, and the power RAO rapidly recedes below the optimal case above and below this frequency.

5.3.3 Power Calculation

Working in the context of linear circuits allows the use of the superposition theorem from the study of electric circuits. Superposition theorem states that the current, voltage, and power associated with a circuit element can be found by solving the circuit for each oscillating source individually and summing the results [61]. As such, the total power produced by the PTO is the sum of the power from each wave in the spectrum.

$$P_U = \sum_{i=1}^{N} P_{Ui} \tag{5.2}$$

Before Chapter 5, power has been presented in W/m^2, which is normalized to wave amplitude squared. The true power generated by the SRPA is proportional to the square of the wave amplitude A_w as shown in equation (5.3) and in the middle of Figure 5-7.

$$P_{Ui}\left(\omega_t\right) = P_{RAO}\left(\omega_t\right) A_{wi}^2 \tag{5.3}$$

Equations (5.2) and (5.3) may be combined to compute the useful power as the dot product of the discrete power RAO and the square of the binned wave amplitudes as described by equation (5.4). An example of this result in shown in the bottom of Figure 5-7.

$$P_U\left(\omega_t\right) = P_{RAO}\left(\omega, \omega_t\right) \bullet A_w^2(\omega) \tag{5.4}$$

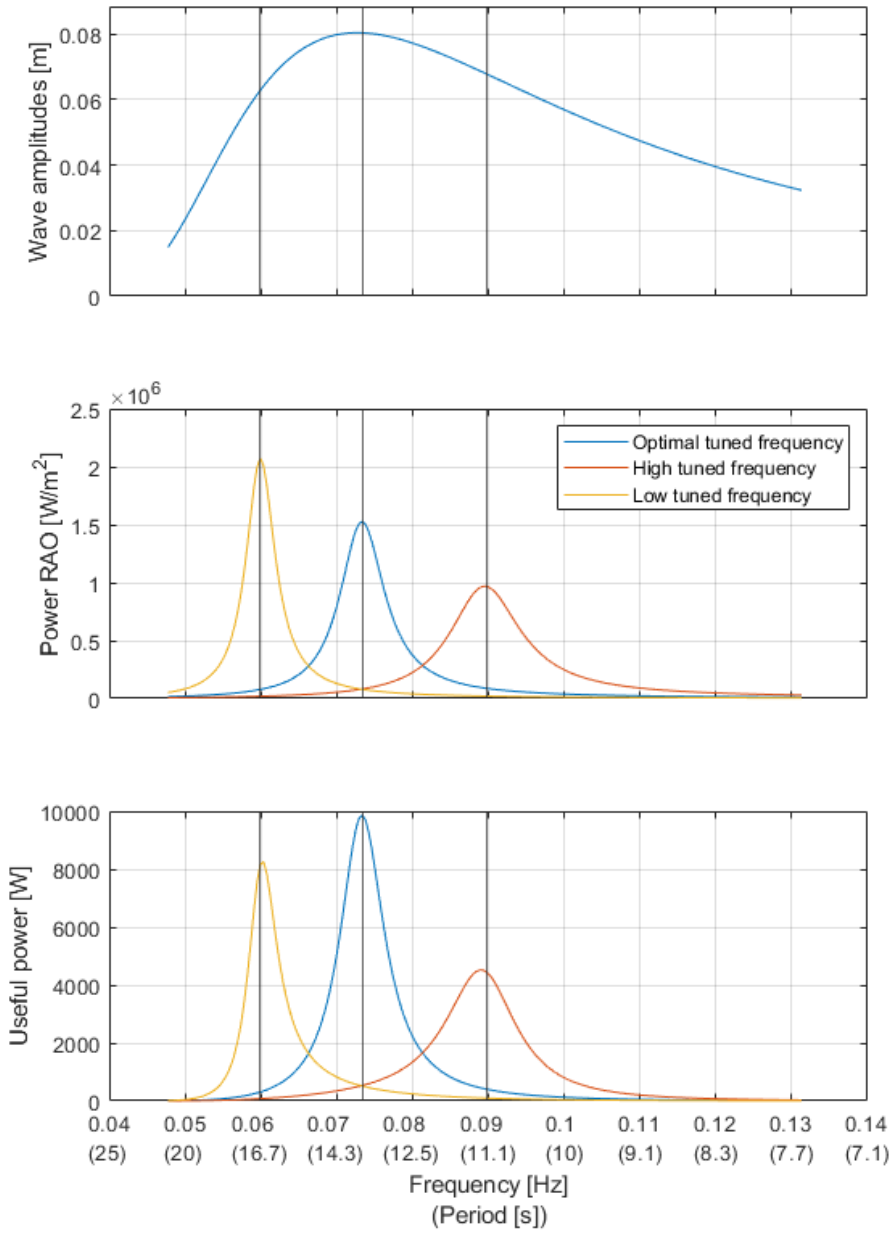

Figure 5-7 Example of wave amplitude from a sea state (top), power RAOs for various ω_t (middle), and corresponding useful power (bottom).

Figure 5-7 highlights that the tuned frequency with the greater RAO does not necessarily lead to the greatest useful power. This property stems from the variation in wave amplitudes for the given spectrum. Comparing the peaks in middle and bottom plots of Figure 5-7 also provides

some insight. The peaks of the power RAO align with the tuned frequency as expected, while the peaks of the useful power plot are skewed towards the peak of the spectrum. This skewing occurs because more wave power is available towards the peak frequency and the power RAOs for each tuned frequency are of a similar scale. This example suggests the maximum power for SSB control should be achieved by tuning to the peak frequency of the spectrum, but this may be a special case or only a local optimum.

With a method for computing SRPA output power in an irregular wave condition and a guess as to the optimal tuned frequency, the next step is to determine if that guess is correct or if another tuned frequency maximizes useful power. The maximum useful power can be found by selecting a frequency to tune to, computing the resulting RAO (middle of Figure 5-7) and power extracted from the given sea state (bottom of Figure 5-7), and comparing the total power generated for each selected frequency. This total is computed by summing the power contributions of each bin of the power RAO from the bottom of Figure 5-7 for each spectrum and tuned frequency. The tuned frequency setpoint which results in the most power is then the optimal frequency for the SSB control approach.

Figure 5-8 depicts the total power produced by the SRPA operating in a wave spectrum when tuned to a range of frequencies. The wave spectrum is also plotted to provide a comparison but is not a one-to-one mapping to average useful power. For example, tuning to 0.11 Hz for the spectrum given in Figure 5-8 results in a total average useful power of 75 kW which is sourced from across the spectrum rather than just the bin at 0.11 Hz. Similar plots for the twenty most energetic sea states are given in Appendix D – Average Power in PM Spectra. The tuned frequency that yields maximum power is marked by the vertical line.

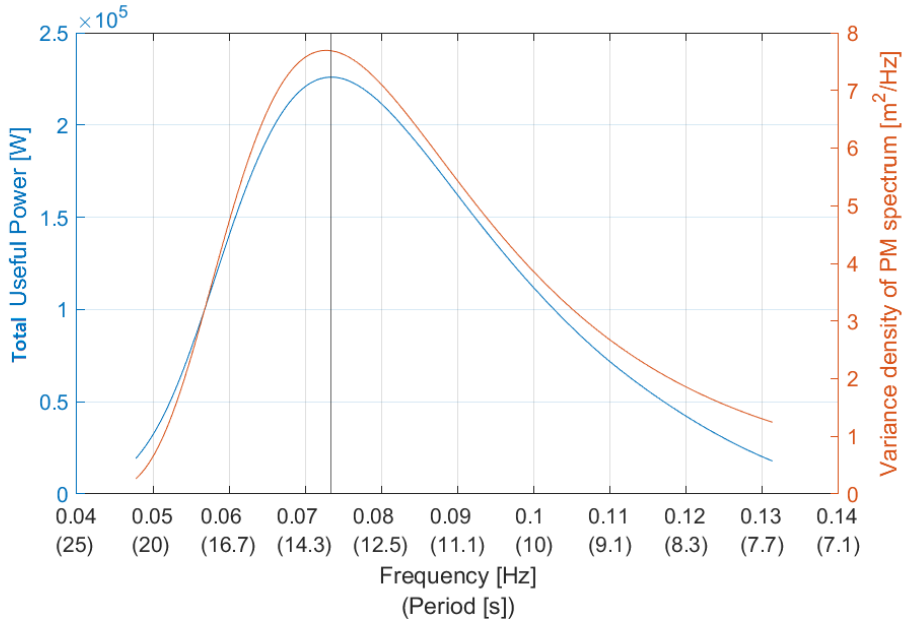

Figure 5-8 Comparison of total useful power extracted from a PM wave spectrum by an SRPA optimized for various frequencies.

Figure 5-8 indicates that the tuned frequency which yields the most power is at or near the peak frequency, but this is not true in all cases.

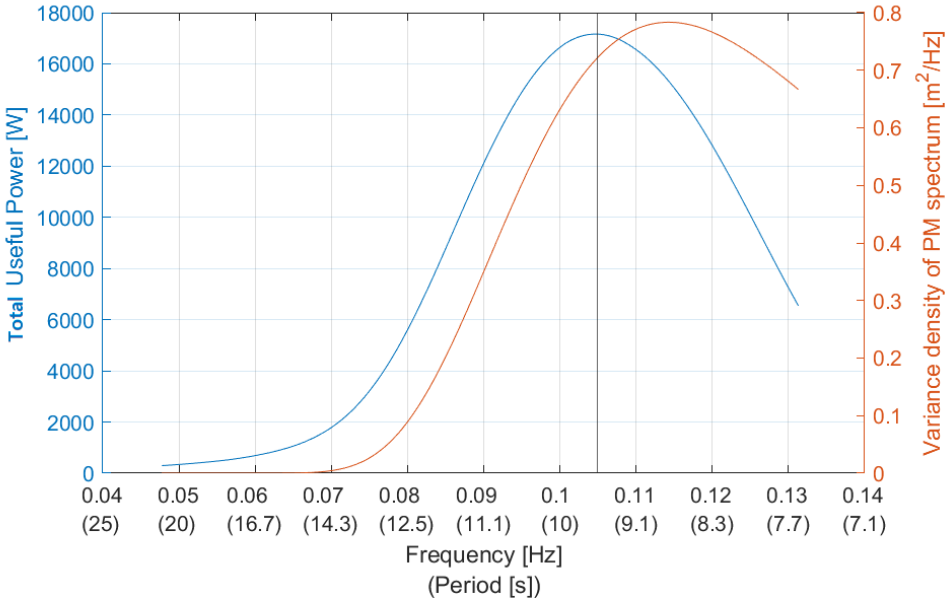

Figure 5-9 Comparison of useful power of an SRPA optimized for various frequencies and another PM spectrum.

Another example from the twenty spectra studied is shown in Figure 5-9. In this spectrum the optimal frequency is 0.105 Hz – notably lower than the peak of the spectrum. However, the frequency range is limited by the lack of hydrodynamic coefficient data for this SRPA, and despite the wave spectra being available beyond 0.13 Hz, the power extracted by the SRPA cannot be computed in that region. If the power extracted could be computed in full, it would serve to shift the peak to the right.

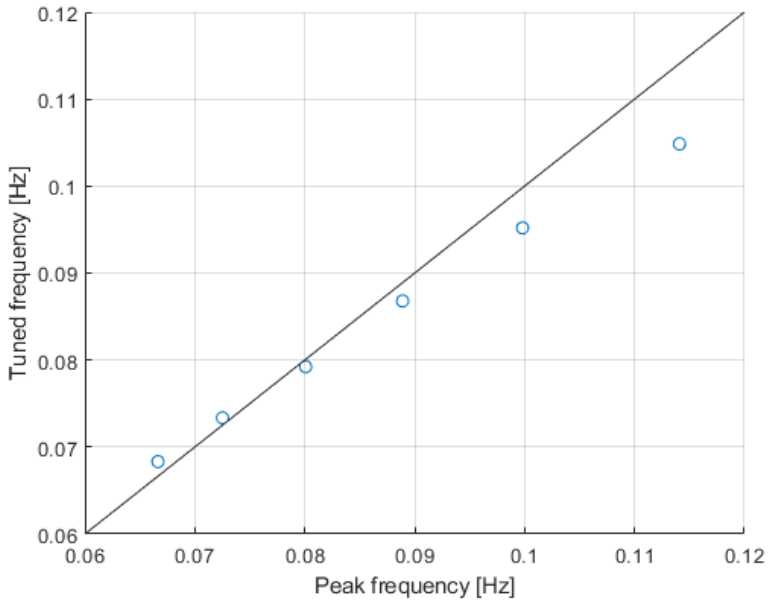

Figure 5-10 Comparison of optimal tuned frequency to peak frequency of PM spectra.

A rule for determining the optimal frequency for GA control with the SSB approach is made clearer by plotting the tuned frequencies which yielded the most total power against the peak frequencies of each of the PM spectra. Note that although twenty spectra were studied, many shared peak frequencies due to having been binned as shown in Figure 3-4, resulting in six unique peak frequencies. Figure 5-10 demonstrates that the best tuned frequencies tend to match the peak frequencies of the spectra, but tended to be lower for higher frequencies. This tendency is

explained by the truncation of spectral data as shown in Figure 5-9 where the optimal frequency is artificially shifted down.

From these results, one can conclude that the optimal setpoint frequency for the SRPA controllers is very near the peak frequency of a PM. Fortunately, this result is somewhat intuitive as well – to maximize power the SRPA should be tuned to or near the wave frequency with the largest amplitude, and therefore most energy. Since the sea states at the selected site tend to have single peaks with much of the energy clustered around the peak frequency, this is the optimal frequency to use for the SSB control approach and GA control.

5.4 Average Annual Useful Power

The useful power and energy from each sea state at the Nootka Island site may be computed with the SSB control approach for optimizing the power from a PM spectrum to estimate annual performance. This estimate provides a visual comparison of how much power the SRPA produces in each sea state. Combining that annual estimate of power with the number of hours each sea state occurs also demonstrates where the most energy is captured. Figure 5-11, Figure 5-12, and Figure 5-13 all use the same scale for comparison of the three control types studied.

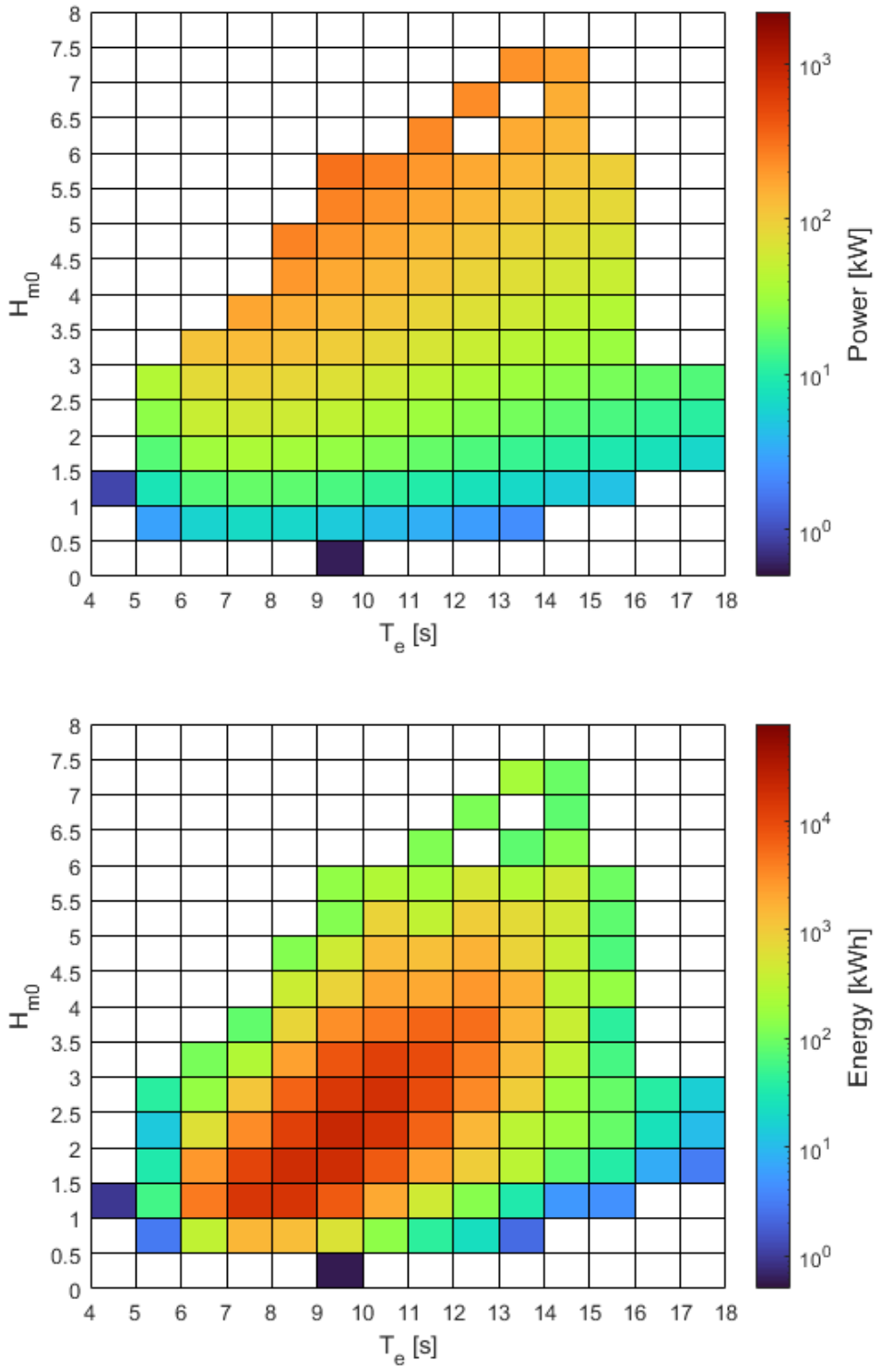

Figure 5-11 Power (top) and energy (bottom) of SRPA with AM control near Nootka Island.

The power plot in Figure 5-11 shows that more power is found for higher wave heights and lower periods. However, some of this is primarily a property of the sea state rather than the control of the device. The power in each sea state P_{PM} is typically estimated in deep water as:

$$P_{PM} = \frac{\rho_w g^2}{64\pi} H_{m0}^2 T_e \tag{5.5}$$

So, as significant wave height increases, energy increases with its square. Interestingly, power in the waves increases linearly with the energy period, but the SRPA under AM control extracts more power from lower periods. Beter performance at low periods where there is less power available indicates a mismatch between the most energetic resonance modes of the SRPA and the spectrum at this site.

The sea states which occur most often are near the bottom-middle of the plots as shown in Figure 5-2. Operating with AM control, the SRPA useful power is on the order of 10^1 kW in this region. Although power is much greater from higher wave height and lower period sea states, these occur less often, and contribute much less energy per year than sea states which occur for hundreds of hours each year. As such, the energy plot is dominated by the hourly occurrences of each sea state.

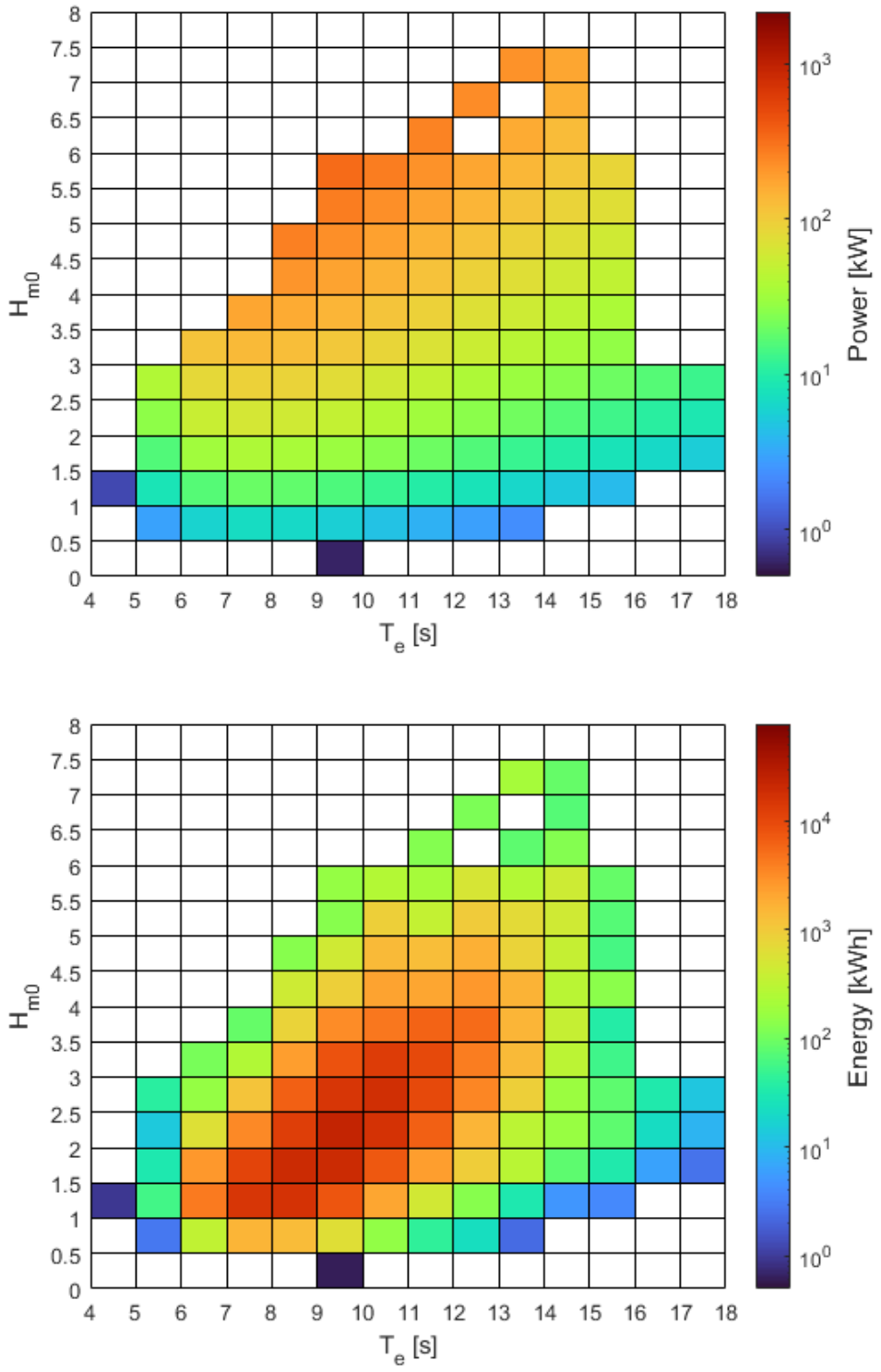

Figure 5-12 Power (top) and energy (bottom) of SRPA with CC control near Nootka Island.

Figure 5-12 demonstrates that CC control exhibits the same mismatch as AM control where the SRPA performs best and where the energy in the spectrum is. Although the controller can bring the SRPA into resonance by cancelling the imaginary component of the intrinsic impedance at the peak frequency, the power produced by that resonant condition is not much greater than that of AM control as was shown in Figure 4-4. That small power improvement is further undercut by the attenuating effect of SSB control, so gains are only seen for a small frequency band around the peak frequency.

Comparing Figure 5-12 directly to Figure 5-11 confirms that there is almost no difference in terms of power or energy between CC and AM control. With the colour scale the difference is imperceptible, but CC control does result in slightly more power and energy overall. Notably, the power in the critical sea states which occur most often is still on the order of 10^1 kW.

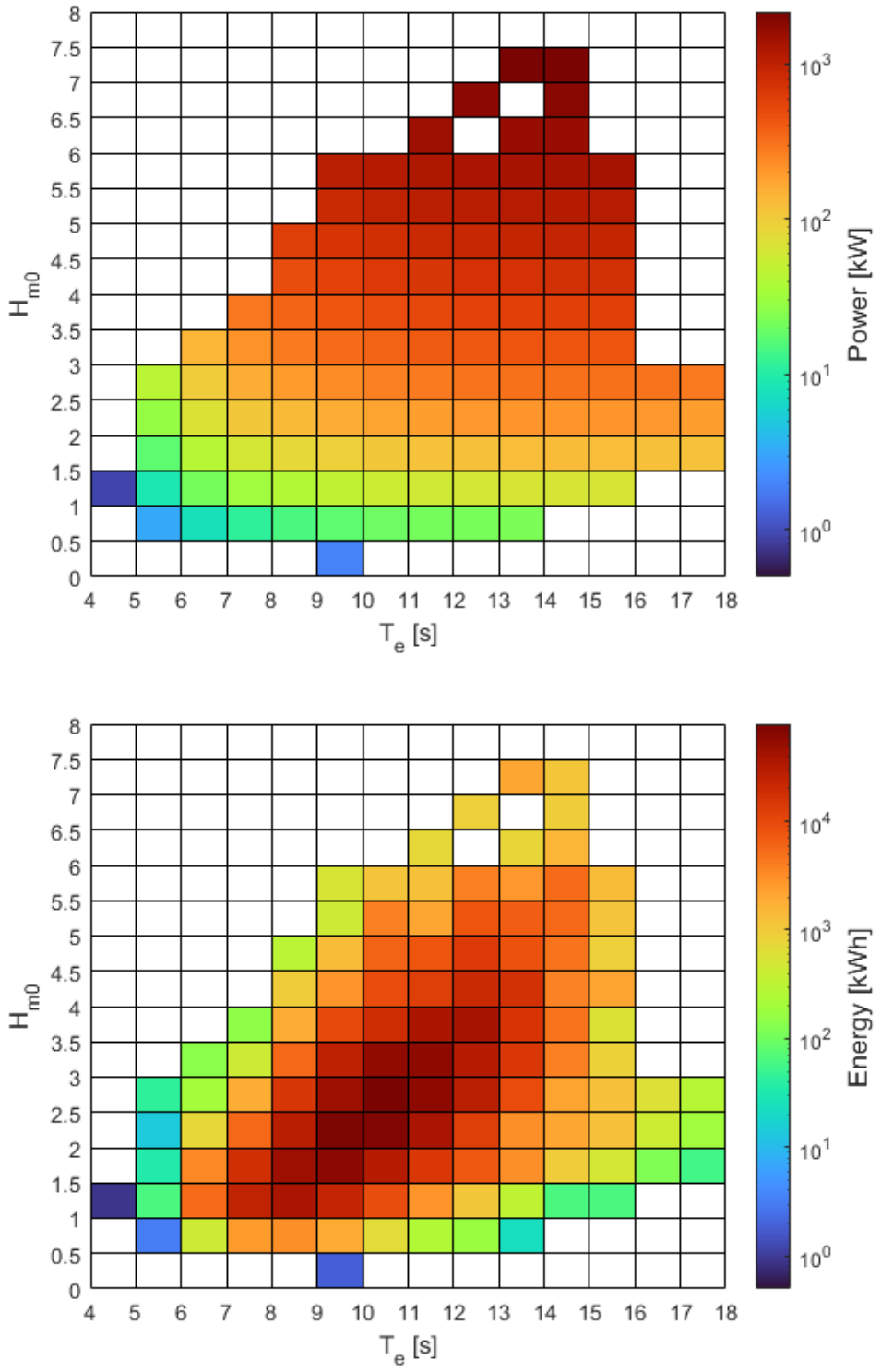

Figure 5-13 Power (top) and energy (bottom) of SRPA with GA control near Nootka Island.

Figure 5-13 shows the power and energy produced by a moored SRPA operating under GA control. Both power and energy are noticeably improved from AM and CC control. More power is produced by larger waves, but the dependence on period has been reversed, and the SRPA now tends to generate more power from spectra with higher energy periods. This tendency serves to generate much more energy in the top-right region and has the effect of expanding the cluster of sea-states which produce the most energy to higher periods and wave heights despite fewer occurrences. The power and energy are similar to AM and CC control for the lowest significant wave heights and energy periods, but in the central region which occurs most often the power is roughly four times higher.

The performance of each control method can be expressed in terms of its Annual Energy Production (AEP), which is simply the sum of the energy from each sea-state. The same can be done with the mooring present but not accounted for in the controller as was done in case 2 in Chapter 4 for comparison with those results. As a reminder, case 2 includes the mooring in dynamic calculations, but not in the setting of the controller and simulates adding the mooring at the end of the design process, while case 3 simulates including the mooring in the early design and designing the controller with that knowledge.

Table 6 Simulated annual energy production of moored WaveBob SRPA operating under three control types with and without knowledge of the mooring.

	Case 2	Case 3
AM	306 MWh	306 MWh
CC	313 MWh	320 MWh
GA	1241 MWh	1261 MWh

The differences between case 2 and case 3 are largely negligible, amounting to a maximum of 2.2% difference for CC control. This small difference is reflective of the negligible difference seen between case 2 and case 3 in Figure 4-5, Figure 4-6, and Figure 4-7 for the catenary mooring.

As established in Section 4.3.2, in the case of the catenary mooring, knowledge of the mooring dynamics did not appreciably change the power RAO. However, other mooring designs would have a greater impact as indicated in Figure 4-8, Figure 4-9, and Figure 4-10.

The gain from CC control is appreciable at this scale but is insignificant compared to the increase in AEP provided by GA control, which provides roughly four times more energy than the other control types which directly impacts the LCOE of the SRPA. It should be noted that although four times more energy is a massive leap forward, it does not necessarily make this SRPA cost-competitive with conventional renewables. Further work including a detailed analysis of the lifetime of the device; as well as the development, operation, and decommissioning costs would be required to calculate the LCOE for comparison with other energy sources. However, this work builds confidence in the inerter technology by demonstrating that GA control is advantageous in a polychromatic sea and is not undercut by the mooring.

Chapter 6

Conclusions and Future Work

The objectives of this work were to present a method for characterizing a mooring to be used in the linear circuit model of a Self-Reacting Point Absorber (SRPA); to determine if including that characterized mooring in the circuit model significantly impacted the control or power production of the SRPA; and to assess if the mooring or operation in a polychromatic sea erodes the increase in power production from changing resonant modes previously seen with geometry control.

An intuitive characterization method stemming from Fourier analysis has been presented and its merits and limitations have briefly been compared with other approaches. This approach in combination with the mechanical circuit framework also led to a multi-block mooring model which sheds light on how the complicated physical phenomena of a mooring may be manifested as a circuit model.

Including a mooring model in the frequency domain SRPA model was shown to have a varied impact depending on the design of the mooring system and control type used. Adding any of the four mooring systems studied to an SRPA was shown to reduce the useful power captured to as low as 10% of the original power in the worst case. However, some of the lost power could be brought back by including the mooring model in the design of the controller. The moorings which reduced the useful power the most could also be recouped the most by accounting for their

impedance in the controllers. Geometry and amplitude control was shown to be the most effective control type with the mooring present.

Finally, frequency domain simulations of a moored SRPA in polychromatic conditions demonstrated the efficacy of geometry and amplitude control over complex-conjugate and plain amplitude control. A heuristic for the sub-optimal control of an SRPA in wave spectra is presented and used to evaluate the annual energy production of the moored SRPA at a site off the West Coast of Canada. The annual energy production of the moored SRPA operating with geometry and amplitude control was calculated to be 788 GWh per year, which was four times more than for complex-conjugate or amplitude control.

Avenues for future work centre around improving the model fidelity of the SRPA in increments. Working in measured increments serves to increase the performance of SRPAs before major design decisions are made. Additionally, an incremental approach serves to build understanding of the effects of other systems and system interactions by not changing too many variables at once. Applying this approach should lead to diagnosing any physical phenomena or logistical constraints which limit or detract of the potential of this class of WEC. If researchers can pin down an element, constraint, or phenomenon which causes performance drops, such issues may begin to be addressed.

One step forward could be made be investigating the effects of including more than one degree of freedom (DOF) motion for the SRPA as well as the mooring. Adding pitch and surge would be an appropriate intermediate step before full 6DOF modelling and simulation and could both make use of the linear circuit approach.

With the relationship between the mooring system and the reactive force source of master-follower control exposed, some study into designing a mooring which better assist the control effort may be prudent. Such a study could be completed with different mooring configurations or perhaps connecting the mooring to the float rather than the spar. The tools presented in this work should help facilitate that research.

Also regarding design revisions, some attention should be directed to the lazy-S mooring design which was difficult to characterize with much accuracy due to snap loads. Such loads could be further damped by widening the U-shaped section to create more perpendicular drag or by reducing the weight of the depressor mass. There may also be some commonality in the concepts of what response is desirable for a mooring designer and what response can be characterized with a linear model which would be intriguing to pursue.

The physical design of the reactive force to achieve the desired control also warrants further investigation. As presented, the reactive force source includes a reaction mass, reaction spring, and inerter which may all be adjusted to achieve the desired control profile. The inerter was treated as a controllable element with an effective mass which was a function of the control profile and choice of reaction mass and spring stiffness. Computing the effective mass of the inerter revealed it to have a negative value for a range of frequencies. Negative mass is physically unattainable, so it follows that the actual control could not be achieved in this range. A future study could investigate the effect of changing the reaction mass and spring stiffness to limit that range as well as to quantify the impacts of not achieving the optimal control effort in that range.

Finally, time domain modelling of the 1DOF and eventually 6DOF system should also be pursued in future work. Many of the assumptions made in this work could be checked by forming

time domain response amplitude operators of the frequency dependent forces and comparing the resulting time domain model with simulations. Demonstrating competitive advantage at the time domain level would be a significant step in the development of master-follower control of SRPAs.

References

[1] R. Haas, C. Kemfert, H. Auer, A. Ajanovic, M. Sayer, and A. Hiesl, “On the economics of storage for electricity: Current state and future market design prospects,” *WIREs Energy Environ.*, vol. 11, no. 3, p. e431, 2022, doi: 10.1002/wene.431.

[2] J. Widén *et al.*, “Variability assessment and forecasting of renewables: A review for solar, wind, wave and tidal resources,” *Renew. Sustain. Energy Rev.*, vol. 44, pp. 356–375, Apr. 2015, doi: 10.1016/j.rser.2014.12.019.

[3] S. C. Parkinson, K. Dragoon, G. Reikard, G. García-Medina, H. T. Özkan-Haller, and T. K. A. Brekken, “Integrating ocean wave energy at large-scales: A study of the US Pacific Northwest,” *Renew. Energy*, vol. 76, pp. 551–559, Apr. 2015, doi: 10.1016/j.renene.2014.11.038.

[4] H. Bailey, B. Robertson, and B. Buckham, “Variability and stochastic simulation of power from wave energy converter arrays,” *Renew. Energy*, vol. 115, pp. 721–733, Jan. 2018, doi: 10.1016/j.renene.2017.08.052.

[5] G. Mork, S. Barstow, A. Kabuth, and M. T. Pontes, “Assessing the Global Wave Energy Potential,” *Proc. Int. Conf. Offshore Mech. Arct. Eng. - OMAE*, vol. 3, pp. 447–454, Dec. 2010, doi: 10.1115/OMAE2010-20473.

[6] C. E. R. Government of Canada, “CER – Provincial and Territorial Energy Profiles – British Columbia.” Accessed: Oct. 12, 2023. [Online]. Available: https://www.cer-rec.gc.ca/en/data-analysis/energy-markets/provincial-territorial-energy-profiles/provincial-territorial-energy-profiles-british-columbia.html

[7] B. Robertson, C. Hiles, E. Luczko, and B. Buckham, “Quantifying wave power and wave energy converter array production potential,” *Int. J. Mar. Energy*, vol. 14, pp. 143–160, Jun. 2016, doi: 10.1016/j.ijome.2015.10.001.

[8] X. Xu, B. Robertson, and B. Buckham, “A techno-economic approach to wave energy resource assessment and development site identification,” *Appl. Energy*, vol. 260, p. 114317, Feb. 2020, doi: 10.1016/j.apenergy.2019.114317.

[9] A. Pecher and J. P. Kofoed, *Handbook of Ocean Wave Energy*. 2017. [Online]. Available: https://books.google.com/books?id=IuTxjwEACAAJ

[10] “CETO Technology,” Carnegie. Accessed: Nov. 11, 2023. [Online]. Available: https://www.carnegiece.com/ceto-technology/

[11] “Wave Energy Technology – CorPower Ocean.” Accessed: Nov. 11, 2023. [Online]. Available: https://corpowerocean.com/wave-energy-technology/

[12] boundarycreative.co.uk, “PB3 PowerBuoy,” Ocean Power Technologies. Accessed: Mar. 08, 2024. [Online]. Available: https://oceanpowertechnologies.com/platform/opt-pb3-powerbuoy/

[13] K. Bubbar and B. Buckham, “On establishing generalized analytical phase control conditions in two body self-reacting point absorber wave energy converters,” *Ocean Eng.*, vol. 197, p. 106879, Feb. 2020, doi: 10.1016/j.oceaneng.2019.106879.

[14] J. Weber, F. Mouwen, A. Parish, and D. Robertson, “Wavebob – Research & Development Network and Tools in the Context of Systems Engineering,” presented at the 8th European Wave and Tidal Energy Conference (EWTEC 2009), Uppsala, Sweden, 2009.

[15] “Reference Model Project (RMP) : Sandia Energy.” Accessed: Nov. 11, 2023. [Online]. Available: https://energy.sandia.gov/programs/renewable-energy/water-power/projects/reference-model-project-rmp/

[16] S. J. Beatty, B. Bocking, K. Bubbar, B. J. Buckham, and P. Wild, “Experimental and numerical comparisons of self-reacting point absorber wave energy converters in irregular waves,” *Ocean Eng.*, vol. 173, pp. 716–731, Feb. 2019, doi: 10.1016/j.oceaneng.2019.01.034.

[17] “Hydropower LCOE worldwide 2021,” Statista. Accessed: Oct. 13, 2023. [Online]. Available: https://www.statista.com/statistics/799349/lcoe-of-hydropower-worldwide/

[18] E. Baca, R. Philip, D. Greene, and H. Battey, “Expert Elicitation for Wave Energy LCOE Futures,” NREL/TP-5700-82375, 1885577, MainId:83148, Aug. 2022. doi: 10.2172/1885577.

[19] A. Babarit, *Ocean Wave Energy Conversion: Resource, Technologies and Performance*. Elsevier, 2017.

[20] J. Weber, “WEC Technology Readiness and Performance Matrix – finding the best research technology development trajectory,” presented at the 7th European Wave and Tidal Energy Conference, Oct. 2012.

[21] B. Robertson, J. Bekker, and B. Buckham, “Renewable integration for remote communities: Comparative allowable cost analyses for hydro, solar and wave energy,” *Appl. Energy*, vol. 264, p. 114677, Apr. 2020, doi: 10.1016/j.apenergy.2020.114677.

[22] K. Budal and J. Falnes, “Optimum operation of improved wave-power converter,” *Mar Sci Commun U. S.*, vol. 3:2, Jan. 1977, Accessed: Oct. 11, 2023. [Online]. Available: https://www.osti.gov/biblio/7213955

[23] P. Nebel, “Maximizing the Efficiency of Wave-Energy Plant Using Complex-Conjugate Control,” *Proc. Inst. Mech. Eng. Part J. Syst. Control Eng.*, vol. 206, no. 4, pp. 225–236, Nov. 1992, doi: 10.1243/PIME_PROC_1992_206_338_02.

[24] A. A. E. Price, C. J. Dent, and A. R. Wallace, “On the capture width of wave energy converters,” *Appl. Ocean Res.*, vol. 31, no. 4, pp. 251–259, 2009, doi: 10.1016/J.APOR.2010.04.001.

[25] L. Wang and J. V. Ringwood, “Control-informed ballast and geometric optimisation of a three-body hinge-barge wave energy converter using two-layer optimisation,” *Renew. Energy*, vol. 171, pp. 1159–1170, Jun. 2021, doi: 10.1016/j.renene.2021.02.125.

[26] K. Bubbar and B. Buckham, “On establishing an analytical power capture limit for self-reacting point absorber wave energy converters based on dynamic response,” *Appl. Energy*, vol. 228, no. October, pp. 324–338, 2018, doi: 10.1016/j.apenergy.2018.06.099.

[27] M. Folley, *Numerical Modelling of Wave Energy Converters*. 2016. doi: 10.1016/c2014-0-04006-3.

[28] Y. Liu and L. Bergdahl, “Frequency-domain dynamic analysis of cables,” *Eng. Struct.*, vol. 19, no. 6, pp. 499–506, Jun. 1997, doi: 10.1016/S0141-0296(96)00091-0.

[29] J. Fitzgerald and L. Bergdahl, “Including moorings in the assessment of a generic offshore wave energy converter: A frequency domain approach,” *Mar. Struct.*, vol. 21, no. 1, pp. 23–46, Jan. 2008, doi: 10.1016/j.marstruc.2007.09.004.

[30] J. Davidson and J. V. Ringwood, “Mathematical Modelling of Mooring Systems for Wave Energy Converters—A Review,” *Energies*, vol. 10, no. 5, Art. no. 5, May 2017, doi: 10.3390/en10050666.

[31] F. Cerveira, N. Fonseca, and R. Pascoal, “Mooring system influence on the efficiency of wave energy converters,” *Int. J. Mar. Energy*, vol. 3–4, pp. 65–81, Dec. 2013, doi: 10.1016/j.ijome.2013.11.006.

[32] M. Jaya Muliawan, Z. Gao, T. Moan, and A. Babarit, “Analysis of a Two-Body Floating Wave Energy Converter With Particular Focus on the Effects of Power Take-Off and Mooring Systems on Energy Capture,” *J. Offshore Mech. Arct. Eng.*, vol. 135, no. 3, May 2013, doi: 10.1115/1.4023796.

[33] M. C. Smith, “Synthesis of mechanical networks: the inerter,” *IEEE Trans. Autom. Control*, vol. 47, no. 10, pp. 1648–1662, Oct. 2002, doi: 10.1109/TAC.2002.803532.

[34] S. Beatty, “Analysis and development of a three body heaving wave energy converter,” Thesis, 2009. Accessed: Nov. 11, 2023. [Online]. Available: https://dspace.library.uvic.ca/handle/1828/1401

[35] J. Falnes, “Wave-Energy Conversion Through Relative Motion Between Two Single-Mode Oscillating Bodies,” *J. Offshore Mech. Arct. Eng.*, vol. 121, no. 1, pp. 32–38, Feb. 1999, doi: 10.1115/1.2829552.

[36] K. Bubbar, B. Buckham, and P. Wild, “A method for comparing wave energy converter conceptual designs based on potential power capture,” *Renew. Energy*, vol. 115, no. September, pp. 797–807, 2018, doi: 10.1016/j.renene.2017.09.005.

[37] J. P. Ortiz, “The influence of mooring dynamics on the performance of self reacting point absorbers,” Thesis, 2016. Accessed: Apr. 17, 2022. [Online]. Available: https://dspace.library.uvic.ca/handle/1828/7339

[38] J. Falnes and A. Kurniawan, *Ocean Waves and Oscillating Systems: Linear Interactions Including Wave-Energy Extraction*, 2nd ed. Cambridge University Press, 2020. doi: 10.1017/9781108674812.

[39] C. M. Harris, C. E. Crede, and H. M. Trent, *Shock and Vibration Handbook*, vol. 15. Physics Today, 1962. Accessed: Dec. 09, 2023. [Online]. Available: https://doi.org/10.1063/1.3058391

[40] S. J. Beatty, M. Hall, B. J. Buckham, P. Wild, and B. Bocking, "Experimental and numerical comparisons of self-reacting point absorber wave energy converters in regular waves," *Ocean Eng.*, vol. 104, pp. 370–386, Aug. 2015, doi: 10.1016/j.oceaneng.2015.05.027.

[41] S. J. Beatty, "Scaling a Wave Energy Converter: from Theory to Application".

[42] S. K. Chakrabarti, "Modelling Laws in Ocean Engineering," in *Developments in Offshore Engineering: Wave Phenomena and Offshore Topics - 1st Edition*, Gulf Professional Publishing, 1999, pp. 295–335.

[43] E. Gubesch, N. Abdussamie, I. Penesis, and C. Chin, "Effects of mooring configurations on the hydrodynamic performance of a floating offshore oscillating water column wave energy converter," *Renew. Sustain. Energy Rev.*, vol. 166, p. 112643, Sep. 2022, doi: 10.1016/j.rser.2022.112643.

[44] S.-H. Yang, J. W. Ringsberg, E. Johnson, and Z. Hu, "Experimental and numerical investigation of a taut-moored wave energy converter: a validation of simulated mooring line forces," *Ships Offshore Struct.*, vol. 15, no. sup1, pp. S55–S69, Dec. 2020, doi: 10.1080/17445302.2020.1772667.

[45] "ProteusDS | A flexible Dynamic Analysis Tool for Ocean Industries | DSA," DSA Ocean. Accessed: Apr. 07, 2022. [Online]. Available: https://dsaocean.com/proteusds/overview/

[46] J. T. Scruggs, S. M. Lattanzio, A. A. Taflanidis, and I. L. Cassidy, “Optimal causal control of a wave energy converter in a random sea,” *Appl. Ocean Res.*, vol. 42, pp. 1–15, Aug. 2013, doi: 10.1016/j.apor.2013.03.004.

[47] B. Paduano, E. Pasta, N. Faedo, and G. Mattiazzo, “Control synthesis via Impedance-Matching in panchromatic conditions: a generalised framework for moored systems,” in *Proceedings of the European Wave and Tidal Energy Conference*, Sep. 2023. doi: 10.36688/ewtec-2023-344.

[48] Robertson, Bryson, Eley, Aaron, I. Beya, and Buckham, Bradley, “Mowachaht Muchalaht Resource Assessment,” PRIMED, Resource Assessment, Aug. 2018. [Online]. Available: https://onlineacademiccommunity.uvic.ca/primed/

[49] S. Ahn, “Modeling mean relation between peak period and energy period of ocean surface wave systems,” *Ocean Eng.*, vol. 228, p. 108937, May 2021, doi: 10.1016/j.oceaneng.2021.108937.

[50] W. J. Pierson Jr. and L. Moskowitz, “A proposed spectral form for fully developed wind seas based on the similarity theory of S. A. Kitaigorodskii,” *J. Geophys. Res. 1896-1977*, vol. 69, no. 24, pp. 5181–5190, 1964, doi: 10.1029/JZ069i024p05181.

[51] L. H. Holthuijsen, *Waves in Oceanic and Coastal Waters*. Cambridge University Press, 2007.

[52] X. Jiang, D. Gao, F. Hua, Y. Yang, and Z. Wang, “An Improved Approach to Wave Energy Resource Characterization for Sea States with Multiple Wave Systems,” *J. Mar. Sci. Eng.*, vol. 10, no. 10, Art. no. 10, Oct. 2022, doi: 10.3390/jmse10101362.

[53] B. Robertson, H. Bailey, D. Clancy, J. Ortiz, and B. Buckham, “Influence of Wave Resource Assessment Methods on Wave Power Production Estimates,” in *Influence of wave resource assessment methods on wave power production estimates.*, Halifax, Canada, 2014.

[54] “Transfer Function Stability - Interesting Facts about Polynomial Form.” Accessed: Oct. 22, 2023. [Online]. Available: https://controlsystemsacademy.com/0012/0012.html

[55] A. Ilchmann and F. Wirth, “On Minimum Phase,” – *Autom.*, vol. 61, no. 12, pp. 805–817, Dec. 2013, doi: 10.1524/auto.2013.1002.

[56] J.-C. Gilloteaux and J. Ringwood, “Control-informed geometric optimisation of wave energy converters,” *IFAC Proc. Vol.*, vol. 43, no. 20, pp. 366–371, Sep. 2010, doi: 10.3182/20100915-3-DE-3008.00072.

[57] G. Bacelli and R. G. Coe, “Comments on Control of Wave Energy Converters,” *IEEE Trans. Control Syst. Technol.*, vol. 29, no. 1, pp. 478–481, Jan. 2021, doi: 10.1109/TCST.2020.2965916.

[58] N. Faedo, G. Scarciotti, A. Astolfi, and J. V. Ringwood, “Energy-maximising control of wave energy converters using a moment-domain representation,” *Control Eng. Pract.*, vol. 81, pp. 85–96, Dec. 2018, doi: 10.1016/j.conengprac.2018.08.010.

[59] N. Faedo, Y. Peña-Sanchez, and J. V. Ringwood, “Receding-Horizon Energy-Maximising Optimal Control of Wave Energy Systems Based on Moments,” *IEEE Trans. Sustain. Energy*, vol. 12, no. 1, pp. 378–386, Jan. 2021, doi: 10.1109/TSTE.2020.3000013.

[60] E. Anderlini, S. Husain, G. G. Parker, M. Abusara, and G. Thomas, “Towards Real-Time Reinforcement Learning Control of a Wave Energy Converter,” *J. Mar. Sci. Eng.*, vol. 8, no. 11, Art. no. 11, Nov. 2020, doi: 10.3390/jmse8110845.

[61] P. Scherz and S. Monk, “Superposition Theorem,” in *Practical Electronics for Inventors*, McGraw-Hill Education, 2016, p. Chap 2.18.

Appendix A – WaveBob SRPA Dimensions

This appendix contains sketches of the float and spar used in this work. All dimensions are in metres.

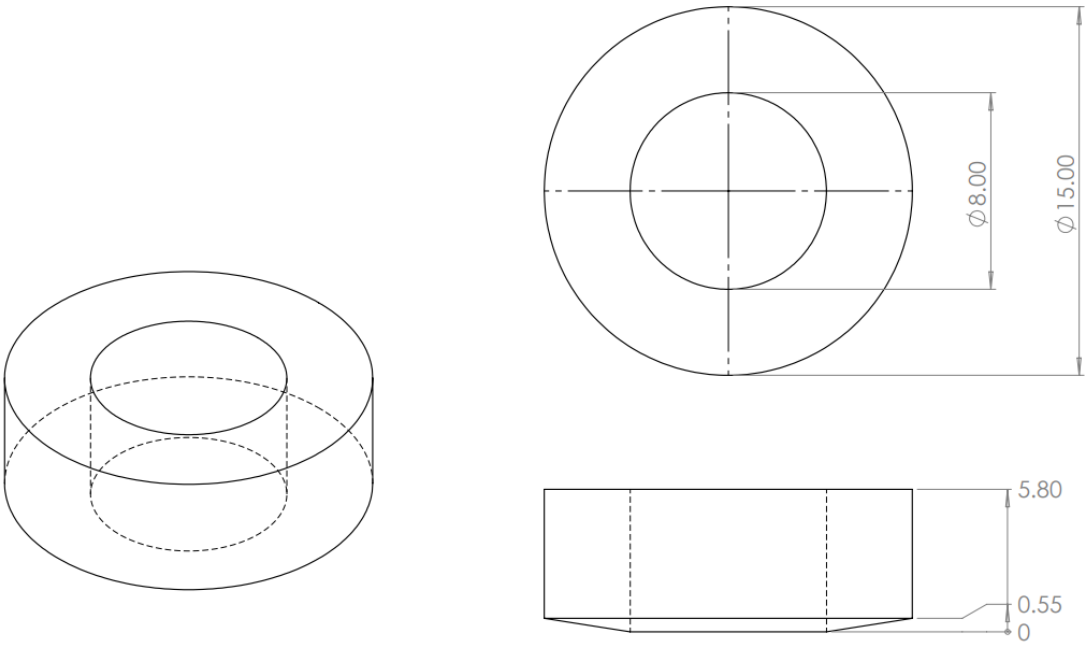

Figure A-1 Drawing of the float. All dimensions are in metres.

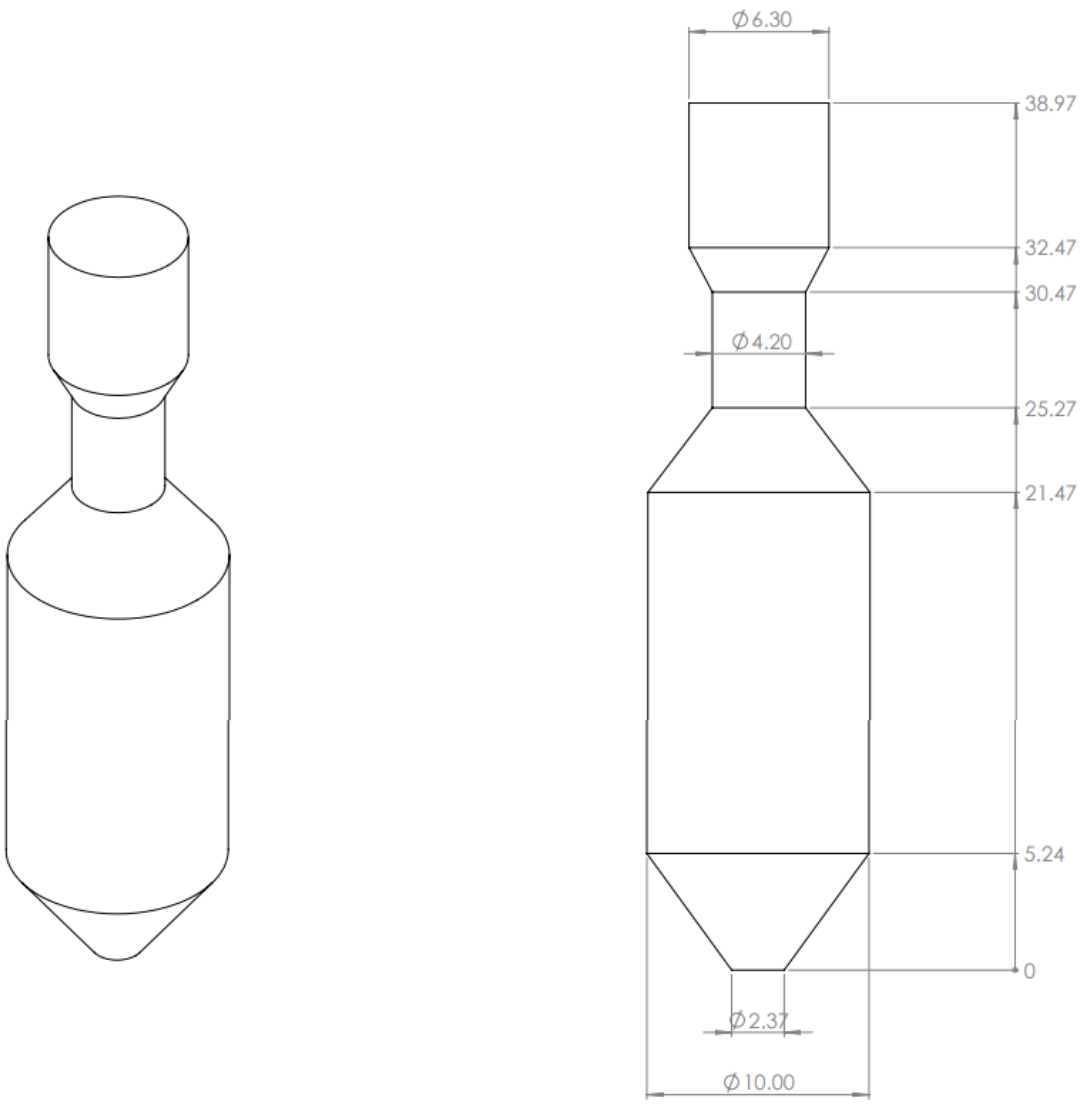

Figure A-2 Drawing of the spar. All dimensions are in metres.

Appendix B – Mooring Initialization Data

The following data describes the parameters of the mooring line segments and weights used in ProteusDS simulations. It may be imported for future simulations as part of the library files. The sections on each mooring describe the initial state of each mooring node and segment. They also include the lengths, segment types, and positions of weights and floats used for each design.

<Cable_n1 type="DCableSegment">
// Fluid loading
$CDc 2.4
$CDt 0.01
$CAc 1
// Mechanical
$EA 1.05e6
$EI1 0
$EI2 0
$GJ 0
$Diameter 0.082606
 $Density 7700
$CID 47680.7465
$BCID 0
$TCID 0
$CE 0
</Cable_n1>

<Cable_n2 type="DCableSegment">
// Fluid loading
$CDc 1.5
$CDt 0.01
$CAc 1
// Mechanical
$EA 1.05e6
$EI1 0
$EI2 0
$GJ 0
$Diameter 0.08
 $Density 7700
$CID 226396.1726
$BCID 0
$TCID 0
$CE 0

```
</Cable_n2>

<Cable_n3 type="DCableSegment">
// Fluid loading
$CDc 1.5
$CDt 0.01
$CAc 1
// Mechanical
$EA 1.05e6
$EI1 0
$EI2 0
$GJ 0
$Diameter 0.08
 $Density 7700
$CID 149328.298
$BCID 0
$TCID 0
$CE 0
</Cable_n3>

<Dyneema_rope_104mm type="DCableSegment">
//Library Version 1.0
//Source: Samson Rope Catalogue
//Type: Amsteel Blue
//Nominal Diameter (manufacturer) 0.104
//mass per unit length (assumed dry state) 6.730
//elongation at 30% break 0.96
//Minimum breaking strength (kg) 828000
//Fluid loading
$CDc 1.5
$CDt 0.045
$CAc 1.0

//Mechanical
$EA 2.54E+08
$EI1 171591.615
$EI2 171591.615
$GJ 171591.615
$Diameter 1.04E-01
$Density 792.2
$AxialDampingMode 1
$AxialReferenceDampingRatio 0.5
$BCID 0
$TCID 0
$CE 0
```

```
$BuoyancyDiameter 9.35E-02
$MBS 8122680
</Dyneema_rope_104mm>

<extMass type="ExtMass">
// Fluid loading
$CD 0.5
$CA 0.5
$FluidLoadingMode 1

// Mechanical
$Diameter 1.1
$Density 7700

// Type
$ExtMassType 0
</extMass>

<extMass2 type="ExtMass">
// Fluid loading
$CD 0.5
$CA 0.5
$FluidLoadingMode 1

// Mechanical
$Diameter 1
$Density 7700

// Type
$ExtMassType 0
</extMass2>

<extMass3 type="ExtMass">
$CD 0.5
$CA 0.5
$FluidLoadingMode 1

//Mechanical
$Diameter 2
$Density 400

//Type
$ExtMassType 0
</extMass>
```

Catenary Mooring

// Boundary constraints
$Node0Static 0
$NodeNStatic 1

// Fluid loading
$FluidLoadingMode 0

// Mechanical
$CableSegmentMode 1

<state>
0
4.8
0
0
0
12.93
0
16.7496910845948
0
0.013851576851076
0
25.8573826783787
0
31.1485229439596
0
0.0384360117144582
0
35.8388947457215
0
46.2386930182727
0
0.0560505796992856
0
40.6960366029659
0
62.1426614352241
0
0.0768625165527049
0
41.2524314656901

0
100.457793874223
0
0.064419592654366
0
40.5361206459004
0
138.756907303422
0
0.0326943156807098
0
40.3562325663561
0
171.93
0
0
0
40
0
</state>
<lengths>
17.18925
17.18925
15.7869
15.7869
35.31347
35.31347
35.31347
</lengths>
<segments>
Cable_n2
Cable_n2
Cable_n3
Cable_n3
Cable_n1
Cable_n1
Cable_n1
</segments>
<Metadata>

<CableStateGenerator version="1">
<NewData>False</NewData>
<GeometryType>Custom</GeometryType>
<Node0>4.8 0 12.93</Node0>
<NodeN>171.93 0 40</NodeN>

<StretchedLength>176.843486989626</StretchedLength>
<ReferenceFromNode0>True</ReferenceFromNode0>
<ZModeReferenceLockHeightNode0>True</ZModeReferenceLockHeightNode0>
<ZModeReferenceLockHeightNodeN>True</ZModeReferenceLockHeightNodeN>
<StretchedLengths>17.3920441687746 17.3920441687746 15.8546455731255 15.8546455731255 36.7833691686086 36.7833691686086 36.7833691686086</StretchedLengths>
</CableStateGenerator>

</Metadata>

Heavy Catenary Mooring

// Boundary constraints
$Node0Static 0
$NodeNStatic 1

// Fluid loading
$FluidLoadingMode 0

// Mechanical
$CableSegmentMode 1

$ExtMass extMass 10
$ExtMass extMass 20
$ExtMass extMass 30
$ExtMass extMass 40
$ExtMass extMass 50
$ExtMass extMass 60

<state>
0
4.8
0
0
0
12.93
0
16.7496910845948
0
0.013851576851076
0

25.8573826783787
0
31.1485229439596
0
0.0384360117144582
0
35.8388947457215
0
46.2386930182727
0
0.0560505796992856
0
40.6960366029659
0
62.1426614352241
0
0.0768625165527049
0
41.2524314656901
0
100.457793874223
0
0.064419592654366
0
40.5361206459004
0
138.756907303422
0
0.0326943156807098
0
40.3562325663561
0
171.93
0
0
0
40
0
</state>
<lengths>
17.18925
17.18925
15.7869
15.7869
35.31347

35.31347
35.31347
</lengths>
<segments>
Cable_n2
Cable_n2
Cable_n3
Cable_n3
Cable_n1
Cable_n1
Cable_n1
</segments>
<Metadata>

<CableStateGenerator version="1">
<NewData>False</NewData>
<GeometryType>Custom</GeometryType>
<Node0>4.8 0 12.93</Node0>
<NodeN>171.93 0 40</NodeN>
<StretchedLength>176.843486989626</StretchedLength>
<ReferenceFromNode0>True</ReferenceFromNode0>
<ZModeReferenceLockHeightNode0>True</ZModeReferenceLockHeightNode0>
<ZModeReferenceLockHeightNodeN>True</ZModeReferenceLockHeightNodeN>
<StretchedLengths>17.3920441687746 17.3920441687746 15.8546455731255 15.8546455731255 36.7833691686086 36.7833691686086 36.7833691686086</StretchedLengths>
</CableStateGenerator>

</Metadata>

Taut-leg Mooring

// Boundary constraints
$Node0Static 0
$NodeNStatic 1

// Fluid loading
$FluidLoadingMode 0

// Mechanical
$CableSegmentMode 1

<state>
0
4.80000019073486
0
0
0
12.9300003051758
0
10.6713673805705
0
0
0
20.554373941055
0
17.1005651399395
0
0
0
27.7135232017719
0
24.1509146794004
0
0
0
34.260055669724
0
31.8700008392334
0
0
0
40
0
</state>
<lengths>
9.5100911635806
9.5100911635806
9.5100911635806
9.5100911635806
</lengths>
<segments>
Cable_n2
Cable_n2
Cable_n2
Cable_n2
</segments>

<Metadata>

<CableStateGenerator version="1">
<NewData>False</NewData>
<GeometryType>Catenary</GeometryType>
<Node0>4.80000019073486 0 12.9300003051758</Node0>
<NodeN>31.8700008392334 0 40</NodeN>
<StretchedLength>38.5</StretchedLength>
<ReferenceFromNode0>True</ReferenceFromNode0>
<ZModeReferenceLockHeightNode0>True</ZModeReferenceLockHeightNode0>
<ZModeReferenceLockHeightNodeN>True</ZModeReferenceLockHeightNodeN>
<StretchedLengths>9.625 9.625 9.625 9.625</StretchedLengths>
</CableStateGenerator>

</Metadata>

Lazy-S Mooring

// Boundary constraints
$Node0Static 0
$NodeNStatic 1

// Fluid loading
$FluidLoadingMode 0

// Mechanical
$CableSegmentMode 1

$ExtMass extMass2 17
$ExtMass extMass3 34

<state>
0.000000e+00
4.800000e+00
0.000000e+00
0.000000e+00
0.000000e+00
1.293000e+01
-2.986276e-02
8.175288e+00
6.494804e-15
2.206212e-13

1.273173e-02
2.081282e+01
-5.470468e-02
1.342476e+01
1.722191e-14
5.190408e-13
3.288170e-02
2.707735e+01
-4.290974e-02
1.852634e+01
2.639221e-14
7.100354e-13
4.326382e-02
2.074800e+01
-2.907281e-02
2.353678e+01
2.404235e-14
7.889888e-13
5.414531e-02
1.406408e+01
-5.397905e-02
3.592271e+01
1.109521e-14
5.668486e-13
9.209606e-02
2.228672e+01
-4.557071e-02
4.772059e+01
2.168621e-15
3.121891e-13
8.021399e-02
3.272169e+01
-1.482860e-03
6.210604e+01
2.460193e-16
3.317451e-14
-1.233677e-03
4.032904e+01
2.145971e-04
7.842178e+01
5.444445e-18
-5.216702e-16
-3.587623e-05
4.041475e+01
0.000000e+00

9.480000e+01
0.000000e+00
0.000000e+00
0.000000e+00
4.000000e+01
0.000000e+00
</state>
<lengths>
8.594625e+00
8.594625e+00
8.594625e+00
8.594625e+00
1.578690e+01
1.578690e+01
1.636564e+01
1.636564e+01
1.636564e+01
</lengths>
<segments>
Dyneema_rope_104mm
Dyneema_rope_104mm
Dyneema_rope_104mm
Dyneema_rope_104mm
Dyneema_rope_104mm
Dyneema_rope_104mm
Cable_n1
Cable_n1
Cable_n1
</segments>

Appendix C – SID Pole-Zero Plots

The following plots show the pole-zero plots of the transfer functions found and used to model each mooring. The highlight that the mooring models are all stable with poles (x's) all being negative-real. They also show that all the designs except the lazy-S mooring are minimum-phase with the zeros (o's) also being negative-real.

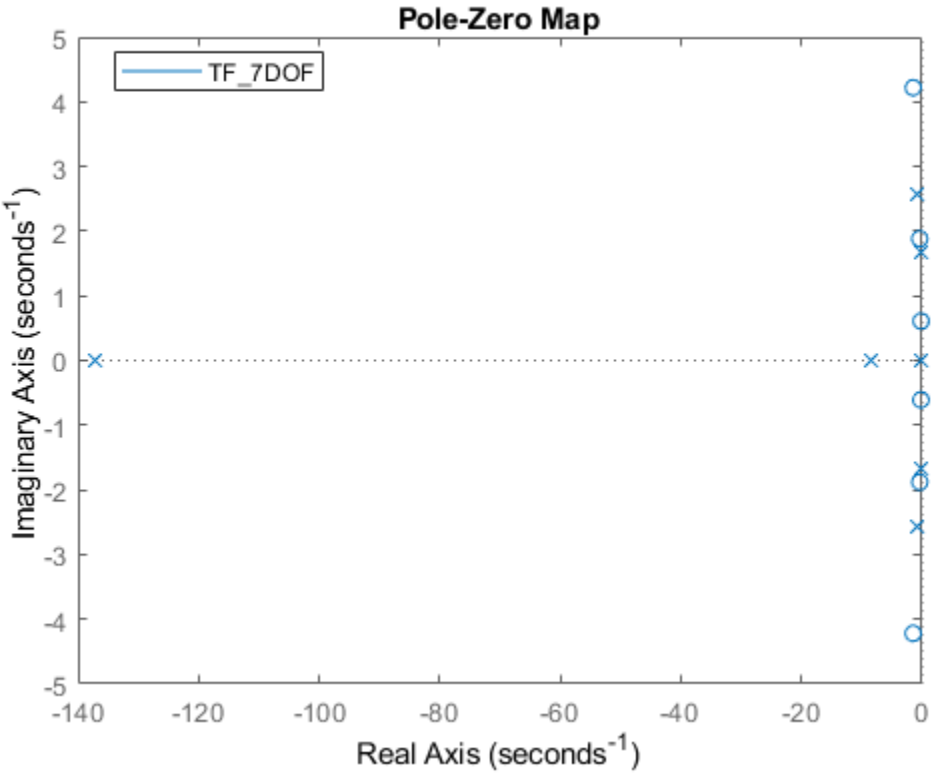

Figure C-1 Pole-zero plot of catenary transfer function fit.

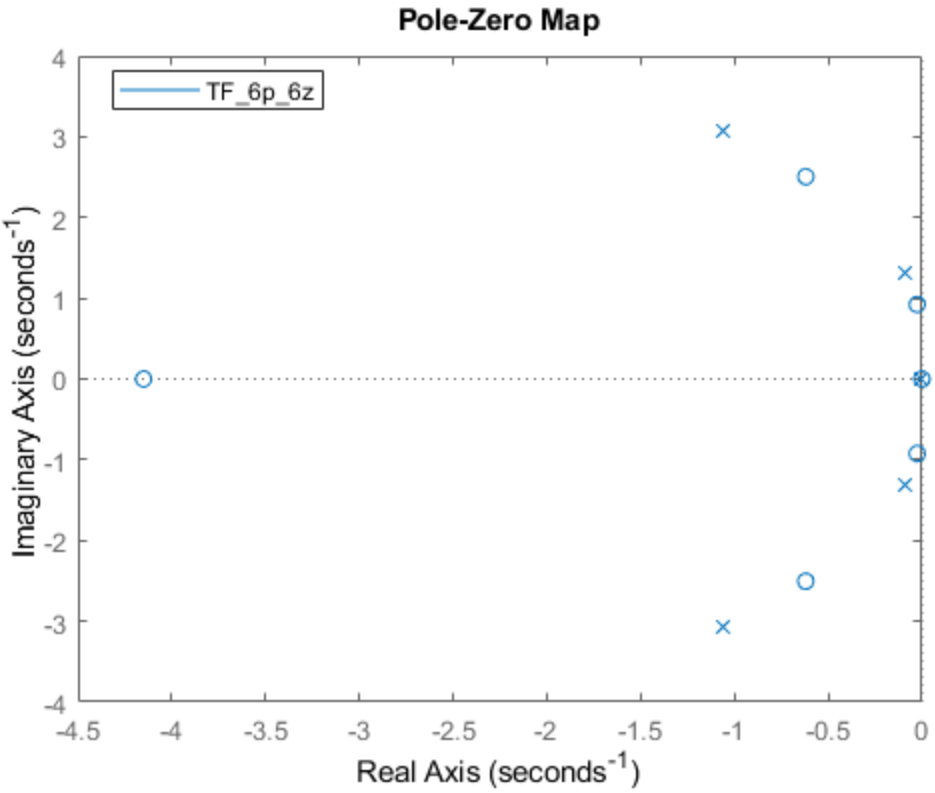

Figure C-2 Pole-zero plot of heavy catenary transfer function fit.

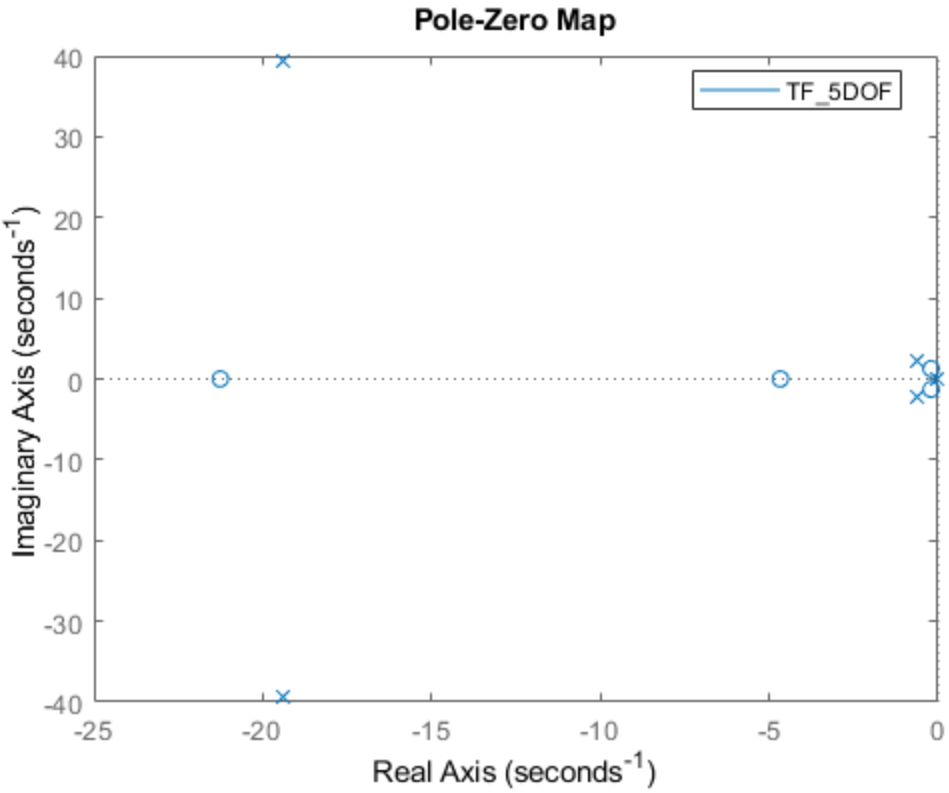

Figure C-3 Pole-zero plot of taut-leg transfer function fit.

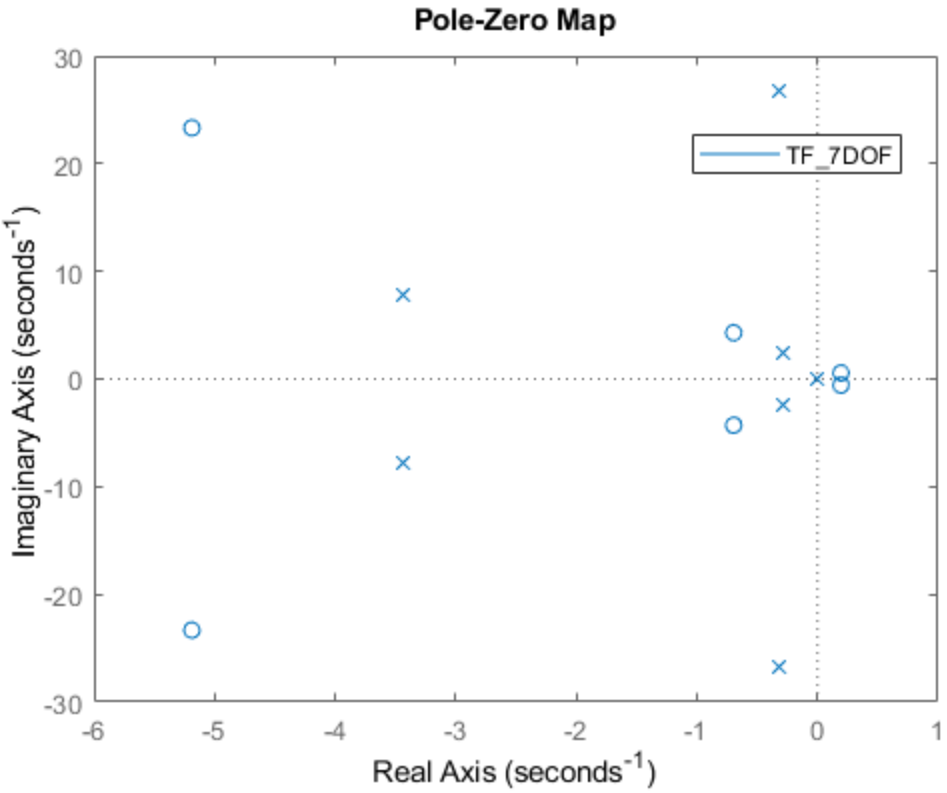

Figure C-4 Pole-zero plot of lazy-S transfer function fit.

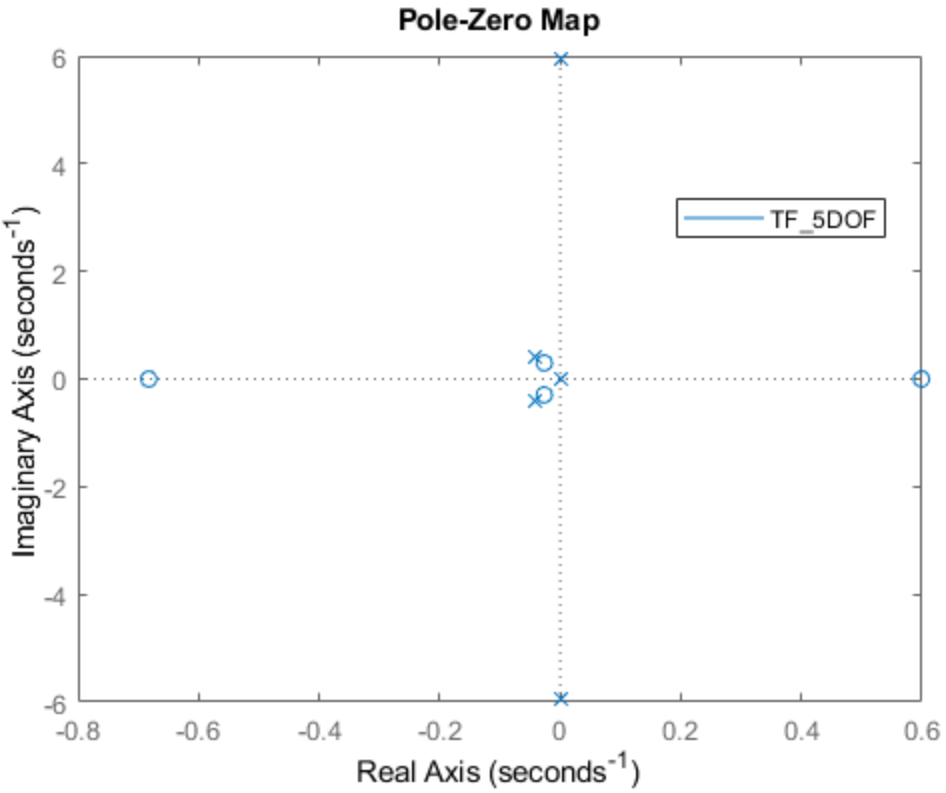

Figure C-5 Pole-zero plot of lazy-S transfer function fit over smaller frequency range.

Appendix D – Average Power in PM Spectra

This appendix contains plots of the power generated by the SRPA in the twenty most energetic PM spectra at Nootka Island when tuned to various frequencies.

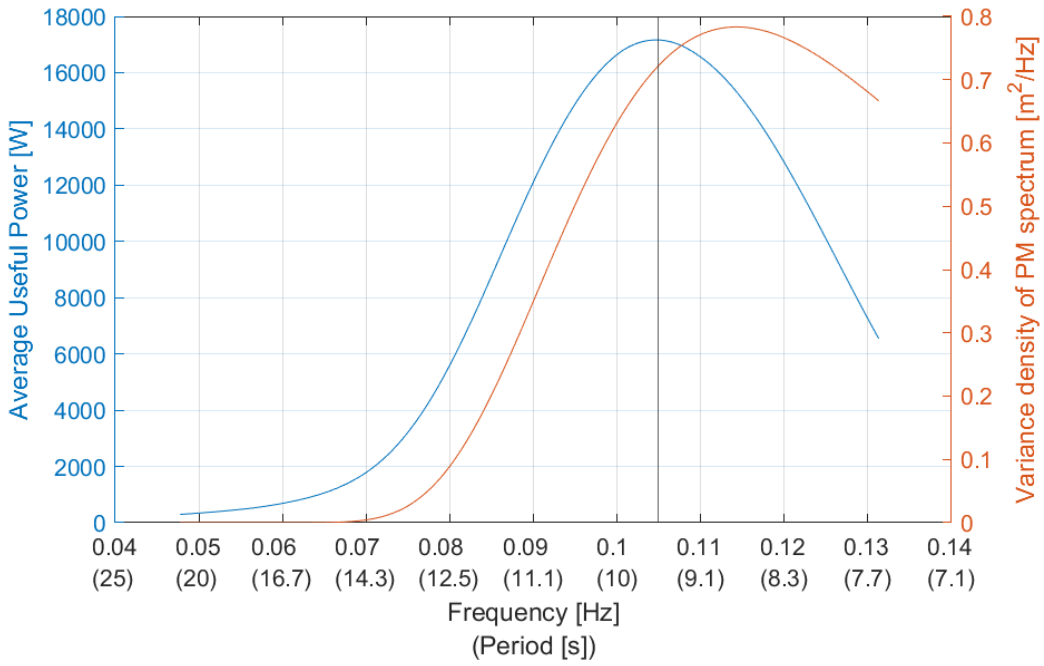

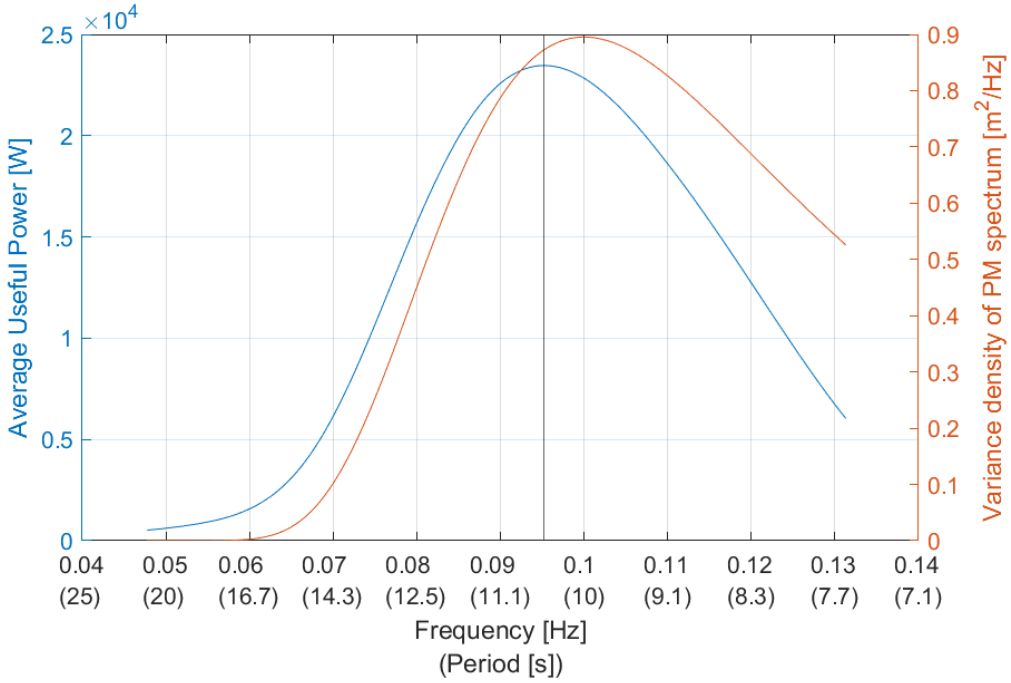

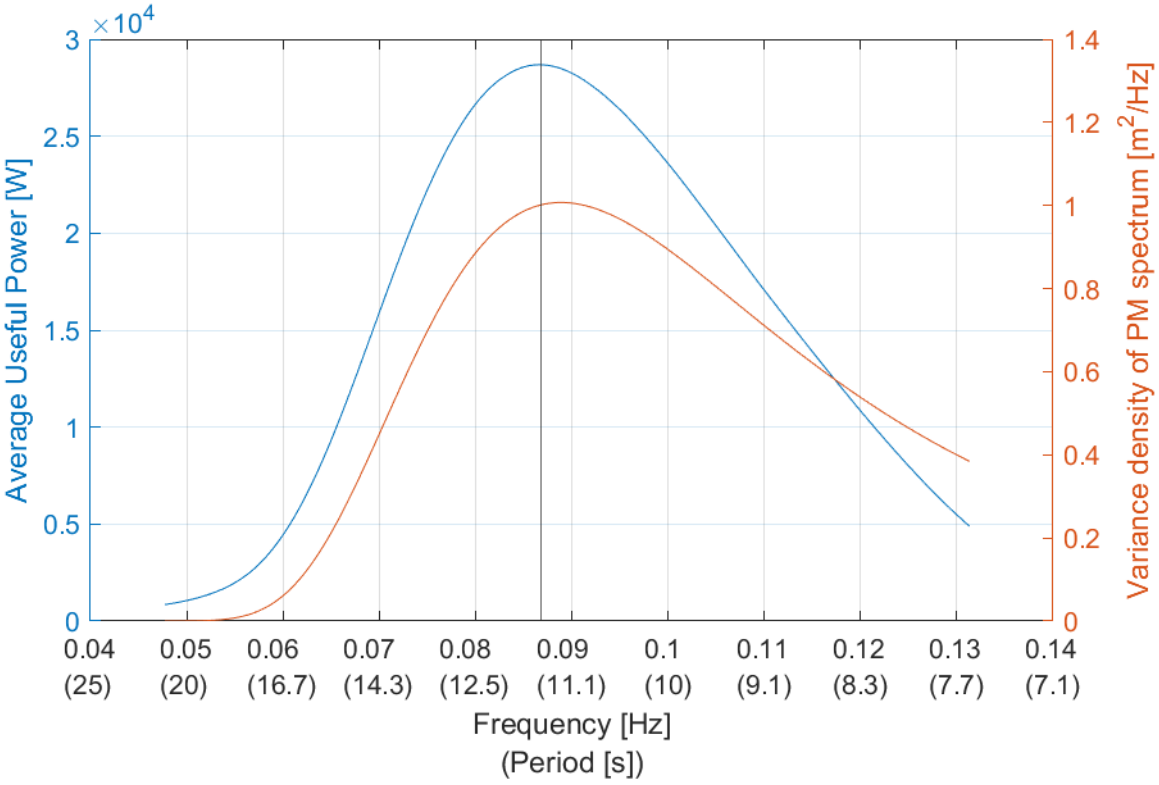
×10^4
3
2.5
2
1.5
1
0.5
0
Average Useful Power [W]
1.4
1.2
1
0.8
0.6
0.4
0.2
0
Variance density of PM spectrum [m^2/Hz]
0.04 (25)
0.05 (20)
0.06 (16.7)
0.07 (14.3)
0.08 (12.5)
0.09 (11.1)
0.1 (10)
0.11 (9.1)
0.12 (8.3)
0.13 (7.7)
0.14 (7.1)
Frequency [Hz]
(Period [s])

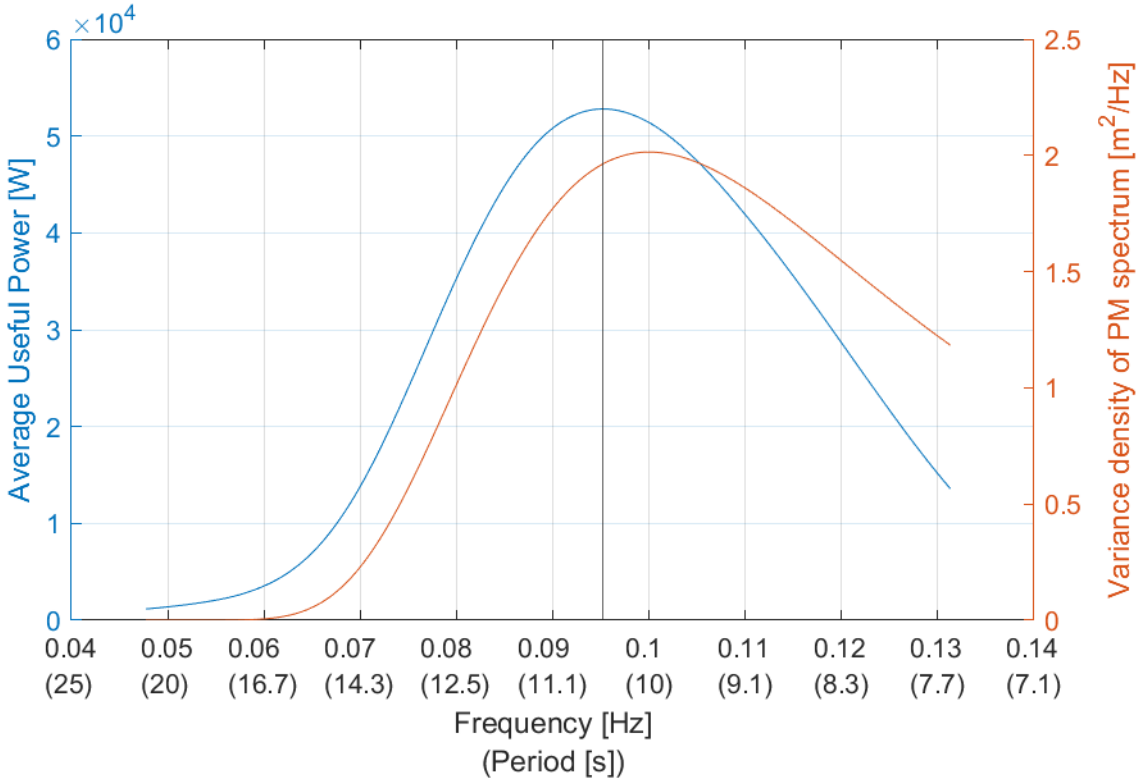
×10^4
6
5
4
3
2
1
0
Average Useful Power [W]
2.5
2
1.5
1
0.5
0
Variance density of PM spectrum [m^2/Hz]
0.04 (25)
0.05 (20)
0.06 (16.7)
0.07 (14.3)
0.08 (12.5)
0.09 (11.1)
0.1 (10)
0.11 (9.1)
0.12 (8.3)
0.13 (7.7)
0.14 (7.1)
Frequency [Hz]
(Period [s])

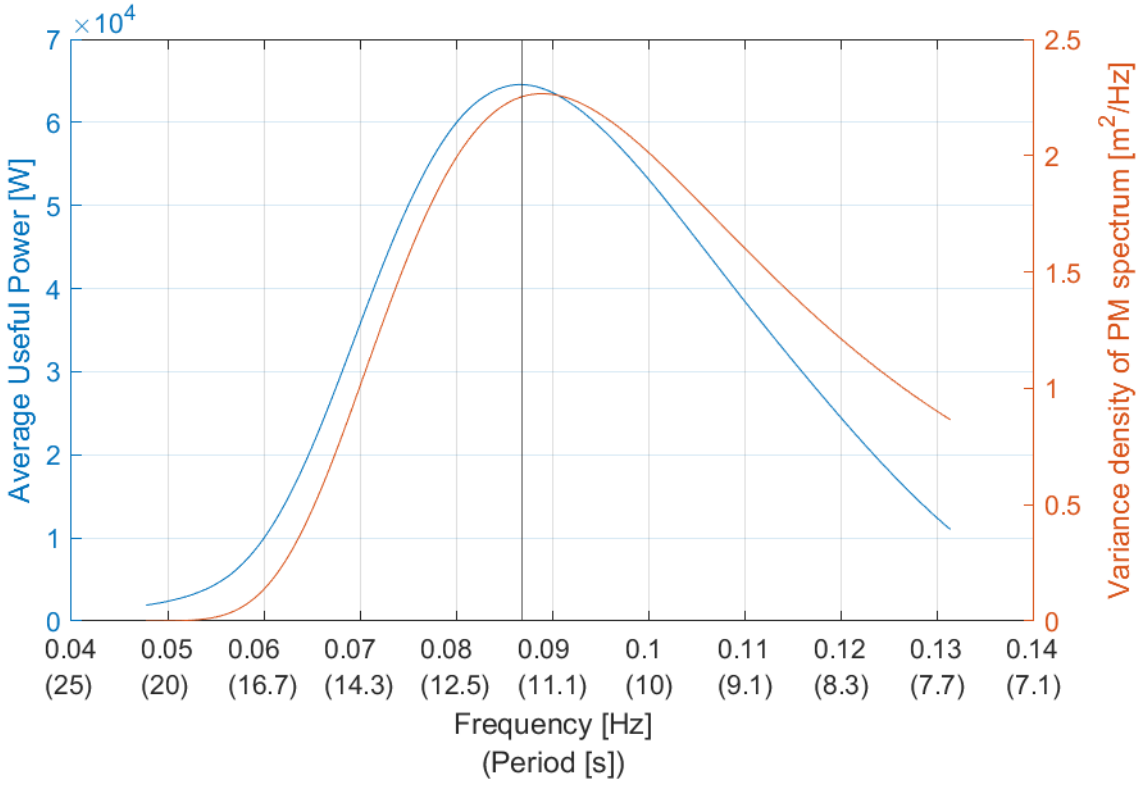
×10^4
Average Useful Power [W]
Variance density of PM spectrum [m^2/Hz]
0.04 (25)
0.05 (20)
0.06 (16.7)
0.07 (14.3)
0.08 (12.5)
0.09 (11.1)
0.1 (10)
0.11 (9.1)
0.12 (8.3)
0.13 (7.7)
0.14 (7.1)
Frequency [Hz]
(Period [s])

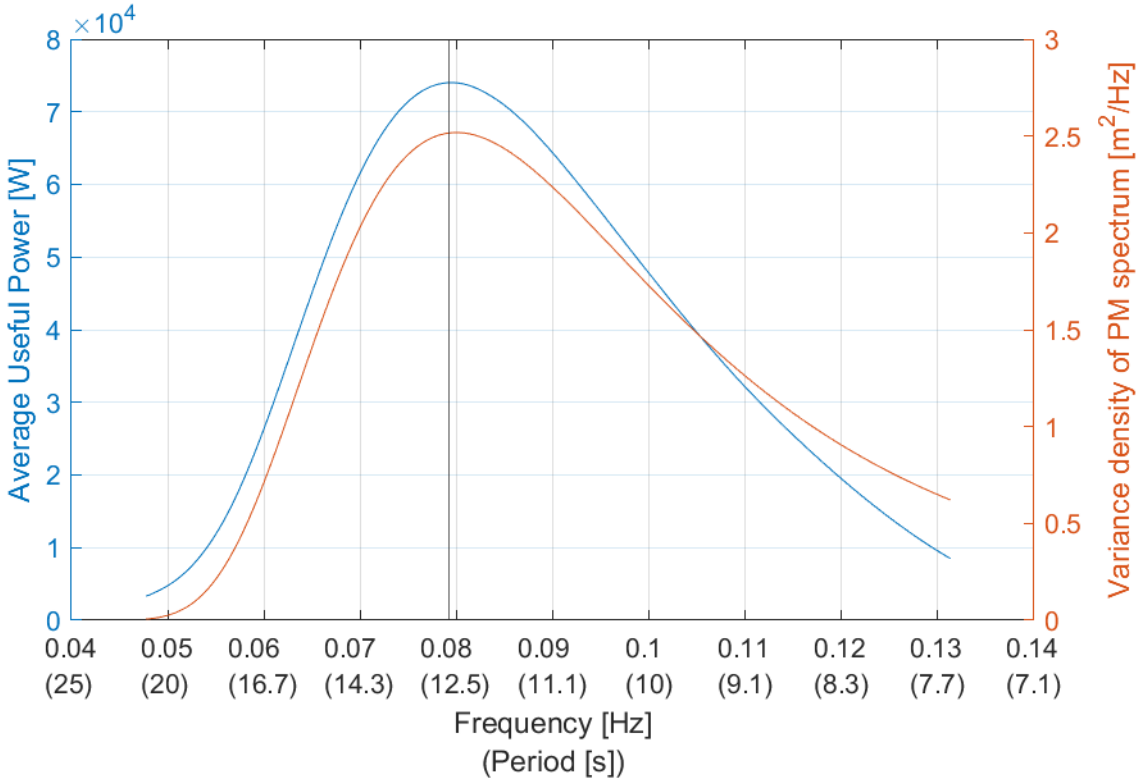
×10^4
Average Useful Power [W]
Variance density of PM spectrum [m^2/Hz]
0.04 (25)
0.05 (20)
0.06 (16.7)
0.07 (14.3)
0.08 (12.5)
0.09 (11.1)
0.1 (10)
0.11 (9.1)
0.12 (8.3)
0.13 (7.7)
0.14 (7.1)
Frequency [Hz]
(Period [s])

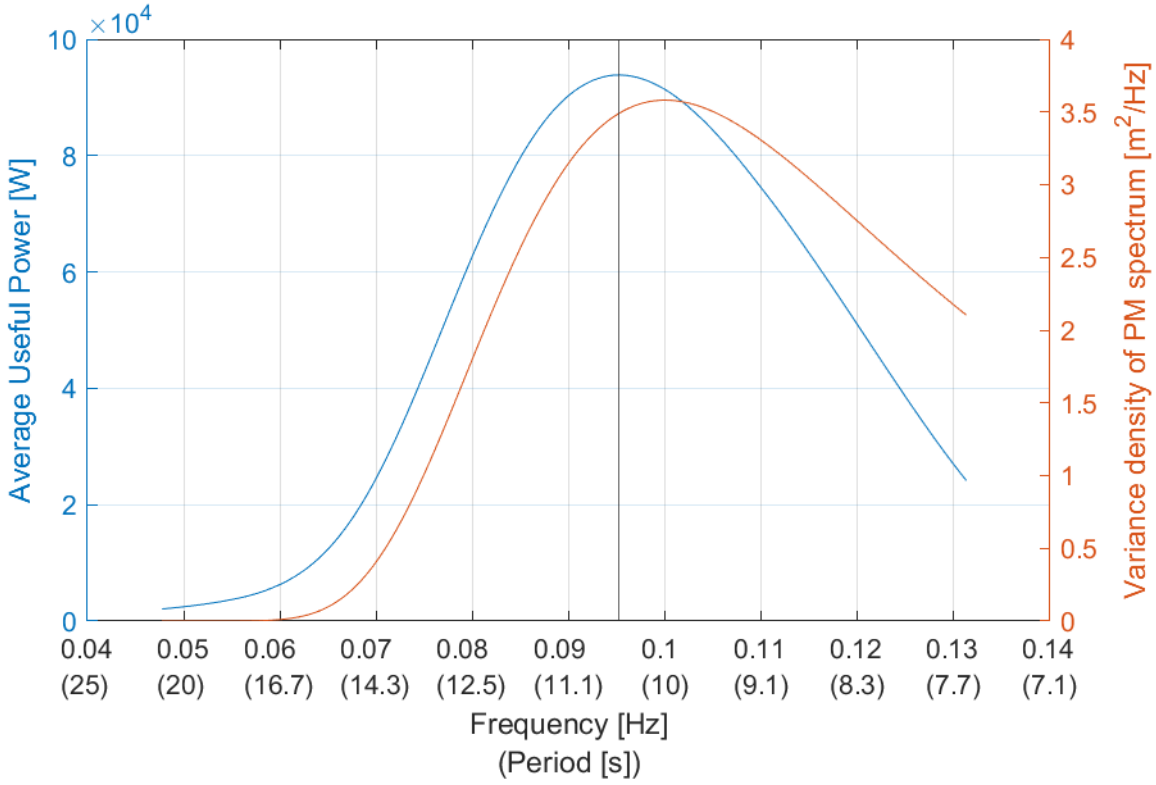
×10^4
Average Useful Power [W]
Variance density of PM spectrum [m^2/Hz]
0.04 (25)
0.05 (20)
0.06 (16.7)
0.07 (14.3)
0.08 (12.5)
0.09 (11.1)
0.1 (10)
0.11 (9.1)
0.12 (8.3)
0.13 (7.7)
0.14 (7.1)
Frequency [Hz]
(Period [s])

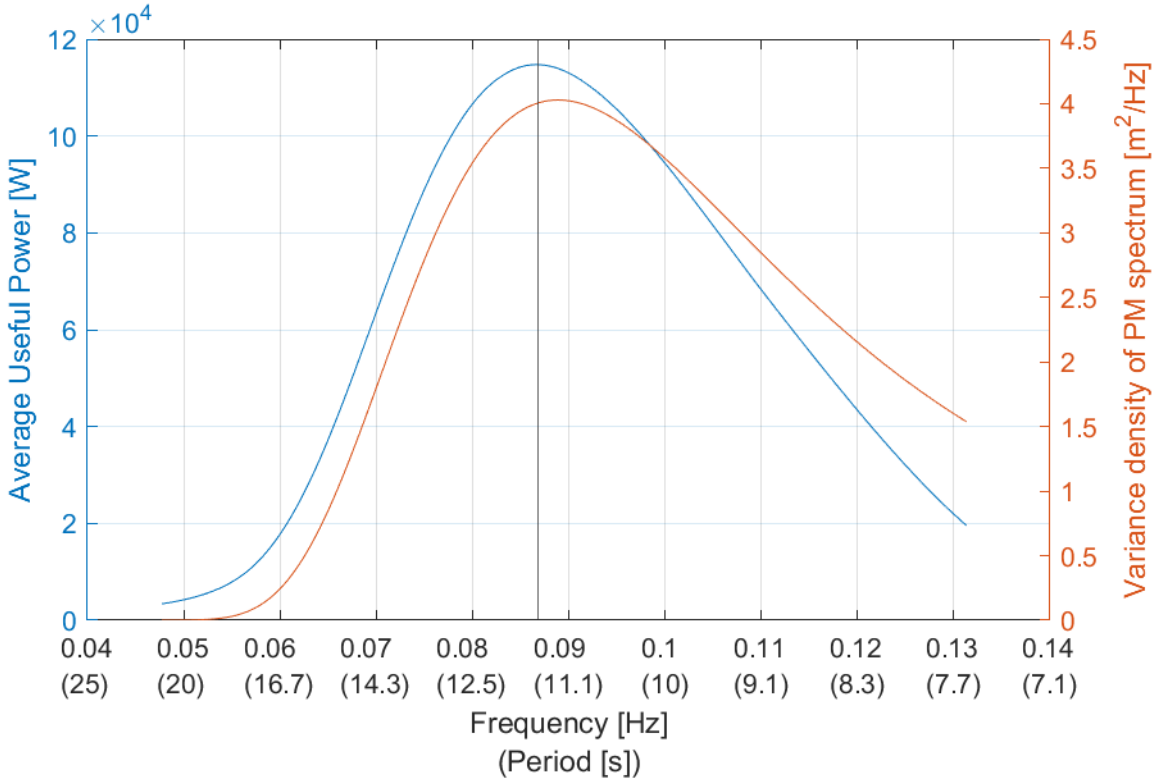
×10^4
Average Useful Power [W]
Variance density of PM spectrum [m^2/Hz]
0.04 (25)
0.05 (20)
0.06 (16.7)
0.07 (14.3)
0.08 (12.5)
0.09 (11.1)
0.1 (10)
0.11 (9.1)
0.12 (8.3)
0.13 (7.7)
0.14 (7.1)
Frequency [Hz]
(Period [s])

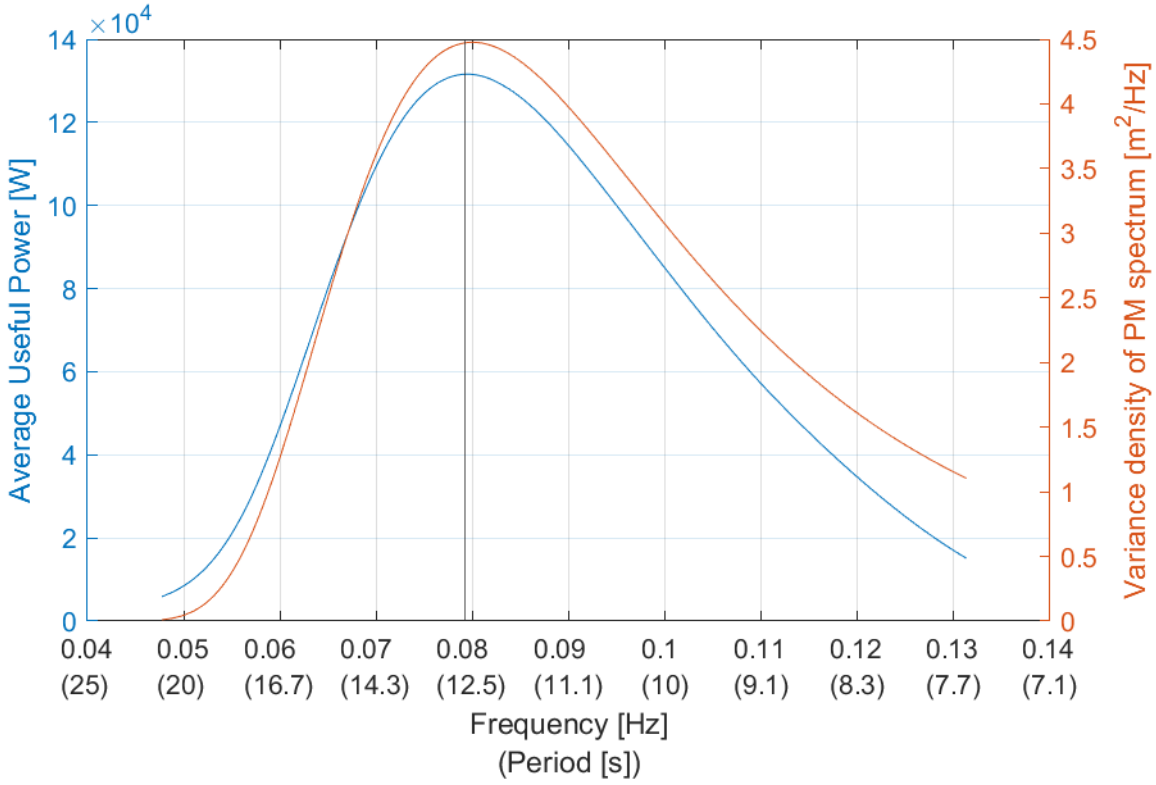
×10^4
14
12
10
8
6
4
2
0
Average Useful Power [W]
4.5
4
3.5
3
2.5
2
1.5
1
0.5
0
Variance density of PM spectrum [m^2/Hz]
0.04 (25)
0.05 (20)
0.06 (16.7)
0.07 (14.3)
0.08 (12.5)
0.09 (11.1)
0.1 (10)
0.11 (9.1)
0.12 (8.3)
0.13 (7.7)
0.14 (7.1)
Frequency [Hz]
(Period [s])

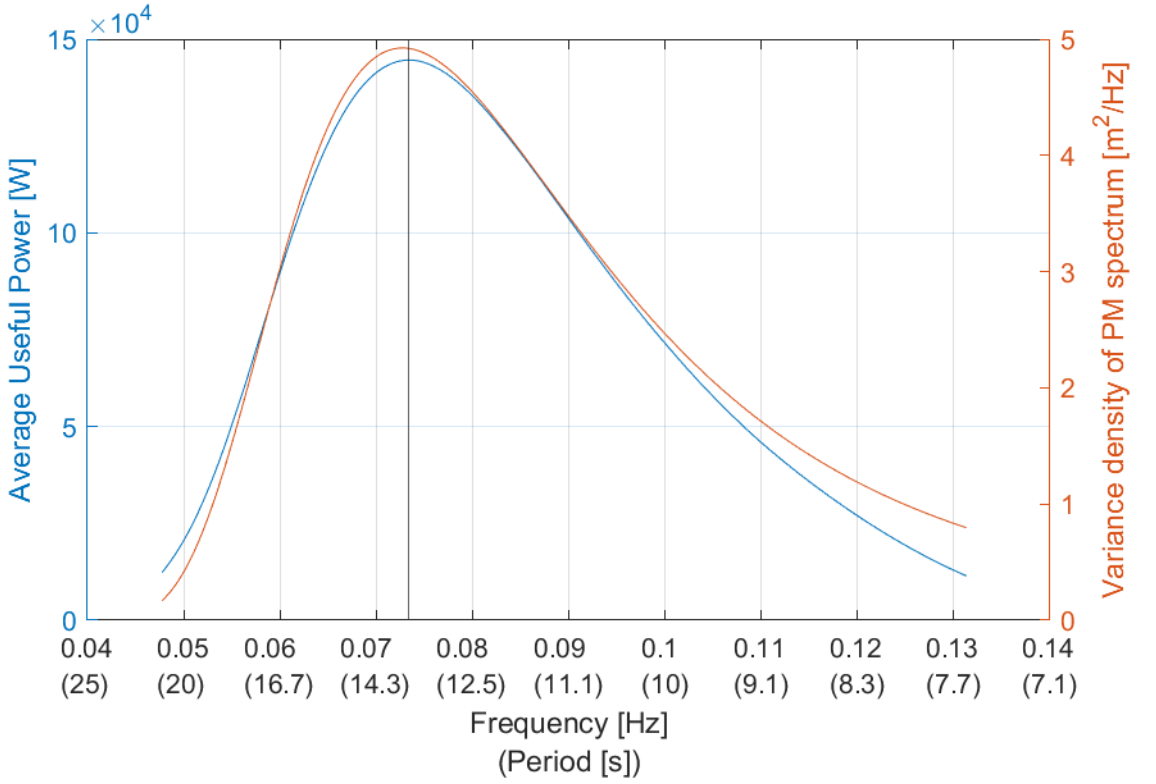
×10^4
15
10
5
0
Average Useful Power [W]
5
4
3
2
1
0
Variance density of PM spectrum [m^2/Hz]
0.04 (25)
0.05 (20)
0.06 (16.7)
0.07 (14.3)
0.08 (12.5)
0.09 (11.1)
0.1 (10)
0.11 (9.1)
0.12 (8.3)
0.13 (7.7)
0.14 (7.1)
Frequency [Hz]
(Period [s])

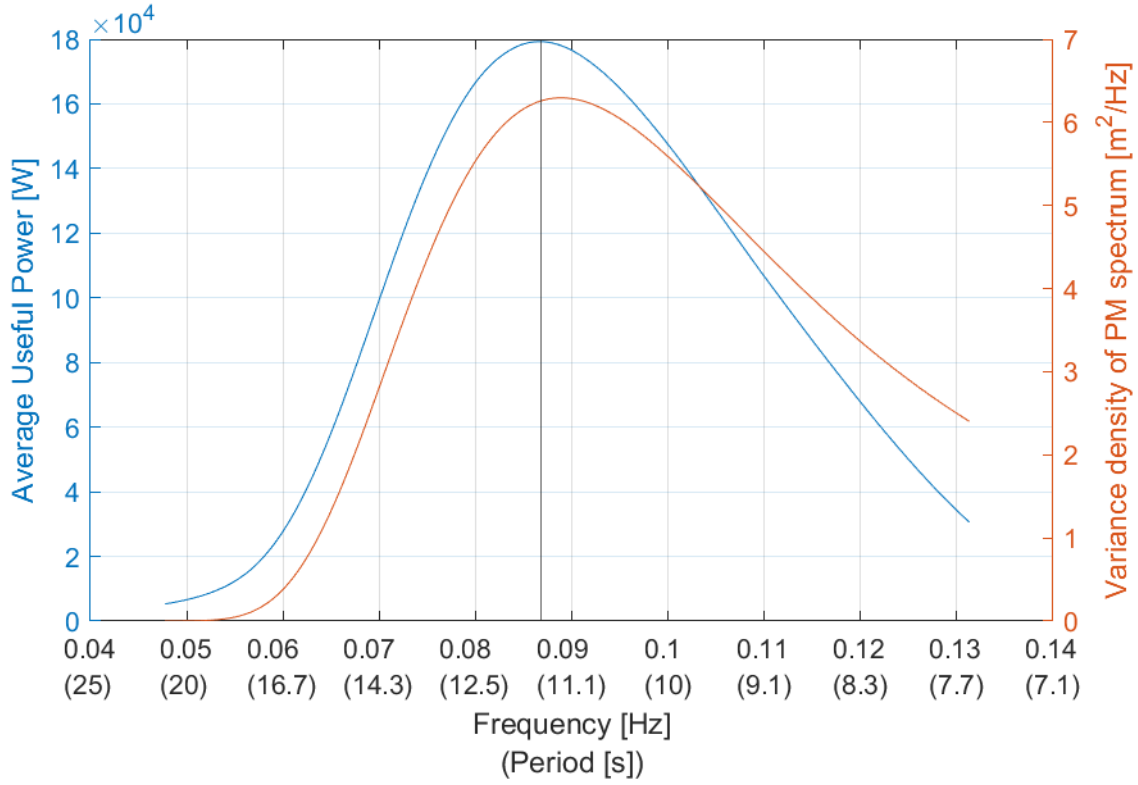
×10^4
Average Useful Power [W]
Variance density of PM spectrum [m^2/Hz]
0.04 (25)
0.05 (20)
0.06 (16.7)
0.07 (14.3)
0.08 (12.5)
0.09 (11.1)
0.1 (10)
0.11 (9.1)
0.12 (8.3)
0.13 (7.7)
0.14 (7.1)
Frequency [Hz]
(Period [s])

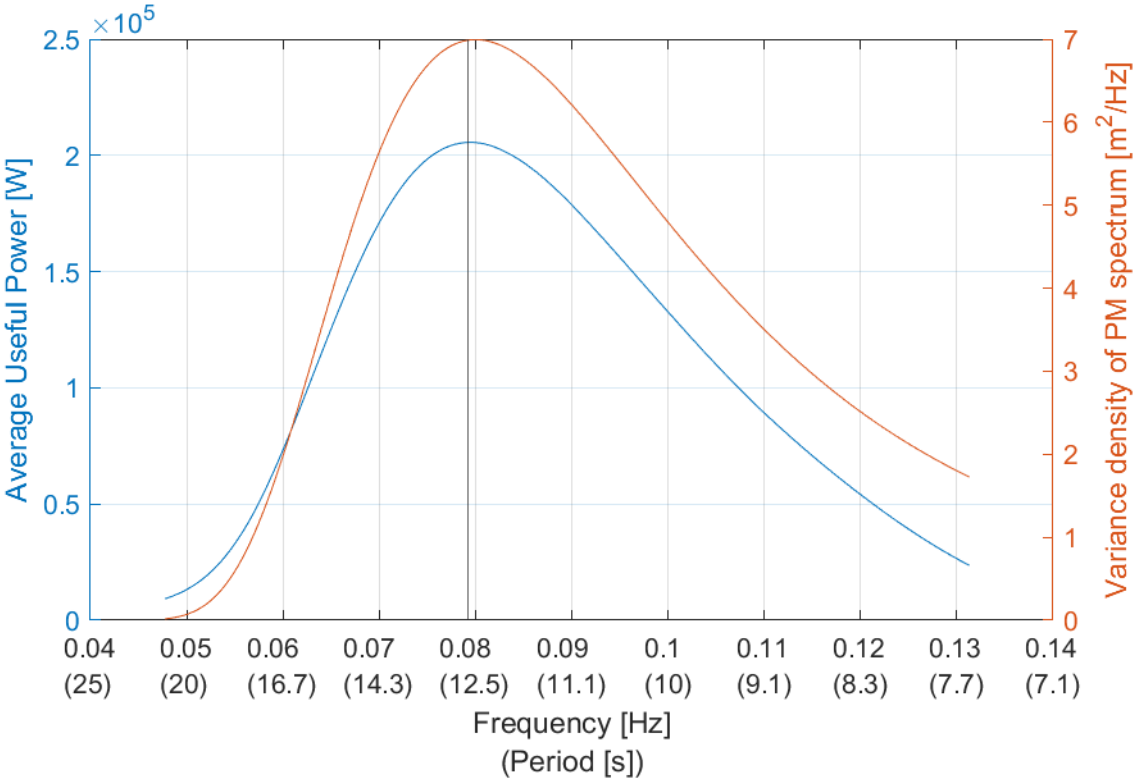
×10^5
Average Useful Power [W]
Variance density of PM spectrum [m^2/Hz]
0.04 (25)
0.05 (20)
0.06 (16.7)
0.07 (14.3)
0.08 (12.5)
0.09 (11.1)
0.1 (10)
0.11 (9.1)
0.12 (8.3)
0.13 (7.7)
0.14 (7.1)
Frequency [Hz]
(Period [s])

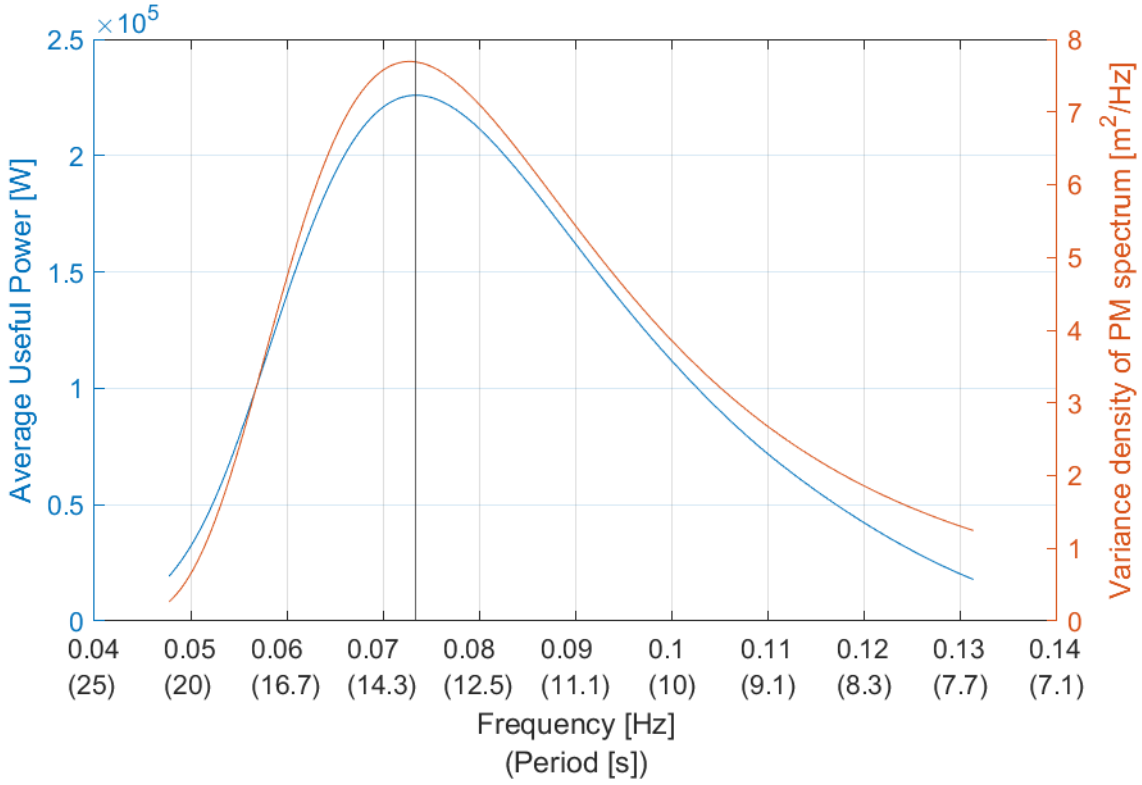
×10^5
2.5
2
1.5
1
0.5
0
Average Useful Power [W]
8
7
6
5
4
3
2
1
0
Variance density of PM spectrum [m^2/Hz]
0.04 (25)
0.05 (20)
0.06 (16.7)
0.07 (14.3)
0.08 (12.5)
0.09 (11.1)
0.1 (10)
0.11 (9.1)
0.12 (8.3)
0.13 (7.7)
0.14 (7.1)
Frequency [Hz]
(Period [s])

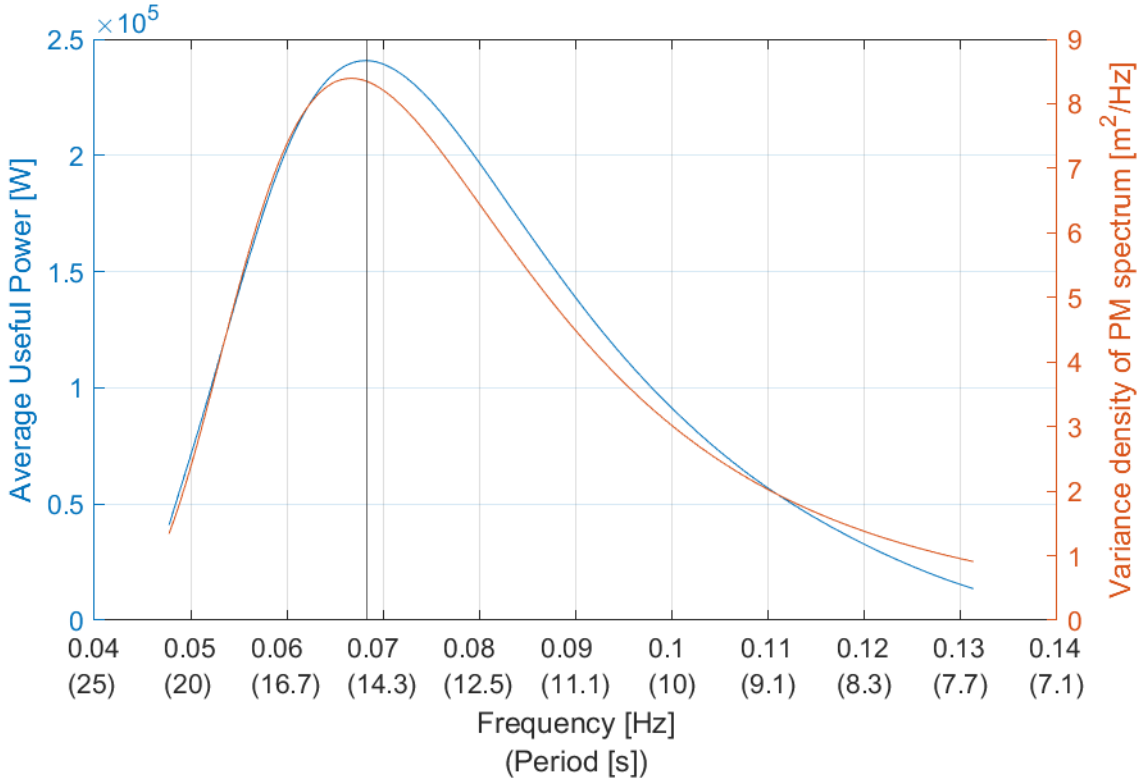
×10^5
2.5
2
1.5
1
0.5
0
Average Useful Power [W]
9
8
7
6
5
4
3
2
1
0
Variance density of PM spectrum [m^2/Hz]
0.04 (25)
0.05 (20)
0.06 (16.7)
0.07 (14.3)
0.08 (12.5)
0.09 (11.1)
0.1 (10)
0.11 (9.1)
0.12 (8.3)
0.13 (7.7)
0.14 (7.1)
Frequency [Hz]
(Period [s])

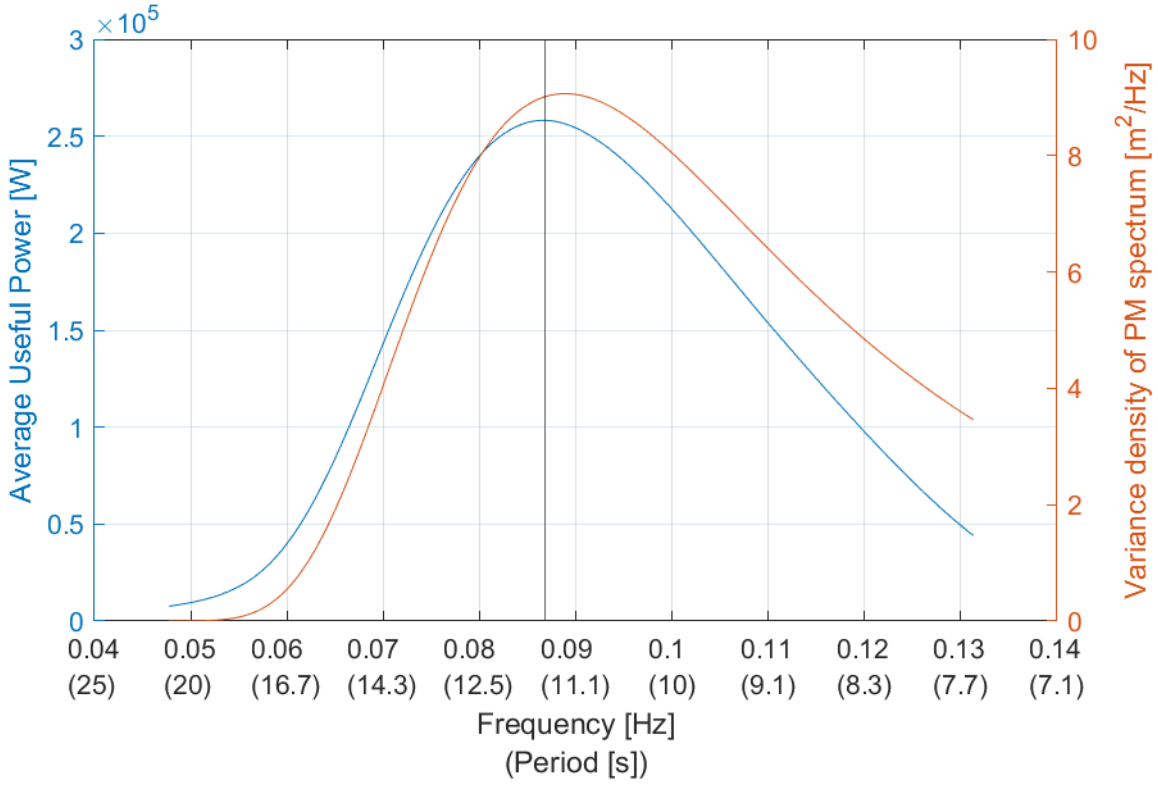
×10^5
3
2.5
2
1.5
1
0.5
0
Average Useful Power [W]
10
8
6
4
2
0
Variance density of PM spectrum [m^2/Hz]
0.04 (25)
0.05 (20)
0.06 (16.7)
0.07 (14.3)
0.08 (12.5)
0.09 (11.1)
0.1 (10)
0.11 (9.1)
0.12 (8.3)
0.13 (7.7)
0.14 (7.1)
Frequency [Hz]
(Period [s])

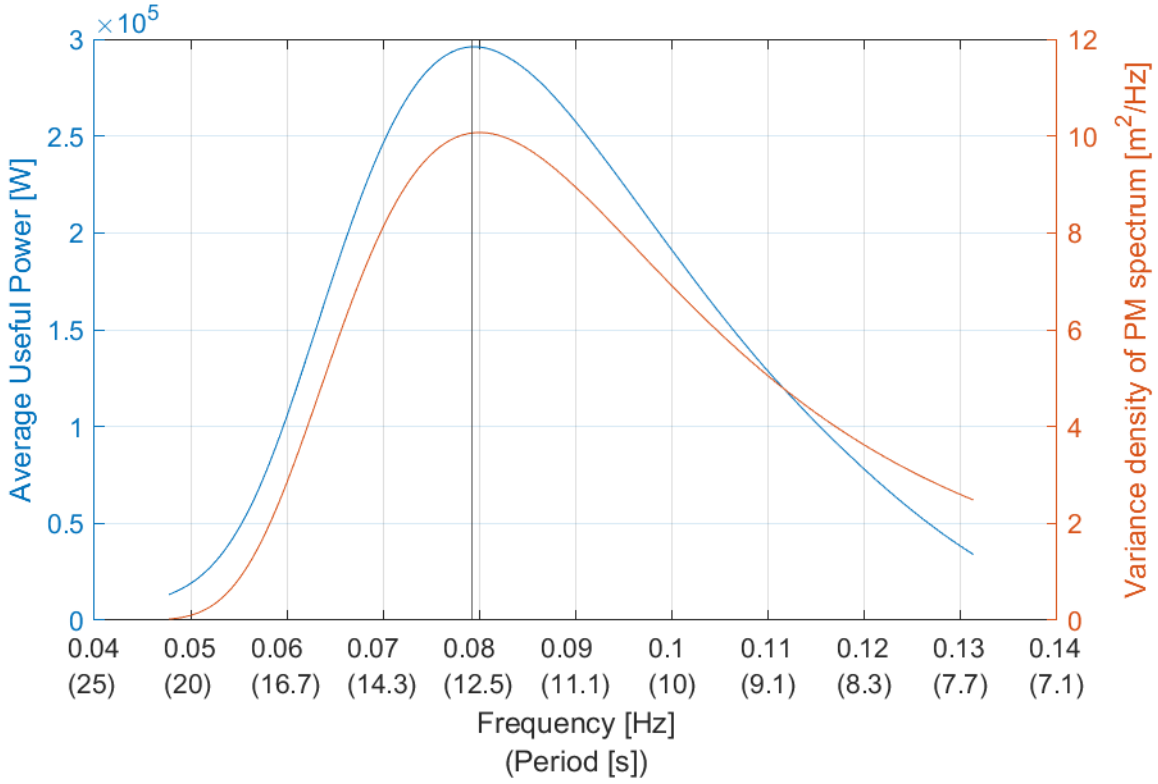
×10^5
3
2.5
2
1.5
1
0.5
0
Average Useful Power [W]
12
10
8
6
4
2
0
Variance density of PM spectrum [m^2/Hz]
0.04 (25)
0.05 (20)
0.06 (16.7)
0.07 (14.3)
0.08 (12.5)
0.09 (11.1)
0.1 (10)
0.11 (9.1)
0.12 (8.3)
0.13 (7.7)
0.14 (7.1)
Frequency [Hz]
(Period [s])

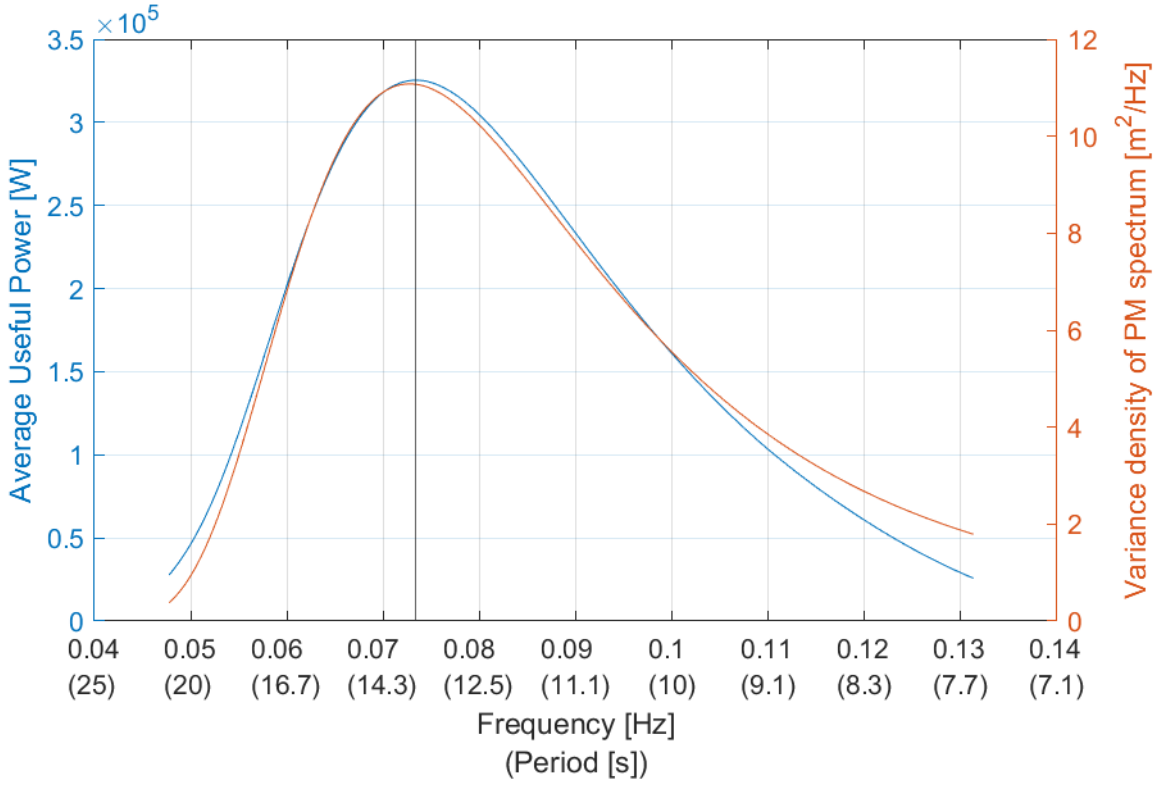
×10^5
3.5
3
2.5
2
1.5
1
0.5
0
Average Useful Power [W]
12
10
8
6
4
2
0
Variance density of PM spectrum [m^2/Hz]
0.04 (25)
0.05 (20)
0.06 (16.7)
0.07 (14.3)
0.08 (12.5)
0.09 (11.1)
0.1 (10)
0.11 (9.1)
0.12 (8.3)
0.13 (7.7)
0.14 (7.1)
Frequency [Hz]
(Period [s])

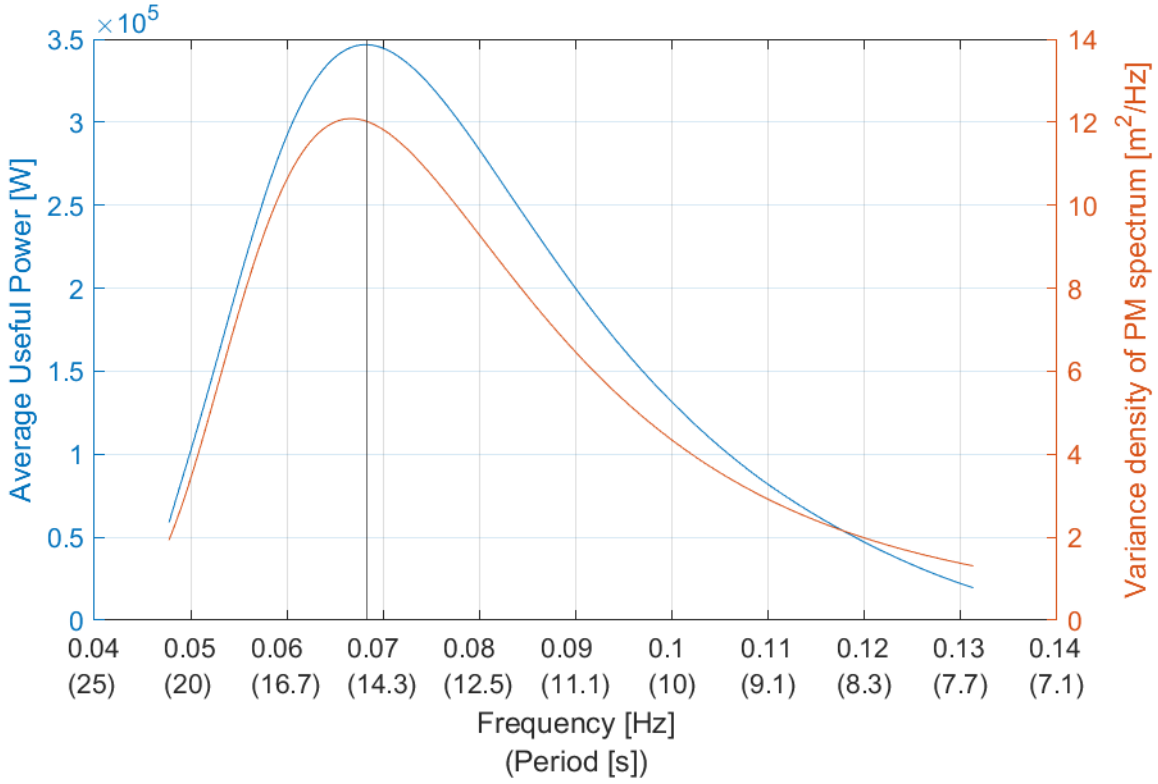
×10^5
3.5
3
2.5
2
1.5
1
0.5
0
Average Useful Power [W]
14
12
10
8
6
4
2
0
Variance density of PM spectrum [m^2/Hz]
0.04 (25)
0.05 (20)
0.06 (16.7)
0.07 (14.3)
0.08 (12.5)
0.09 (11.1)
0.1 (10)
0.11 (9.1)
0.12 (8.3)
0.13 (7.7)
0.14 (7.1)
Frequency [Hz]
(Period [s])

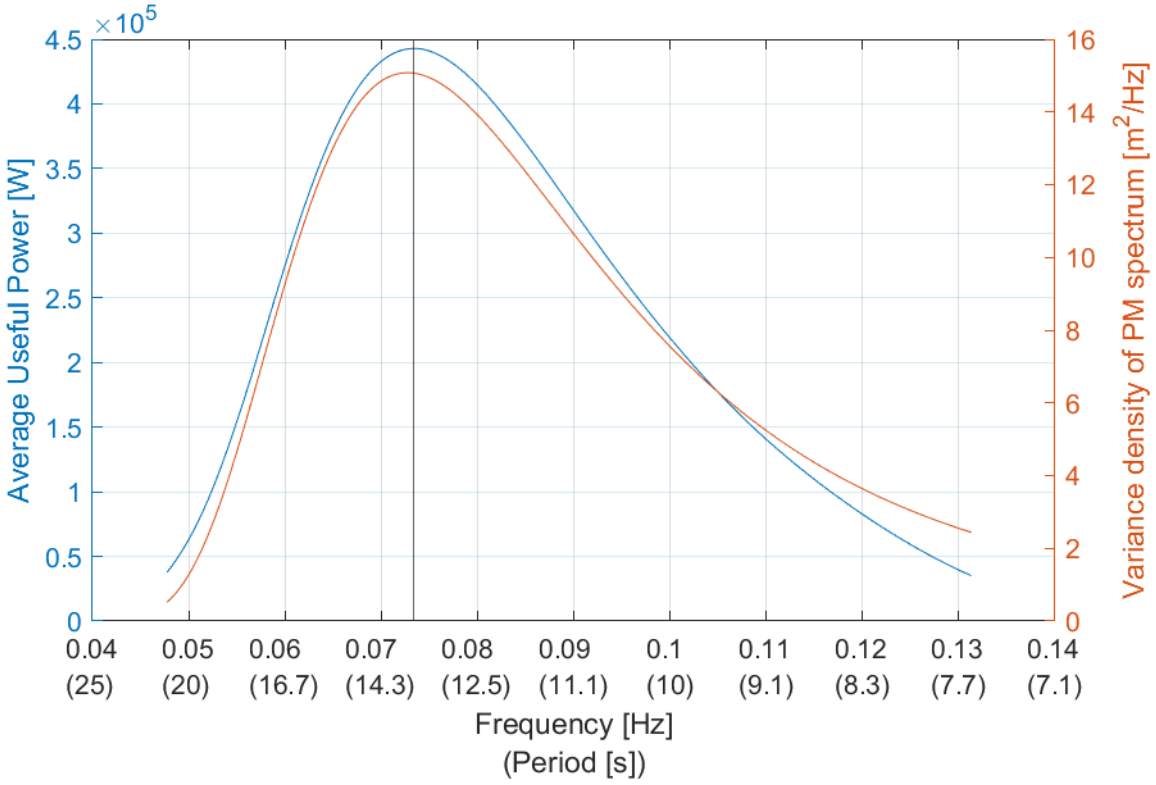
×10^5
4.5
4
3.5
3
2.5
2
1.5
1
0.5
0
Average Useful Power [W]
16
14
12
10
8
6
4
2
0
Variance density of PM spectrum [m^2/Hz]
0.04 (25)
0.05 (20)
0.06 (16.7)
0.07 (14.3)
0.08 (12.5)
0.09 (11.1)
0.1 (10)
0.11 (9.1)
0.12 (8.3)
0.13 (7.7)
0.14 (7.1)
Frequency [Hz]
(Period [s])

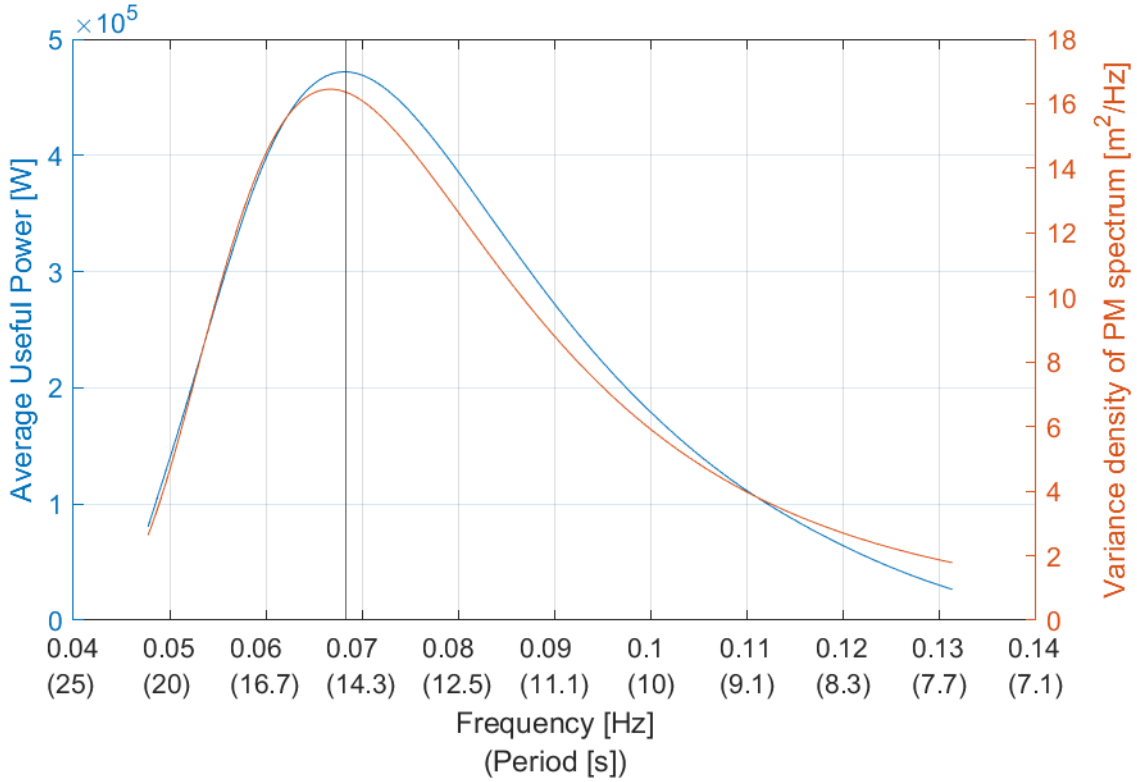
×10^5
5
4
3
2
1
0
Average Useful Power [W]
18
16
14
12
10
8
6
4
2
0
Variance density of PM spectrum [m^2/Hz]
0.04 (25)
0.05 (20)
0.06 (16.7)
0.07 (14.3)
0.08 (12.5)
0.09 (11.1)
0.1 (10)
0.11 (9.1)
0.12 (8.3)
0.13 (7.7)
0.14 (7.1)
Frequency [Hz]
(Period [s])